

On the Behaviour and Radiating Properties of Heavy  
Elements in Fusion Plasmas.

—

Submitted for the degree of Doctor of Philosophy by

Adam Foster

Department of Physics

University of Strathclyde

31st August 2008

# Copyright

This thesis is the result of the author's original research. It has been composed by the author and has not been previously submitted for examination which has lead to the award of a degree.

The copyright of this thesis belongs to the author under the terms of the United Kingdom Copyright Acts as qualified by University of Strathclyde Regulation 3.50. Due acknowledgement must always be made of the use of any material contained in, or derived from, this thesis.

Signed:

Date:

## Abstract

Radiation from impurities in magnetically confined fusion devices is regularly utilised on existing tokamaks for both diagnostic purposes (to reveal plasma conditions) and to estimate the impurity content itself to detect any detrimentally high radiation power losses. For the light elements ( $Z \leq 18$ ) commonly found in tokamaks the atomic physics infrastructure to allow such observations and model the results is well developed.

The proposed design for ITER calls for a partially tungsten divertor. This has led to a resurgence of interest in the behaviour of heavy impurities in plasma. Many codes for generating fundamental atomic data and for modelling plasma behaviour encounter significant difficulties when dealing with heavy elements. This work addresses some of these issues.

This thesis improves baseline methods for calculation of atomic structure and electron impact excitation in order to provide rapid universal coverage of all elements, allowing the selective substitution of higher quality data if and where it exists. This method also allows improved estimates of the total radiated power from heavy species. A technique is then implemented to combine adjacent stages of heavy species into superstages, allowing the use of heavy element atomic data in 2D fluid models of fusion plasmas, specifically the EDGE-2D code suite.

Experiments have been conducted on MAST to observe heavy impurities introduced into the plasma by erosion from a probe tip as a preliminary experiment for a potential erosion diagnostic for ITER.

Neutral beam charge exchange has been studied for heavy species, and an estimate has been made of the likely significance of this process for devices with heavy elements present. Specifically, the cases of MAST-Upgrade and ITER are studied.

# Contents

<b>1</b>	<b>Introduction</b>	<b>1</b>
1.1	Heavy Elements in Fusion: Uses and Challenges . . . . .	1
1.2	Spherical Tokamaks . . . . .	5
1.2.1	History . . . . .	5
1.2.2	MAST . . . . .	6
1.2.3	Future uses of Spherical Tokamaks . . . . .	7
1.3	Outline of this work . . . . .	9
<b>2</b>	<b>Relevant Atomic Physics</b>	<b>11</b>
2.1	Atomic Processes in Plasmas . . . . .	13
2.1.1	Radiative Processes . . . . .	14
2.1.2	Collisional Processes . . . . .	16
2.2	Fundamental data . . . . .	17
2.2.1	Atomic Structure . . . . .	18
2.2.2	Electron Impact Excitation and Ionisation . . . . .	21
2.2.3	Ion Impact Excitation and Charge Transfer . . . . .	27
2.3	Derived Atomic Data . . . . .	29
2.3.1	Timescales in Fusion Plasmas . . . . .	30
2.3.2	Population Modelling and GCR Coefficients . . . . .	31
2.3.3	GCR Coefficient Simplifications . . . . .	34
2.4	ADAS . . . . .	42
<b>3</b>	<b>Improved Heavy Species Baseline Calculations</b>	<b>45</b>

3.1	Motivation . . . . .	45
3.1.1	Electron Impact Excitation Cross-Sections . . . . .	47
3.1.2	Configuration Selection by Promotion Rules . . . . .	48
3.1.3	Optimisation of Promotion Rules . . . . .	52
3.2	Sample Results . . . . .	54
3.2.1	Ionisation Balance . . . . .	57
3.2.2	Line Radiated Power from Individual Stages . . . . .	58
3.3	Superstages . . . . .	62
3.3.1	The Need for Superstaging . . . . .	62
3.3.2	The Superstage Model . . . . .	66
3.3.3	Bundling Schemes - The Natural Partition . . . . .	71
3.3.4	Superstaging in Modelling Codes. . . . .	73
3.3.5	Sample Application - 1D and 2D Plasma Modelling . . . . .	75
3.4	Conclusions . . . . .	78
<b>4</b>	<b>Experiments on MAST</b>	<b>80</b>
4.1	Plasma Surface Interactions Model . . . . .	83
4.2	Experimental Setup . . . . .	85
4.2.1	Introduction of Impurities . . . . .	85
4.2.2	Spectroscopy . . . . .	87
4.3	Midplane Impurity Probe Results . . . . .	90
4.3.1	Core Impurity Observations . . . . .	92
4.3.2	Edge Impurity Observations . . . . .	92
4.4	Influx Estimates . . . . .	100
4.4.1	$\mathcal{SXB}$ Influx . . . . .	100
4.4.2	Sputtering Calculations . . . . .	104
4.5	Transport Analysis . . . . .	106
4.6	Divertor Experiment Results . . . . .	110
4.6.1	Divertor Impurity Probe . . . . .	110
4.6.2	Spectroscopic Setup . . . . .	111
4.6.3	Plasma Conditions . . . . .	114

4.6.4	DIP Results . . . . .	115
4.7	Conclusions . . . . .	119
<b>5</b>	<b>Charge Exchange and Heavy Species</b>	<b>122</b>
5.1	The Charge Exchange Reaction . . . . .	124
5.2	Charge Exchange Cross Sections . . . . .	126
5.2.1	Calculation for Light Elements . . . . .	126
5.2.2	Estimation for Heavy Elements . . . . .	129
5.2.3	The $n$ -shell Resolved Cross Section, $\sigma_n$ . . . . .	131
5.2.4	The $l$ -shell Resolved Cross Section, $\sigma_l$ . . . . .	134
5.3	The Bundle-n Model . . . . .	135
5.4	Emission from Tungsten . . . . .	138
5.4.1	MAST Upgrade . . . . .	138
5.4.2	Emission Estimates . . . . .	139
5.5	Application to ITER and Conclusions . . . . .	141
<b>6</b>	<b>Conclusions</b>	<b>144</b>
6.1	Future Work . . . . .	145
6.1.1	Further Experimental Work . . . . .	145
6.1.2	Heavy Species Baseline Development . . . . .	146
6.1.3	Charge Exchange . . . . .	147
6.2	Contributions of the Author and Publication Plans . . . . .	148

# List of Tables

2.1	The codes available for calculation of electron impact/ionisation cross sections.	24
2.2	The ADAS data formats used in this work . . . . .	43
2.3	The ADAS codes used in this work . . . . .	44
3.1	The iterative changes made to promotion rules . . . . .	54
3.2	The two superstaging schemes used with tungsten in EDGE2D. . . . .	78
4.1	The filters available for studying impurities using cameras. . . . .	90
4.2	The Sn and In lines which were observed in the VUV region. . . . .	94
4.3	The Sn and In lines observed in the visible region . . . . .	98

# List of Figures

1.1	The proposed shape and material composition of the wall of the ITER vessel.	3
1.2	The aspect ratio of spherical tokamaks . . . . .	6
1.3	A cutaway view of the MAST vessel and coils. . . . .	7
1.4	The shape of a typical MAST plasma . . . . .	8
2.1	The effective collision strengths and $\mathcal{FPEC}$ for $\text{Xe}^{26+} 3d^{10} 1S_0 \rightarrow 4d^1 S_0$ . . . . .	28
2.2	The $S_{CD}$ ionisation coefficients for the $n = 3$ shell of Sn. . . . .	38
2.3	A comparison of the DR and RR contributions to $\alpha_{CD}$ for Sn . . . . .	40
2.4	The $\mathcal{PRB}$ and $\mathcal{PCT}$ for $\text{Sn}^{+19}$ . . . . .	40
3.1	A schematic of the adas8xx code suite. . . . .	49
3.2	The total radiated power from tungsten as a function of $T_e$ . . . . .	53
3.3	The step by step nature of an adas8xx_opt_promotions_control run, for $\text{W}^{+20}$	55
3.4	The structure of the promotion rule optimisation code. . . . .	56
3.5	The number of configuration and levels present in runs of ADAS808. . . . .	57
3.6	The ratio (case A/case B) of the recombination and ionisation rate coefficients	59
3.7	Total radiated line power calculations for different coupling schemes from ADAS808. . . . .	61
3.8	$\mathcal{PCT}$ calculations for different coupling schemes for tungsten . . . . .	63
3.9	Difference in $\mathcal{PCT}$ in the $ca$ coupling scheme for different calculation sizes .	64
3.10	$\mathcal{FPEC}$ s for $\text{W}^{+17}$ in different coupling schemes . . . . .	64
3.11	$\mathcal{PEC}$ s for $4p^5 4d^{X+1} \rightarrow 4p^6 4d^X$ and $4p^6 4d^{X-1} \rightarrow 4p^6 4d^X$ transitions. . . . .	65
3.12	The superstaging method, applied to carbon . . . . .	67
3.13	The fractional change in ionisation potential for tungsten. . . . .	72

3.14	The fractional abundance of the components of a tungsten superstage. . . .	74
3.15	The plasmas which were used for comparison of different superstaging systems.	76
3.16	A comparison of different bundling schemes for nickel and tungsten. . . . .	77
3.17	The ITER plasma conditions used with superstaged tungsten . . . . .	77
3.18	The density along the separatrix for different partitioning of tungsten . . . .	79
4.1	The potential drop at a floating surface in a plasma. . . . .	83
4.2	The increase in energy of a $C^{+1}$ ion approaching a surface . . . . .	84
4.3	The old materials probe head used in the M3b campaign in 2004. . . . .	86
4.4	The new materials probe designed for use in midplane impurity experiments	86
4.5	The positions of the spectrometers and cameras used in midplane experiments	87
4.6	Typical plasma parameters used with the midplane probe on MAST. . . . .	91
4.7	The VUV spectra recorded on SPRED for shot 13837 . . . . .	93
4.8	The predicted and observed spectra for Sn in MAST shot 14479 . . . . .	95
4.9	The predicted and observed spectra for In in MAST shot 15100 . . . . .	96
4.10	The time history of a Sn XXI and In XXII line in the core of the plasma. . .	97
4.11	The DIVCAM image recorded at 0.259s for MAST shot 13835. . . . .	98
4.12	The spectra recorded before and during the plasma-probe interaction. . . .	99
4.13	The intensity of the different lines observed on SPEX as a function of $\delta r_{sep}$	101
4.14	The $\mathcal{SXB}$ ratios for the observed Sn and In near-neutral stages . . . . .	102
4.15	A comparison of the old and new TS systems . . . . .	103
4.16	Influx estimates obtained from photon counts and $\mathcal{SXB}$ calculations. . . . .	104
4.17	Physical sputtering yield estimates for Sn and In obtained from SRIM . . . .	105
4.18	Estimates of the influx from the probe tip obtained from SRIM data . . . . .	106
4.19	Estimates of the anomalous transport coefficients for two MAST shots. . . .	108
4.20	Ionisation balance for Sn as a function of temperature . . . . .	109
4.21	The divertor impurity probe. . . . .	111
4.22	The divertor impurity probe protruding from the Mast Imbricated Divertor.	112
4.23	The lines of sight of the spectrometers used in the DIP experiments . . . .	112
4.24	The view from the Photron camera, taking during a disruption . . . . .	113
4.25	Images from the photron camera and spectra from the O.O. spectrometer . .	116

4.26	Conditions at the sample and influx rates for Sn . . . . .	118
4.27	The Al spectrum lines recorded before and during the disruption . . . . .	119
4.28	Conditions at the sample and influx rates for Al . . . . .	120
5.1	The wavelength of light emitted in $n$ to $n'$ transitions in $C^{+5}$ . . . . .	125
5.2	$n$ -shell selective charge exchange cross sections for the H( $n=1$ ) donor. . . . .	127
5.3	$l$ -shell selective charge exchange cross sections for the H( $n=1$ ) donor. . . . .	128
5.4	Scaled total CX cross sections . . . . .	130
5.5	Scaled $n$ -shell selective cross sections . . . . .	132
5.6	Scaled $n$ -shell selective cross sections for low neutral beam energy . . . . .	133
5.7	Scaled $l$ -shell selective cross sections . . . . .	136
5.8	Structure of codes for obtaining CX emission estimates . . . . .	137
5.9	The line of sight used for the MAST Upgrade predictions . . . . .	139
5.10	The predicted emission from one ionisation stage of tungsten at $T_e \approx 2.4\text{keV}$	140
5.11	The predicted emission from a steady state ionisation balance of tungsten .	141
5.12	Predicted line integrated tungsten CX and Bremsstrahlung for MAST-U. .	142
5.13	Predicted line integrated tungsten CX and Bremsstrahlung for ITER . . . .	142

# Acknowledgements

Firstly, I would like to thank both EPSRC and UKAEA Culham for funding this work, and UKAEA Culham for access to the facilities at Culham on which this research was conducted. I would like to thank my supervisors Hugh Summers and Glenn Counsell for the insight and help they have given me over the past years. Hugh, for his vast knowledge of atomic physics and his patience and readiness to discuss concepts which I should probably already have understood; and Glenn, for his knowledge of plasma and SOL physics and for always helping with the experiments and analysis.

I would also like to thank Allan Whiteford, Martin O'Mullane and Hugh Summers for taking the time to read over my thesis, especially given the roughness of some of the early drafts, and for many enjoyable conversations about both physics and non-physics matters.

I would like to thank everyone at MAST for their assistance with my various experiments. There are too many to name, but special thanks goes to Graeme Wearing, whose work in designing the DIP was invaluable: otherwise it would still be a pretty sketch on a whiteboard. Also I would also like to thank Steve Lisgo for many enlightening conversations about the scrape off layer and the joys of Fortran 90, and to John Dowling for assisting in the setup of the spectrometers and cameras during operations, often at very short notice.

For keeping me sane during my time in Oxford, I would like to thank my housemates, Martin James, Seb Tallents and Jamie Zacks. Also, for the brief time they were here, Diana Trimiño, Jean-Francois Gagnon and Veronique Nollet for the same. I would also like to thank Alex Carter, Tom O'Gorman, James Harrison and Rory Scannell for putting up with my frequent visits to the Student Ghetto when they were trying to get some work done, and to them and the many other students at Culham past and present for the many

interesting social experiences.

I would also like to thank my parents for offering their unwavering support as the many deadlines came (and sometimes went) for completion of this thesis, and my brother for his equally unwavering prodding to finally finish being a student, have a shave, and get a real job.

Finally, I would like to thank my girlfriend Julia Breslin, who has given me an excuse to visit places ranging from the Arctic circle to Florida swamps; who reminds me every day that there is a world outside of the computer screen, and it is definitely worth seeing.

---

Adam Foster

August 2008

# Chapter 1

## Introduction

### 1.1 Heavy Elements in Fusion: Uses and Challenges

Research into magnetically confined fusion, which aims ultimately to produce a functioning fusion reactor for power generation, recently received a great boost with the announcement in 2006 that the International Thermonuclear Experimental Reactor (ITER) will be constructed at Caderache, France. This announcement has greatly accelerated interest in several areas of physics and engineering relevant to the design and operation of ITER.

One area where ITER will differ from most present tokamaks is in the choice of wall material. In ITER, the walls of the vessel will be made mostly from beryllium, as it is a light element and therefore contributes little to the power radiated from the plasma (see section 2.3.3). However, this material is unsuitable for use in the divertor region, where most of the plasma-wall interaction takes place, as it is susceptible to melting[1].

Many tokamaks use carbon divertor tiles, either in the form of graphite or carbon fibre composites (CFCs). These tiles can withstand a much larger power loading than most other materials available, which has made them the obvious choice until now. Unfortunately, while they are highly resistant to damage from physical sputtering, they are susceptible to chemical sputtering by hydrogen isotopes in the plasma, through the formation of hydrocarbons (e.g. methane,  $\text{CH}_4$ ). In current tokamaks this is not a significant concern, as hydrogen or deuterium are used as fuel ions. However in a future power plant, deuterium-tritium fusion will be used to create power, as this reaction has a larger

cross section than deuterium-deuterium fusion. Therefore for demonstration purposes in ITER, tritium will be used routinely, and in significantly higher quantities than in those experiments where tritium has already been utilised. Tritium is a radioactive isotope of hydrogen, and therefore hydrocarbon formation and redeposition will lead to tritium being retained in the vessel walls during each ITER pulse, which will rapidly lead to the vessel becoming excessively radioactive and being shut down - the limit for tritium content in ITER is 1kg, which could be reached in 200 pulses if the divertor is made of carbon[2], against an expected experimental life of 20 years at 1000 pulses/year.

It has therefore been decided to construct much of the divertor from tungsten. This material can withstand a power loading of over  $20\text{MW}/\text{m}^2$ [3, 4] and is not susceptible to chemical erosion by hydrogen isotopes. This approaches the performance of CFC tiles, however concerns exist about melt layers forming and then rapidly eroding leading to rapid degradation of a tungsten tile in some areas. It is therefore proposed to use a small area of CFCs in the divertor where the main plasma-wall interaction takes place (see figure 1.1).

Experience in the 1970s on the Princeton Large Torus (PLT), which had a tungsten limiter, and other devices with high-z components was of unacceptably high core impurity radiation losses. For example, in PLT,  $\approx 85\%$  of the total plasma energy was lost through impurity radiation[5]. For two decades since then fusion devices deliberately tried to avoid using heavy elements for plasma facing components, or where this is unavoidable, they have coated them with lighter elements (e.g. carbon) to prevent them from polluting the plasma.

Knowing that the ITER design called for a non-carbon solution, several experiments have moved to again investigate metal walls. The Alcator C-Mod[6] tokamak has a full molybdenum wall, while the ASDEX-Upgrade device[7] has since 1996 been slowly converting from an all-carbon PFC device to an entirely tungsten or tungsten-coated one[8]. Significant effort has been put into observing the impurity concentration in the plasma and monitoring the effect it has on the plasma [9]. It has been found that by keeping a cold dense outer plasma, the erosion rate and therefore the build up of tungsten in the core can be limited [10]. The problems experienced in earlier metal tokamaks have been overcome by a combination of wall conditioning techniques such as boronisation, and the use of significantly more additional heating power than was available on earlier devices[11].

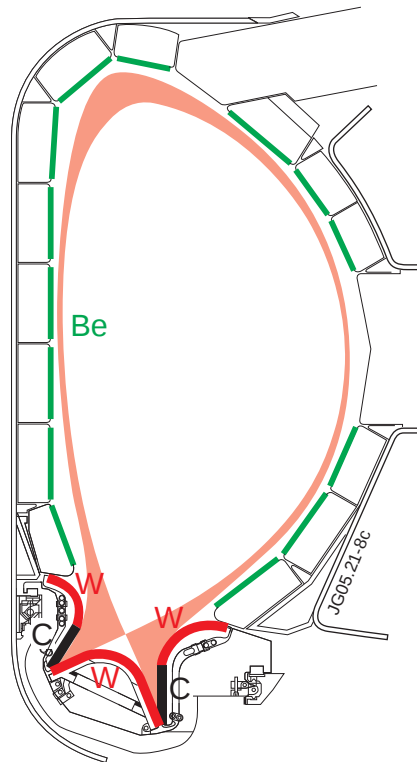


Figure 1.1: The proposed shape and material composition of the wall of the ITER vessel.

Prior to and during the construction of ITER, it is planned to implement an ITER-like wall in the Joint European Torus (JET), which will replicate the shape of the ITER divertor and the materials used, with Be walls and an all-tungsten divertor (such a divertor is another possible plan for ITER, should tritium retention in carbon prove to be an insurmountable issue)[12]. As well as being the largest, and therefore most ITER-like of the present tokamaks, JET is also one of the few sites capable of handling both tritium and beryllium, the former material being radioactive and the latter highly toxic. This opens up several unique opportunities for this experiment: both the power handling capabilities and tritium retention of tungsten and beryllium can be observed. Of particular interest is the behaviour of the metals during strong edge localised modes (ELMs, [13]), which deposit a large quantity of power onto the walls in a short space of time, and are expected to lead to melting of surface layers of the metals, possibly leading to increased erosion or deformation.

It is clear, therefore, that heavy elements, although previously relatively rare in tokamaks, are becoming more widespread and in the future will become ubiquitous in large devices. The routine use of impurities in plasmas for a variety of diagnostic purposes has driven the investigation of the atomic processes responsible for radiation from a plasma for these light elements (broadly defined as  $z_0 \leq 18$ ) to allow modelling and analysis of experiments. Heavy elements have received significantly less study, due to a combination of lack of interest (they are also largely irrelevant to astrophysical plasmas, which is the other main driver of relevant atomic physics research), and the complexity of their atomic structure, which make the application of sophisticated models difficult or (currently) impossible.

Yet such elements are now used in tokamaks, and experiments are analysed using the atomic data which is available. For example, on ASDEX-U significant use has been made of the the cooling curves (which are a total of the radiated power), to estimate the effect of different concentrations of a variety of different elements on the plasma, with a focus on tungsten[9].

This has driven significant effort into understanding the atomic physics of such elements and their behaviour in plasmas. However these efforts have focused entirely on one or two heavy elements: tungsten, due to its use for wall materials, and krypton and xenon, which

as gaseous elements are easily introduced into the plasma via gas lines, and are used for cooling the plasma edge. Any species other than tungsten which could have either a structural or physics relevance has been largely ignored.

Ideally, this gap would be filled with comprehensive studies of the highest quality relevant atomic data. However such a project is not feasible on the timescales on which answers are required. Nor is it necessary, as many stages of elements will not exist in significant quantities in plasma, and therefore high resolution data is not required. Those stages which have the (relatively) easier to calculate atomic structure are also those most likely to contribute to observable line emission. Yet analysis of experiments requires some classes of data from all the stages of a given element. Therefore the ability to rapidly generate atomic data of moderate quality, but with comprehensive coverage of all elements, is useful, and forms the focus of much of this work.

## 1.2 Spherical Tokamaks

The experiments which will be described here (largely in chapter 4) were conducted on the Mega Ampère Spherical Torus (MAST[14]) at UKAEA Culham Laboratory, between 2004 and 2008. A basic outline of fusion is given [15] and the introductory chapters of [16], and will not be repeated here, however the spherical tokamak concept will be described briefly as it is less well known.

### 1.2.1 History

A spherical tokamak (ST) differs from a conventional tokamak due to its much smaller aspect ratio,  $A = R/a$ , where  $R$  is the major radius, and  $a$  is the minor radius of the plasma (see figure 1.2). The design was first mooted in 1986[17]. Notable theoretical aspects of the design were the high value of  $\beta$ , which is a measure of the efficiency of the confinement of the plasma pressure by the magnetic field  $\beta = p/(B^2/2\mu_0)$ . Here  $p$  is the plasma pressure,  $B$  is the magnetic field at the geometric axis of the plasma, and  $\mu_0$  is the permeability of free space. The denominator is also known as the magnetic pressure. This gain implies that similar plasma confinement to conventional devices can be achieved using a weaker magnetic field.

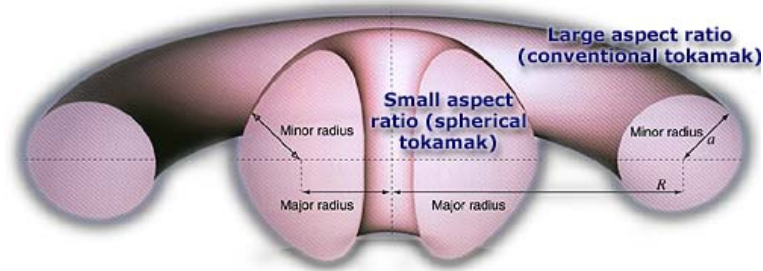


Figure 1.2: The (exaggerated) difference in shape between a conventional and a spherical tokamak. Spherical tokamaks are those with  $R/a < 2$ . The aspect ratio for MAST is 1.4, while that of JET is 2.4.

The implications of this benefit are a much cheaper tokamak, which is important if fusion is to become a commercial reality. The reduced aspect ratio allows for significantly reduced magnet size, as a power plant would be physically smaller. Additionally, the reduced field requirements would allow non-superconducting coils to be used. Given that the superconducting coils required for ITER are estimated to cost  $\approx \text{€}1$  billion (at 2000 prices), or 30% of construction cost[18], the savings would be considerable.

Early experiments using modified spheromak experiments[19, 20] showed some promise, however these were very cold plasmas ( $\approx 25\text{eV}$ ). The Small Tight Aspect Ratio Tokamak (START, [21]) was constructed in 1992 at UKAEA Culham to investigate hotter plasmas more typical to fusion research. The device achieved world record values of  $\beta$  with an aspect ratio of 1.4[22]. This achievement spurred further interest and construction of spherical tokamaks.

Currently the largest spherical devices in the world are the National Spherical Tokamak Experiment (NSTX[23]) at Princeton, New Jersey, and MAST.

### 1.2.2 MAST

MAST was designed to follow on from the highly successful START experiment. It enlarges the vessel by a factor of 2 in every dimension, with a vessel diameter of 4m and a height of 4.4m. MAST differs from other tokamaks not just in its aspect ratio, but also in its shape, which is cylindrical with the plasma control coils mounted internally (see figure 1.3). This

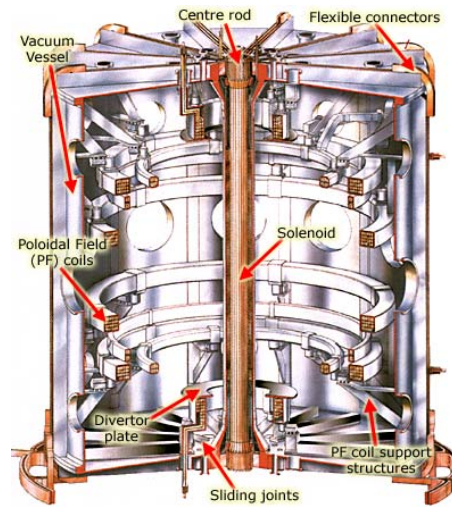


Figure 1.3: A cutaway view of the MAST vessel and coils. The cylindrical shape and internally mounted coils, which are unusual for tokamaks, can be seen. Note that this schematic shows the original MAST design, several components have since been modified (e.g. the divertor).

design was chosen to replicate the START experiment, while the NSTX vessel, built at a similar time, follows the more usual design of a shaped vessel with the coils mounted externally.

The unusual vacuum vessel shape provides excellent access to the outboard edge of the plasma for diagnostics. This contrasts with the complete lack of access to the inboard side of the plasma. Another feature of the MAST design is the ability to operate in single or double null configurations, due to presence of both upper and lower divertors (see figure 1.4).

### 1.2.3 Future uses of Spherical Tokamaks

The MAST program has so far been unable to replicate the values of  $\beta$  achieved on START due to lack of heating power [24]. This was due to the eightfold increase in the plasma volume compared with START but the retention of the same heating systems. Upgrades to the NBI systems, replacing the two old Oak Ridge National Laboratory (ORNL) injectors with two JET-style Positive Ion Neutral Injectors (PINI) are almost complete, and will

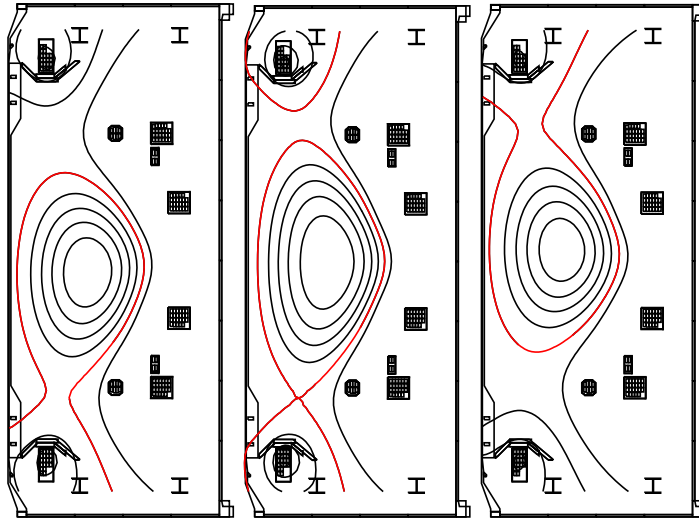


Figure 1.4: The shape of a typical MAST plasma in (left to right) lower single null (LSN), double null diverted (DND) and upper single null (USN) configurations. The last closed flux surface (LCFS) is marked in red. Data from MAST shots 14480, 18426 and 13835 respectively.

increase the NBI heating power from 3MW to 5MW. There are also plans, as part of a more general upgrade of MAST (termed MAST-Upgrade) to add 2 further PINIs, as well as significantly increasing the electron cyclotron resonance heating (ECRH) power. Other significant changes that would affect MAST are changes to the divertor from an open to a closed divertor design, to aid detachment (the screening of the vessel walls by accumulation of neutral ions [25]) and the possible use of tungsten as a divertor material.

These upgrades are directed towards establishing the regime relevant to a future Component Test Facility (CTF)[26]. This facility is aimed to be built after construction of ITER is complete: while ITER deals with plasma physics issues for a future power plant, the CTF will investigate the suitability of materials for use in a reactor by exposing them to reactor-relevant conditions (in particular neutron flux). The data from this will then be used in the first demonstration power plant, DEMO.

In order to make a CTF practical, it must be significantly cheaper than DEMO, otherwise it brings no benefit over simply attempting to build DEMO. The spherical tokamak, due to its reduced magnetic field could produce a high neutron flux at a (relatively) eco-

nomical rate[27]. Therefore there is significant motivation for spherical tokamak research both to progress towards a spherical tokamak power plant, and also to generally support the fusion program through the CTF.

### 1.3 Outline of this work

This work will attempt to improve the coverage of the atomic physics relevant to heavy species in fusion plasmas. The emphasis will be on ensuring that a baseline level of atomic data, suitable (though not necessarily ideal) for experimental analysis can be generated for any arbitrary element rapidly and consistently. The structures used allow for the use of improved atomic data where it is available.

Chapter 2 introduces the atomic physics behind the models used in this thesis. The relevant reaction processes and collisional-radiative modelling for heavy species in fusion plasmas will be discussed.

Chapter 3 demonstrates the generation of comprehensive atomic data, fulfilling the general heavy species requirements and precisions, which can now be performed in a semi-automatic manner. The product of this is called *baseline* data. It is then shown how this baseline can be built upon both by compressing the data into *superstages* to allow for use in complex plasma modelling codes, and also by tuning for use with high precision diagnostics through the substitution of higher quality data for selected stages. Illustrations of these methods are given both for spectroscopy and in enabling two dimensional transport calculations for heavy species such as tungsten.

Chapter 4 shows the results of experiments conducted introducing heavy impurities into MAST from an impurity coated probe tip, and uses such baseline data to analyse the erosion and transport of the elements into the core plasma.

In chapter 5 the charge exchange process between heavy species ions and neutral hydrogen beams is examined. Methods for extending the charge exchange recombination spectroscopy (CXRS) from the current light element provision to highly-ionised heavy species are detailed. Demonstrations are shown of how heavy species CXRS will influence diagnostic spectroscopy in the visible spectral region of ITER.

Finally, in chapter 6 the work will be summarised and future work for exploiting these

advances will be outlined.

## Chapter 2

# Relevant Atomic Physics

The emission of electromagnetic radiation caused by the interaction between ions and other particles is a phenomenon which is routinely used to diagnose all kinds of plasmas, whether astrophysical, industrial or for fusion research. Line emission observed on spectrometers can be used to both identify and quantify the various elements and the ionisation stages of those elements present in the plasma. The radiation from the impurities also reveals the character of the plasma in which they lie, such as the electron temperature,  $T_e$ , electron density  $N_e$ , plasma rotation speed and more. As well as these useful diagnostic properties, the fraction of the total plasma energy which is radiated from the plasma in a short time can be significant as a fraction of the total stored energy, therefore it is important to be able to model and understand this total radiated power. The main atomic processes shaping this radiation are discussed in section 2.1.

When considering the radiation from a plasma both the individual ion and the plasma in which it sits must be considered. For an isolated ion, the transition energies and probabilities of the emitted light depend on the quantum mechanical structure of the emitting ion. The observed wavelengths and emissivities, however, are influenced by the motion of the ion, external magnetic and electric fields, and on the excitation mechanisms for the ions in the plasma - all of which are properties of the local plasma, not the ions themselves. It is therefore useful to define two broad types of atomic data, *fundamental* and *derived*. Fundamental data consists of data relating to the individual atom (energy levels, quantum numbers, transition probabilities) and individual collision cross sections (for

electron-ion and ion-ion/atom collisions). Derived data generally incorporates the effects of many different processes on many different ions/atoms to produce a more experimentally useful quantity, such as an effective ionisation, recombination or emissivity coefficient. Since these coefficients average many collisions in the plasma, they are functions of the local plasma conditions (particularly temperature and density). This thesis is concerned with generating and using both fundamental and derived data for heavy species.

This work will largely be dealing with heavy species impurities which have not been looked at in great detail in other studies. Therefore nearly all of the atomic data used here have been generated from first principles. Typically, the theoretical wavelengths produced by such first-principles calculations are insufficient for spectroscopy. For light elements, comparison of experimentally observed spectra with calculated wavelengths allows identification of many important lines and therefore corrections can be applied to the calculated wavelengths. For complex ions such as heavy elements in fusion plasmas there are many overlapping weak features with vast numbers of lines present, making identification of individual lines impossible for all but a few valence electron ions. It is therefore not universally possible to apply the wavelength correction as is normally done for the light elements.

Most modern diagnostic spectroscopy records the spectral intensity in a wavelength region, which allows a small discrepancy in wavelength to be tolerated. Provided the wavelength can be obtained accurately enough to allow successful observation, it is the precision of the theoretical collision rate, and therefore the predicted line intensities, which limits the overall accuracy of the subsequent analysis.

Modern close-coupling methods for calculating cross sections for these collisions are based on variational principles with a finite termination of complete basis function representations. In the case of light elements, these have been extended to large basis function sets, often demonstrating convergence and therefore a good estimate of the accuracy of the cross section estimates. In the case of complex ions, calculation sizes become prohibitive with even relatively small sets of basis functions, leading to poorer accuracy which is more difficult to quantify.

Fortunately, for heavy elements the equilibrium point of the ionisation and recombination curves for an equilibrium ionisation balance tend to shift systematically to higher electron temperatures. This pushes them towards the asymptotic Born regime of the

excitation rates, which is used in this work to establish comprehensive baseline data of an acceptable precision for many studies. This Born approximation will be discussed in section 2.2.

This work forms part of the Atomic Data and Analysis Structure (ADAS) project[28]. The main goal of the ADAS project is to provide useful atomic physics data for use in fusion research, though it has also been used for analysis of astrophysical and industrial plasmas. To this end a large body of data has been calculated and/or taken from the literature and archived for use in fusion analysis. There is also work in progress amongst many ADAS collaborators to calculate further fundamental and derived data to enhance and extend the ADAS database: these projects will be highlighted when relevant to the current work.

As well as the atomic physics database, a large number of codes for generating fundamental and derived data and for analysing experiments have also been developed. A brief description of the structure of ADAS is provided in section 2.4 to aid in understanding of the computational processes and terminology used.

## 2.1 Atomic Processes in Plasmas

The electron temperatures encountered in fusion plasma research range from the 40keV predicted to exist in the core of ITER to less than 1eV in a radiatively cooled divertor plasma. The electrons thermalise rapidly in the plasma due to collisions and therefore are safely assumed to have Maxwellian distributions. The excited and ionised states of the elements in the plasma, both fuel and impurity, are sustained by collisions with these Maxwellian electrons.

The low densities and relatively small volumes of the plasma mean that the plasma is optically thin to its own emission. The only exception is in the divertor region, where the presence of significant neutral hydrogen atoms can lead to optical thicknesses of up to 2 or 3 for the Lyman series of hydrogen. There is also no external radiation field present in a magnetically confined fusion plasma. This means that for impurities photon stimulated processes, such as stimulated emission and photoionisation, are negligible.

It is found that for the effective composite rates of atomic processes scaling laws for

electron density and temperature exist. The reduced electron density is  $\rho_e = N_e/z_1^7$ , and the reduced temperature is  $\theta_e = T_e/z_1^2$ , where  $z_1$  is the residual charge of the ion  $z$  plus 1. Thus  $\theta_e$  falls off very sharply with  $z_1$ , so that three body recombination, which occurs mainly at high densities, is negligible for all but the neutral stage of elements.

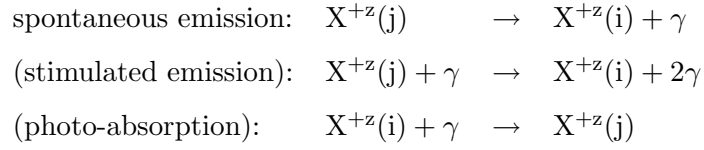
Ion-ion collisions in a thermal plasma are ineffective at transferring large quantities of energy to electronic excitation of ions, therefore they only have a significant effect on transitions with a small transition energy, such as redistribution between  $l$  subshells of high  $n$  principal quantum shells. These highly excited shells are typically populated by dielectronic recombination (DR) and charge exchange recombination (CX).

Neutral beam injectors used in fusion plasmas, usually with hydrogen but occasionally with helium or even lithium and sodium, provide a regime where ion-atom collisions are significant. The high velocity of the neutrals (typically with energies greater than 40 keV/amu) means that collisions with the plasma ions, not the electrons, dominate. Charge exchange tends to be into relatively high  $n$  shells of the receiving ion from the neutral donor, which is the starting point of the process used for charge exchange recombination spectroscopy (CXRS).

The atomic processes which affect the observed radiation are described in this section, for both radiative and non-radiative processes. Section 2.2 will explain the methods used to obtain fundamental data, while section 2.3 will describe the generation of derived data for use in experimental analysis.

### 2.1.1 Radiative Processes

The processes which lead to the emission of light from plasmas can be broken into three categories depending on the initial and final state of the electrons which cause the emission: bound-bound, bound-free and free-free transitions. Free-free transitions form the continuum emission from Bremsstrahlung due to the deflection of the electrons by the plasma ions. In the descriptions below, processes which are neglected in this work for the reasons outlined in the text are in brackets.

**Bound-Bound Transitions**

Consider the transition of an electron, from an upper state  $j$  with initial energy  $E_j$  to a lower state  $i$  with energy  $E_i$ . Both  $E_i$  and  $E_j$  are less than the ionisation potential of the ion,  $I_p$ . Decay from the upper state to the lower state can be through either spontaneous emission or stimulated emission, and the process emits a photon of energy  $E_{phot} = E_j - E_i$ . Photo-absorption is the inverse process, where an incident photon provides the energy to excite the electron. Due to the optical thickness arguments above, only spontaneous emission is significant in fusion plasmas.

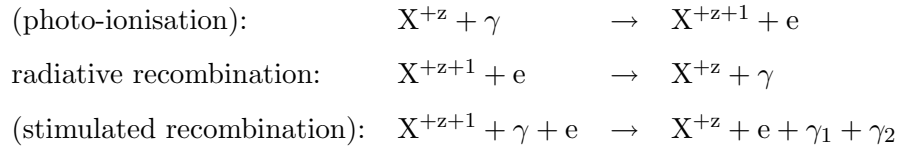
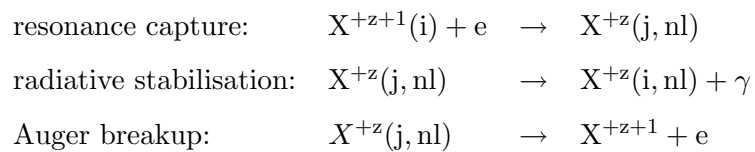
**Bound-Free Transitions**

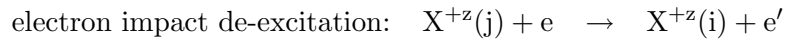
Photo-ionisation is the ionisation of an ion by absorbing incident radiation. Again, due to the optically thin nature of fusion plasmas, it is negligible for impurity ions and will be disregarded in this work. Of the inverse processes, stimulated recombination is also negligible for the same reasons, while radiative recombination (RR) is significant.

The dielectronic recombination process is also of relevance. Denote a highly excited state as  $nl$ , with  $E_{nl} > I_p$ . This state is also known as a resonance state. A collision between the electron and the ion excites a bound electron into an excited state  $j$  while the incident electron loses energy and is loosely captured into the resonance state  $nl$ . From this point it can either dissociate again from the ion (Auger breakup), or radiatively decay to a stable energy level (radiative stabilisation). The rapid capture into  $nl$  and the (radiative) Auger breakup is what gives rise to the name resonance state.



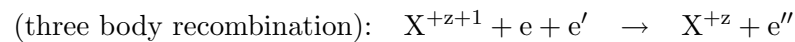
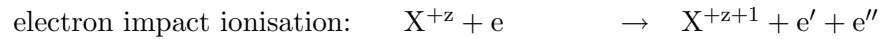
### 2.1.2 Collisional Processes

#### Electron Impact Excitation



Electron impact excitation is the main driver for populating the excited states of ions, and therefore in turn determining the quantity of photons produced for a given line. This will be returned to in some detail in section 2.2.2. The inverse process is electron impact de-excitation.

#### Electron Impact Ionisation



Three body recombination requires a high reduced density and low temperature to allow two electrons to interact simultaneously with the ion and to allow the electron to be captured. These conditions exist in the edge of fusion plasmas for neutral atoms under normal circumstances, where the effect can be significant for hydrogen. Consider, however, the difference between a hydrogen ion and a singly ionised heavy impurity. In order for recombination to take place, the electron must lose sufficient energy to allow capture. With ionised hydrogen, there is no bound electron, and therefore as soon as this happens it is captured. With a heavy impurity, the energy is more easily dissipated in the excitation of already bound electrons; for heavy ions there are many of these levels with very close energy levels, therefore the amount of energy lost by the free electron is often insufficient to allow capture. Since this work is dealing with such heavy species impurities, three body recombination will be disregarded.

The electron impact ionisation process is essentially the same as the electron impact excitation process, except that the excited electron receives sufficient energy to dissociate from the ion, either directly or through excitation-autoionisation, where the electron is excited into a high energy level from which it can either dissociate from the ion or radiatively decay back into a bound state.

### Charge Exchange



The charge exchange (CX) reaction is the transfer of an electron from one ion to another through an ion-ion collision. In thermal fusion plasmas, the donor ion is usually neutral hydrogen which exists in the plasma. The high core temperatures in fusion plasmas mean that neutrals are a significant fraction of the total hydrogen content only at the very edge of the plasma. The charge exchange reaction can therefore be considered to be limited to that region.

Modern fusion plasmas have an additional source of neutral atoms in the form of neutral beam injectors (NBI). These fire highly energetic (typically  $E > 40\text{keV}$ ), monoenergetic neutrals into the plasma to add heat and fuel. These neutrals ionise in the plasma either through electron or ion collisions. If colliding with another ion, the electron can transfer into very high energy levels of the recombining ion, resulting in emission which is useful for plasma diagnostics (this will be returned to in chapter 5). Charge exchange with neutrals from an NBI is known as beam or active CX, while reaction with other ions/neutrals in the plasma is known as thermal or passive CX.

## 2.2 Fundamental data

Fundamental data are conveniently split into one particle data (energy level and radiative transition data) and multiple (usually two) particle data (collisional cross sections). The former are simpler to obtain since they involve only the N-electron bound system. The latter comprise the N+1 electron target plus projectile system, which can have a continuum of energies and angular momentum range and may also include resonant states. However, the two calculations are closely linked, since the wave functions of the N-electron target are used as a starting point for the collision problem. As a result, in this section, the generation of atomic structure data and electron impact data will be discussed. Also, charge exchange from ion-ion collisions will also be discussed briefly, as this data was used elsewhere in this thesis.

### 2.2.1 Atomic Structure

The calculation of the atomic structure of an ion underpins all estimates of the radiation emitted from the element and its interaction with the rest of the plasma. Accurate structure data is thus a very important aspect of the prediction of emission from a plasma. The present work is concerned with establishing the baseline infrastructure of atomic modelling for all heavy species, therefore the desire for the highest possible quality data must be combined with the requirement of providing universal coverage for any required species swiftly enough to satisfy the shifting interests of fusion research. Therefore the approach here will be of moderate quality data with universal coverage, allowing selective substitution of higher quality data where available and appropriate.

Ideally, energy levels, their quantum number labels and transition probabilities would come from experimental measurements. The present situation for heavy species is, however, that there is a paucity of experimental structure data for many ions, and where it does exist it is generally incomplete and consequently insufficient for calculation of properties such as the total line radiated power. Therefore theoretical calculations are routinely used for the atomic structure instead of experimental measurements.

Such calculations are always inaccurate to some degree: typically wavelengths (which are the most easily observed measure of the accuracy of a structure calculation) calculated in this work, which will be described below, differ from experimental observations listed in the NIST atomic spectra database [29] by up to 4%<sup>1</sup>. Depending on the nature of the instruments used and spectral range under study, this can make a significant difference when considering spectroscopic observations, therefore experimentally observed energy levels and wavelengths for lines of interest should always be substituted for calculated ones for important lines to ensure the spectrometer does not “miss” them.

Consider the Hamiltonian obtained from the Schrödinger wave equation[30] for an  $N$  electron atom (where  $N > 1$ ). The Hamiltonian comprises several different parts, most simply written as:

$$H = H_k + H_{e-n} + H_{e-e} + H_{s-o} \quad (2.1)$$

where the components represent the kinetic energy, the electron-nucleus interaction, the

---

<sup>1</sup>The more advanced structure calculations mentioned in this section improve on this

electron-electron interaction and the spin-orbit interaction respectively. Solution of this Hamiltonian, provides the full energy level structure of the ion. However, one of the main problems is accurately defining the Hamiltonian in such a way that it is accurately solvable. For higher stages relativistic effects on the electrostatic and kinetic terms must be treated with increasing completeness. Also, the angular momentum coupling schemes which are appropriate for population and ionisation state modelling change in parallel.

### Coupling Schemes

In order to obtain the energy levels of an ion, an appropriate set of orthogonal basis functions must be established. In theory, the set of basis functions is infinite, however for practical computational purposes this set has to be truncated. Therefore it is important to use an appropriate set of basis functions, which is done by using appropriate angular momentum coupling schemes. Generally these are described in terms of the individual electron orbital angular momentum,  $l$ , spin angular momentum,  $s$ , total angular momentum,  $j$ , and the combinations of these  $L$ ,  $S$  and  $J$  and the associated azimuthal quantum numbers for each of these.

For the special case of hydrogen, with only one electron, there is no angular momentum coupling, and the configuration averaged, or *ca*, approach which disregards all coupling is exact. For multi electron ions, the *ca* approach can be used to rapidly obtain the centroid energy for each configuration.

The two main coupling schemes for multi electron ions are the *LS*[31] and *jj* schemes. The choice of appropriate coupling scheme depends on the relative sizes of the electrostatic term,  $H_{e-e}$ , and the relativistic terms, in particular the spin-orbit term,  $H_{s-o}$ , in the Hamiltonian.

For light ions, the electrostatic term dominates. The  $L$  and  $S$  quantum numbers are good descriptions of the states, with the spin-orbit term providing a small perturbation to these levels, which depends on  $J = L + S$ . In this coupling scheme, levels are labelled as  $^{2S+1}L_J$ .

For heavier, highly ionised ions, the spin-orbit interaction can exceed the electrostatic term. When these relativistic effects dominate, the *jj* coupling scheme is valid. In this case spin orbit effects cause the angular momenta for each individual electron to be coupled,

$j_i = l_i + s_i$ , and the electrostatic term then acts as a perturbation on this, coupling the individual  $j_i$  to give  $J = \sum j_i$  as another good quantum number. Levels in the  $jj$  scheme are labelled as  $[(l_1, s_1)j_1, (l_2, s_2)j_2, \dots, (l_N, s_N)j_N]_J$ .

In most heavy ions, however, neither term is fully dominant, and neither coupling scheme is therefore fully appropriate. In this intermediate coupling (*ic*) regime, the only good quantum numbers are  $J$  and the parity of the configuration. In this case, the Hamiltonian is diagonalised numerically, and the levels are identified by the the dominant  $LS$  configuration as  $^{2S+1}L_J$ . It is this *ic* regime that will be used most for heavy species in this work.

### Structure Codes

For ion charges  $z \geq 18$ , the structure required changes from a term resolved to a level resolved one, while relativistic terms in the Hamiltonian begin to matter. For  $z \leq 50$ , these can be modelled perturbatively using Breit-Pauli spinors. Above this, full Dirac/Breit formulation becomes necessary. It is noted that ITER is in this region, with ionisation stages of tungsten with  $z \approx 60$  predicted to exist in the core. For baseline data, complex ions mean that the code selected has to have a proven ability to deal with multiply occupied f-shells, and a history of effective use on a wide range of ions.

There are many different atomic structure codes in use by different collaborating groups, including the Cowan Code[32], Autostructure[33], the Hebrew University-Lawrence Livermore Atomic Code (HULLAC)[34], the Flexible Atomic Code (FAC)[35], and the General purpose Relativistic Atomic Structure Program (GRASP)[36]. For different ionisation stages different codes have characteristics which make them more or less suitable.

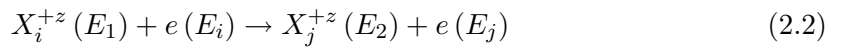
The Cowan code uses Breit-Pauli spinors and a Hartree-Fock potential[37] in its structure calculations. The Hartree-Fock method used is that of Hartree with Statistical Exchange (HX) [38, 39, 40], where the contribution of the electron-electron interaction to the Hamiltonian is obtained from statistical arguments, and the Hartree potential is then obtained iteratively. Such iterative techniques can lead to instabilities in the structure codes when there is a failure to converge for certain orbitals. This makes it sometimes necessary to omit some configurations from neutral and near neutral atom calculations

that might otherwise be desirable to include. It should be noted that this problem afflicts many codes, not just Cowan.

Both the HULLAC and the FAC codes produce above-baseline quality data, however the HULLAC code is not used here as it is a proprietary code, while the FAC package is relatively new and comprehensive experience of its use has not yet been built up. Autostructure is specially tuned for DR and RR, and produces data of above baseline quality. It has, however, only recently been extended to multiply occupied f shells, therefore this work has concentrated on Cowan as the baseline calculation, though there is no reason why the results of the optimisation methods (section 3.1.3) should not be applied by Autostructure. It is currently used heavily in conjunction with R-Matrix calculations of electron impact (see section 2.2.2). GRASP is the highest grade code considered here, and uses the fully relativistic Dirac/Breit Hamiltonian, making it suitable for heavy ions. It is the preferred source of highest quality data for ADAS, though the range of ions it can handle is too restricted to be used as a baseline data generation technique.

## 2.2.2 Electron Impact Excitation and Ionisation

The main driver for populating excited states in finite density plasmas such as those found in fusion plasmas is electron impact excitation:



where the total energy of the incoming electron and the ion are equal before and after the interaction ( $E_1 + E_i = E_2 + E_j$ ). The energy transferred to the ion excites one or more electrons to higher energy states. The cross section,  $\sigma_{i \rightarrow j}(E_i)$ , and de-excitation cross section  $\sigma_{j \rightarrow i}(E_j)$  can be calculated using a variety of methods, which are discussed in section 2.3.3.

For heavy species ions with many closed inner quantum shells, it is found that the dominant pathway to ionisation is usually excitation to auto-ionising resonance states. Direct ionisation of the inner and outer shell electrons is therefore a smaller part of the total. Typically, given the conditions of fusion research plasmas, such ions are dynamic influx ions, existing in a temperature regime above that in which they would occur for a steady state equilibrium. Thus excitation/autoionisation is further favoured. In collision

codes this route can be (and is) dealt with by treating the excitation-autoionisation route as a normal excitation collision, with multiplication by a branching ratio into the Auger breakup channel providing the ionisation cross section. Direct ionisation is accounted for by the so-called “flux loss” of bound electrons to continuum states in excitation cross-section calculations, which in close-coupling methods is included by introducing pseudo-states and complete pseudo-state expansions representing these continuum states. It is evident that there is a close connection between the ionisation and excitation calculations, and it would be artificial to try and break them up. They are therefore better treated together.

There are several different ways of quantifying and archiving electron impact information. Data is often presented as cross sections. However it is more convenient to deal with the collision strength,  $\Omega_{ij}(E)$ , which is a dimensionless quantity and also symmetrical between the initial and final states,  $i$  and  $j$ :

$$\Omega_{ij}(E) = \omega_i \left( \frac{E_i}{I_H} \right) \left( \frac{\sigma_{i \rightarrow j}(E_i)}{\pi a_0^2} \right) = \omega_j \left( \frac{E_j}{I_H} \right) \left( \frac{\sigma_{j \rightarrow i}(E_j)}{\pi a_0^2} \right) \quad (2.3)$$

where  $\omega$  is the statistical weight of a state,  $a_0$  is the Bohr radius, and  $I_H$  is in Rydbergs (1 Rydberg = 13.6eV = ionisation potential of the ground state of the hydrogen atom). Under the assumption that electrons in fusion plasmas have a Maxwellian energy distribution, the quantities of interest become the excitation and de-excitation rate coefficients  $q_{i \rightarrow j}(T_e)$  and  $q_{j \rightarrow i}(T_e)$ , described in section 2.3.2. First we introduce the Maxwell-averaged collision strength,  $\Upsilon_{ij}(T_e)$ :

$$\Upsilon_{ij} = \int_0^{\infty} \Omega_{ij}(E_j) e^{-\frac{E_j}{kT_e}} d(E_j/kT_e) \quad (2.4)$$

Then for excitation:

$$q_{i \rightarrow j}(T_e) = 2\sqrt{\pi} \alpha c a_0^2 \left( \frac{I_H}{kT_e} \right)^{\frac{1}{2}} \frac{1}{\omega_i} e^{-\frac{\Delta E_{ij}}{kT_e}} \Upsilon_{ij}(T_e) \quad (2.5)$$

and for de-excitation:

$$q_{j \rightarrow i}(T_e) = 2\sqrt{\pi} \alpha c a_0^2 \left( \frac{I_H}{kT_e} \right)^{\frac{1}{2}} \frac{1}{\omega_j} \Upsilon_{ij}(T_e) \quad (2.6)$$

Generally it is these Maxwell-averaged collision strengths which are then tabulated as a function of  $T_e$ . There are cases where non-Maxwellian electron energy distribution

functions are required, these are discussed in detail in [41] and will not be dealt with further here. Accurate theoretical calculations of collision strengths show elaborate resonance structures superimposed on a smoother background. Such features require many thousand of data points at different energies to fully describe them. Maxwell-averaging smooths over the resonances, and in the process provides a reasonably slowly varying, and therefore interpolatable,  $\Upsilon$  at fusion plasma densities.

### Calculation methods

Looking at the actual calculation of electron impact cross sections and rate coefficients, consider ionisation first. There has been considerable success in obtaining universal coverage by representing the interaction as a binary collision using the Thomson Classical formula[42]. Variants based upon this allowing for Thomson-like shell contributions with carefully selected adjustable parameters are surprisingly successful. The most successful methods allow for adjustments to account for classical exchange, non-classical high energy behaviour and have an intelligent flexible approach to effective shell ionisation potentials and equivalent electrons. Methods such as these are used for ADAS baseline ionisation rate calculations, as detailed in section 2.3.3. In this section, several codes available for obtaining cross sections of both baseline and above baseline accuracy, and therefore suitable for stage selective substitution, will be summarised. The various techniques available are listed in table 2.1. Many of these techniques are being used by collaborators with the ADAS project to improve the database of atomic data.

There are, broadly speaking, three methods available for calculating electron impact cross sections: plane-wave Born (PWB), distorted wave (DW) and close coupled methods. Excitation codes are strongly linked to atomic structure codes, which provide the target ion description: the precision of this target description limits the precision of any subsequent cross section calculation. It is therefore found that for the baseline data, and in particular for the heavy species baseline, the accuracy of the PWB approximation is acceptable, and so this method has been adopted. It is also more than sufficient for the configuration-averaged radiated power top-up estimates (see section 3.2.2). A fuller description of PWB is given below. The PWB approach is, in general, most accurate for highly ionised heavy ions. Accuracy is further improved for these ions as the intermediate

Code	Method	Usual Application	Precision	Comments
Autostructure/ Cowan	PWB with modified threshold region	Low to medium/ high Z	< 40%	Very general and stable. LS and IC coupling. No spin change. No resonances. Baseline data.
HULLAC/ FAC	Distorted wave	Medium to high Z	$\approx 20\%$	IC coupling. Includes spin change. No resonances. Matched to HULLAC/FAC structure codes.
CCC / CCC-R	Convergent close-coupling	low to medium/ high Z; 1-2 valence electrons	< 5%	Highest precision. Inefficient for many energies i.e. resonance delimitation. Limited ion scope. Being extended to Dirac relativistic.
RM / RMPS	R-matrix / with pseudostates	low to medium Z	$\approx 5 - 10\%$	High precision. LS coupling. Tuned to Autostructure structure calculation. Includes resonances. Calculates ionisation. Scripted for isoelectronic production.
RM- ICFT / RM II	R-matrix with IC frame transformation / with IC inner region	medium to medium / high Z	$\approx 5 - 10\%$	As for RM, extends to higher Z in IC. RM II improves high Z results.
DARC / DRMPS	Relativistic R-matrix / with pseudostates	low to high Z	$\approx 5 - 10\%$	As for RM. Tuned to GRASP structure calculations. IC coupling. Highest precision data, suitable for low and high Z.
RM-RD / DARC- RD	R-matrix with radiation damping	medium to high Z	$\approx 5 - 10\%$	As for RM, but extends to medium/high Z where significant radiative / Auger branching of resonances occurs.
TDCC	Time dependent close coupling	low Z, 1-2 valence electrons	$\approx 5 - 10\%$	Highest precision, benchmark for low Z ionisation.

Table 2.1: The codes available for calculation of electron impact/ionisation cross sections.

coupling (*ic*) system starts to break down in these cases, making the fact that PWB does not model spin changing transitions correctly less important. Finally, it is noted that it is straightforward for most structure codes to return the Bessel functions required by the PWB approximation, enabling rapid calculations of cross sections.

The DW codes represent more advanced perturbative, as opposed to close coupled, methods. The main examples of these are the Hebrew University Lawrence Livermore Atomic Code (HULLAC) and the Flexible Atomic Code (FAC). Both of these improve on the PWB approach, notably by correctly modelling spin changing transitions. The accuracy of these methods is however still eclipsed by the close coupled techniques, in particular with their ability to deal with resonances (which DW cannot do) and therefore it is generally R-matrix or other close coupled methods which are used when better than baseline accuracy is desired.

The main close coupled techniques are the Convergent Close Coupling (CCC)[43], the Time Dependent Close Coupled (TDCC)[44], and the R-matrix[45] methods. The CCC method produces highly accurate results but is inefficient for the calculation of resonances. TDCC produces the highest quality data available, but is only able to run for very low  $Z$  ions with only one or two valence electrons. The R-matrix methods stand out due to their good handling of resonances and efficiency at running at the many energies required to delimit them. The demands of heavy species have led to the development of several different flavours of R-matrix. For  $Z > 18$ , the relativistic terms in the Hamiltonian become more significant and there is a shift from Russell-Saunders (or *ls*) coupling to the intermediate coupling (*ic*) picture. The RM-II variant includes the complete *ic* model while the RM-ICFT[46] model includes a more efficient approximation. The DARC[47] code includes the fully relativistic Dirac approach required for  $z > 50$ . For near-neutrals where electron loss to the continuum is significant the R-matrix with pseudostates (RMPS)[48], and its relativistic version, DRMPS, are best suited. R-matrix calculations have been performed extensively for many light elements up to argon and selectively for heavier ions, particularly those with closed or near closed valence shells, e.g. Ni-like Xe[49] and W[50].

Despite significant progress in the integration of Autostructure with R-matrix and the automation of calculations [51], there remain many ions for which cross sections from these calculations do not exist. The nature of an R-matrix calculation lends itself more easily to

progression along an isoelectronic sequence as opposed to isonuclear. Combined with the significant time investment required in terms of both computing and man power it will be many years before every ionisation stage of an ion such as tungsten has been calculated. It is also not currently possible to perform such calculations on heavy element stages with several open shells. Most work that has been done for in this area has tended to focus on only one or two of the heavy elements (especially W); if information is required for any other element then little or no information will be found in the literature. Therefore it is not practical to assume that there will be complete coverage of any given heavy element by such highly detailed calculations. This provides the motivation for the steady improvement of the baseline data where it is possible, which will feature in chapter 3.

### The Plane Wave Born Approximation

A good summary of the PWB approximation is given in [52]. Here, a brief explanation is given. Returning to the Schrödinger equation[30]:

$$\left[ -\frac{\hbar^2}{2m} \nabla^2 + V(r) \right] \psi = E\psi \quad (2.7)$$

the wavefunction of an incoming electron can be described in a very similar manner to that of one electron orbiting a nucleus:

$$\psi(r) = \frac{1}{r} \mathbf{P}_{\ell l}(r) \mathbf{Y}_{l m_l}(\theta_i, \phi) \sigma_{m_s}(s_z) \quad (2.8)$$

where the quantum number  $n$  is now meaningless and the energy of the free electron,  $\epsilon$  is used instead.

In the Plane Wave Born approximation, the energy of the incoming electron is assumed to be considerably larger than the potential energy of the bound electron,  $V(r)$ , with which it interacts. This term is therefore neglected. The solution to equation 2.7 then becomes

$$\psi_f(r) = e^{ik \cdot r} \quad (2.9)$$

which is the equation of a plane wave, where  $k^2 = \epsilon =$  the kinetic energy of the electron in Rydbergs.

Upon colliding with an atom the electron is inelastically scattered, transferring energy  $\Delta E = k^2 - k'^2$  to the bound electrons, and changing the N-electron ion from state  $\alpha$  to  $\alpha'$ .

These two states are assumed to be orthogonal, although the free electron wavefunction need not be orthogonal to either. The Hamiltonian operator for the two states is then only a function of the interaction between the free electron and one or more bound electrons: all other contributions to the Hamiltonian are zero due to the orthogonality of the states.

$$H_{\alpha\alpha'} \equiv \langle \gamma e^{ik \cdot r} | H | \gamma' e^{ik' \cdot r} \rangle \quad (2.10)$$

$$= \frac{8\pi}{(k' - k)^2} \langle \gamma | \sum_m e^{i(k' - k) \cdot r_m} | \gamma' \rangle \quad (2.11)$$

This can be solved by expanding the  $e^{i(k' - k) \cdot r}$  term as a sum of Bessel functions. The cross section for the collision is then the integral over the momentum transfer  $k' - k$ , to obtain the collision strengths  $\Omega_{ij}$ .

The assumption of high incoming electron energy relative to  $\Delta E$  results in the PWB approximation being valid mostly at high energies and neutral or near neutral ions. This is to be balanced by the problems that the structure calculation encounters for the neutral and near-neutral stages. Therefore data from these stages should still be treated with some caution, while highly ionised ions are in fact found to be more accurately modelled.

Results from the PWB method can be used for line spectroscopy if a large error - estimated to be in the region of 40% - in line intensities can be tolerated. Where higher quality data is available, it is preferable to substitute it for spectroscopically important stages. For assessments of total radiated power, however, the data is of sufficient quality: errors in individual lines are masked when all the data from all transitions are totalled. Finally, when converted into the Maxwell-averaged coefficients much of the low-energy inaccuracy is masked by the high energy tail contributions.

A comparison of the spectra obtained from the Cowan Code with results from an R-Matrix calculation for  $\text{Xe}^{+26}$  is shown in figure 2.1. It can be seen from this that the two techniques produce collision strengths which lie within 40-50% of each other, and qualitatively similar spectra, therefore the Cowan code is an acceptable technique for baseline data.

### 2.2.3 Ion Impact Excitation and Charge Transfer

For excitation of ions in thermal plasmas, ion-ion collisions play a minor role compared to ion-electron collisions. The two main situations where they have a significant effect

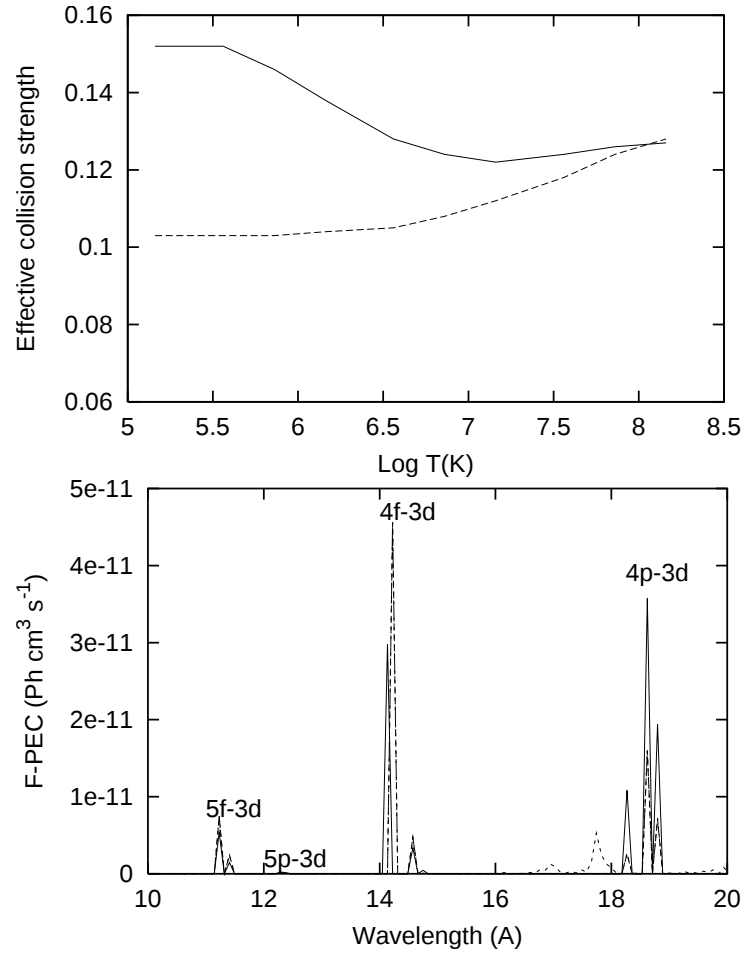


Figure 2.1: *Top:* the effective collision strengths for the  $3d^{10} \ ^1S_0 \rightarrow 4d^1S_0$  transition in  $\text{Xe}^{26+}$ : solid curve, 129CC Dirac-Coulomb R-matrix; dashed curve, plane-wave Born (baseline data). *Bottom:* equilibrium feature  $\mathcal{P}\mathcal{E}\mathcal{C}$  for  $\text{Xe}^{+26}$  at  $T_e = 550$  eV and  $N_e = 10^{13} \text{ cm}^{-3}$ : solid curve, utilizing Dirac-Coulomb R-matrix excitation data; dashed curve, utilizing plane-wave Born (baseline) excitation data; both for  $\text{Xe}^{+26}$  only. The dotted curve denotes features arising from other Xe ionization stages. Both figures from [49].

are ion impact induced transitions between target levels with very small energy levels and collision with highly energetic neutral beam atoms. The former occurs for both transitions between fine-structure levels of moderately charged ions and transitions between the nearly degenerate  $l$  subshells of high  $n$  shells. Population of these high  $n$  shells in fusion plasmas can be by either dielectronic recombination or charge transfer from highly energetic NBI ions.

For DR, both the doubly excited and the post radiative stabilisation state are susceptible to ion impact collisions. In fusion plasmas, the density is usually too low to significantly affect the lifetime of the doubly excited states, but sufficiently high that the electrons are statistically distributed among the  $l$ -subshells during the cascade. For the current baseline work, ion impact will be neglected for DR, while the cascade will be assumed to be fully  $l$  redistributed, leading to bundle- $n$  collisional radiative modelling.

Charge transfer from neutral beam atoms populates high  $n$  shells, and is the process of primary interest here. Typical energies of neutral beams are sufficiently high ( $> 40\text{keV}/\text{amu}$ ) that the beam ion speeds are considerably greater than that of the thermal ions and therefore the beam atoms dominate the collision rates.

Typically, capture from beam neutrals is into high  $n$  shells with, peaking at  $n_{crit} \approx z^{(3/4)}$ . Transitions giving rise to visible lines are usually from the  $n \approx 2n_{crit}$  shells (e.g.  $n = 8$  for  $\text{C}^{+6}$ ). For light elements, these  $n$  shells are sufficiently far apart in energy that redistribution amongst  $l$  shells is incomplete, and therefore the cross sections into each  $nl$  shell is important due to its effects on the subsequent cascade. For heavy ions the energy levels are much closer together, and collisional redistribution is, or is almost, complete, as was the case for the dielectronic recombination.

Calculation of beam-plasma charge exchange coefficients will be discussed further in chapter 5.

## 2.3 Derived Atomic Data

There are many sets of data which fall under the category of atomic physics. Not all of the data which is produced is immediately useful for practical application by experimental physicists working on a plasma physics experiment. As an example, the producers of

fundamental ion-electron and ion-ion collision data tend to produce their data as cross sections. Experimental observations tend to be of the intensity of spectral lines, and for the successful interpretation of these different types of data are more useful. It is therefore important to create data sets which are relevant and easily applicable to experiments so that fundamental data which is generated can be usefully applied to real experimental data. The most commonly used data types are the effective ionisation/recombination rates ( $S_{CD}, \alpha_{CD}$ ), and the photon emissivity coefficients ( $\mathcal{PEC}$ ), which will be defined in section 2.3.2.

To obtain this latter data type, the Generalised Collisional Radiative Model (GCR)[53] will be considered. This model considers the population of each level of an ion in relation to the various populating and depopulating processes from other levels within the same ion and in adjacent ions, and will be explored in 2.3.2.

### 2.3.1 Timescales in Fusion Plasmas

The levels of an ion can be broken down into four basic types: ground, metastable, and two types of excited state, ordinary and autoionising (or doubly excited). An ordinary excited state is one with an energy between the ground state and the ionisation limit energy, and from which decay to a lower energy state is rapid. A metastable state is defined as a low lying state from which all non-collisional decay transitions are “forbidden”, that is to say they are non electric dipole transitions. More precisely in this context they are defined as any levels whose population evolves on the same timescale as the plasma itself. An autoionising state is any excited state with sufficient energy that Auger breakup may occur, causing ionisation.

The relationship between the lifetimes of these states for a given ion are[28], for metastable states

$$\tau_m \approx \frac{10^1}{z^8} s, \quad (2.12)$$

for ordinary excited states

$$\tau_o \approx \frac{10^{-8}}{z^4} s, \quad (2.13)$$

and for autoionising states

$$\tau_a \approx 10^{-13} s, \quad (2.14)$$

For conditions relevant to fusion plasmas, the metastable lifetime,  $\tau_m$  is comparable to the lifetime of the ground state,  $\tau_g$  (which is limited by ionisation and recombination) and the timescale on which the plasma evolves (which can be thought of as the motion of ions across temperature gradients),  $\tau_p$ , such that

$$\tau_p \sim \tau_g \sim \tau_m \gg \tau_o \gg \tau_a \quad (2.15)$$

Due to the similarity in their timescales and their behaviour, ground states and metastable states are collectively referred to as metastable states. Due to the short lifetimes of excited states compared with the  $\tau_p$  and  $\tau_m$ , it is assumed that they are always in quasi-equilibrium with the metastable states. In this way the excited populations depend only on the population of the metastable states of the ion and the local plasma conditions.

### 2.3.2 Population Modelling and GCR Coefficients

The processes populating and depopulating a given excited state,  $i$  of an element can be collisional and radiative. The effect of all of these processes can be considered by using the collisional radiative matrix. Elements of this matrix are denoted generically by  $C_{ij}$ . These are rates per ion for transition from state  $i$  to state  $j$ .

Excited state populations are additionally affected by ionisation from the state to the next stage (coefficient  $S_i$ ) and recombination from the next stage (coefficient  $r_i$ ), while other stages can be ignored as coupling between ions is mostly via the metastable states.

Denote an ion of element  $X$  with charge  $z$  by  $X^{+z}$ . Excited states of this ion will be denoted with roman indices, e.g.  $X_i^{+z}$ , and metastables by greek, e.g.  $X_\sigma^{+z}$ ,  $X_\rho^{+z}$ . Metastables of adjacent ions will be denoted by  $\mu, \mu'$  for the  $X^{+z-1}$  ion and  $\nu, \nu'$  for the  $X^{+z+1}$  ion. Population densities of each state will be denoted by  $N_i^{+z}$ ,  $N_\sigma^{+z}$ ,  $N_\mu^{+z-1}$  etc. Using the convention that repeated indices are summed, i.e.  $a_{ij}b_j = \sum_j a_{ij}b_j$ , the continuity equations for population densities are:

$$\frac{d}{dt} \begin{bmatrix} \vdots \\ N_{\mu}^{+z-1} \\ N_{\rho}^{+z} \\ N_i^{+z} \\ N_{\nu}^{+z+1} \\ \vdots \end{bmatrix} = \begin{bmatrix} \vdots & \vdots & \vdots & \vdots \\ C_{\mu\mu'} & N_e \mathcal{R}_{\mu\sigma} & 0 & 0 \\ N_e \mathcal{S}_{\rho\mu'} & C_{\rho\sigma} & C_{\rho j} & N_e r_{\rho\nu'} \\ 0 & C_{i\sigma} & C_{ij} & N_e r_{i\nu'} \\ 0 & N_e S_{\nu\sigma} & N_e S_{\nu j} & C_{\nu\nu'} \\ \vdots & \vdots & \vdots & \vdots \end{bmatrix} \begin{bmatrix} \vdots \\ N_{\mu'}^{+z-1} \\ N_{\sigma}^{+z} \\ N_j^{+z} \\ N_{\nu'}^{+z+1} \\ \vdots \end{bmatrix} \quad (2.16)$$

Here  $S_{\nu j}$  is the ionisation coefficient for populating the metastable  $\nu$  of the adjacent stage from level  $j$ ;  $r_{i\nu'}$  is the coefficient for recombination from metastable  $\nu'$  to level  $i$ , and so on. Note that this equation is only complete for the  $N^{+z}$  stage as the matrix has been truncated: script coefficients ( $\mathcal{R}, \mathcal{S}, \mathcal{C}$ ) indicate pre-condensed matrices for other stages.

Using the quasi-static assumption, that is that all the ordinary level populations are in instantaneous equilibrium with the metastable populations, gives  $dN_i/dt = 0$ . The third matrix element of 2.16 then becomes

$$N_j^{+z} = -C_{ji}^{-1} C_{i\sigma} N_{\sigma}^{+z} - N_e C_{ji}^{-1} r_{i\nu'} N_{\nu'}^{+z+1} \quad (2.17)$$

This equation shows that the population of an ordinary excited level is in fact dependent only on the population of the metastable states. Reinserting this into the equation for  $dN_{\rho}^{+z}/dt$  in equation 2.16 gives the result:

$$\frac{dN_{\rho}^{+z}}{dt} = N_e \mathcal{S}_{\rho\mu'} N_{\mu'}^{+z-1} + \left[ C_{\rho\sigma} - C_{\rho j} C_{ji}^{-1} C_{i\sigma} \right] N_{\sigma}^{+z} + N_e \left[ r_{\rho\nu'} - C_{\rho j} C_{ji}^{-1} r_{i\nu'} \right] N_{\nu'}^{+z+1} \quad (2.18)$$

The right hand side gives the source terms for the population of metastable  $\rho$  in terms of the populations of adjacent ionisation stages and other metastables of the same ion. These are known as the generalised collisional radiative coefficients, which are given the suffix CD to indicate that they include dielectronic recombination effects. These are the recombination coefficient:

$$\alpha_{CD} \equiv r_{\rho\nu'} - C_{\rho j} C_{ji}^{-1} r_{i\nu'} \quad (2.19)$$

The metastable cross-coupling coefficient:

$$Q_{CD} \equiv C_{\rho\sigma} - C_{\rho j} C_{ji}^{-1} C_{i\sigma} \quad (2.20)$$

The ionisation coefficient (this relation becomes apparent by repeating the insertion of 2.17 into 2.16 for the  $X^{+z+1}$  ion):

$$S_{CD} \equiv S_{\nu\sigma} - S_{\nu j} C_{ji}^{-1} C_{i\sigma} \quad (2.21)$$

There is also the coefficient for coupling between metastables via recombination to the parent metastable and then re-ionisation:

$$X_{CD} \equiv -N_e \left[ S_{\nu j} C_{ji}^{-1} r_{i\nu'} \right] \quad (2.22)$$

Finally, there is the process of charge exchange recombination. This has been omitted in the previous discussion, but adds another method of populating the excited state  $i$  by recombination from the parent ion. This is similar to recombination, except that the driver is the neutral hydrogen density,  $N_H$ , not  $N_e$ , and the coefficient is denoted by  $L$ , not  $R$ :

$$C_{CD} \equiv L_{\rho\nu'} - C_{\rho j} C_{ji}^{-1} L_{i\nu'} \quad (2.23)$$

The calculation of these coefficients will be discussed in the next sections for the  $\alpha_{CD}$  and  $S_{CD}$  cases. The heavy species data generated in this thesis assume that each ionisation stage has only one metastable - the ground state - and therefore there is no need for the  $X_{CD}$  and  $Q_{CD}$  terms to be discussed. This is known as the *unresolved* case, and the model is the collisional-radiative model (CR), whereas when several metastables are included for each ion it is known as the (metastable) *resolved* case, and the model is the generalised collisional-radiative model (GCR). Details of the GCR model have been included because of their relevance to superstaging, discussed in chapter 3.

### Photon Emissivity Coefficients

The emissivity of a spectral line,  $\epsilon_{j \rightarrow k}$ , is the total emission from a transition from state  $j$  to  $k$ . This is equal to the sum of the rate for each of the processes populating state  $j$ , multiplied by the Einstein  $A_{j \rightarrow k}$  coefficient for spontaneous emission. It is useful to define a photon emissivity coefficient,  $\mathcal{PEC}(T_e, N_e)$  which is a function of local temperature and density such that

$$\epsilon_{j \rightarrow k} = \mathcal{PEC}_{j \rightarrow k} N_e N^{+z} \quad (2.24)$$

These  $\mathcal{PEC}$ s can then be tabulated and stored (in ADAS they are stored as ADF15 files). The  $\mathcal{PEC}$ s allow the emission from a volume of plasma by an impurity to be estimated from knowledge of  $T_e$ ,  $N_e$ , and the impurity density  $N^{+z}$  alone. Of these,  $N^{+z}$  is usually the hardest to determine, requiring a combination of ionisation balances and/or modelling of transport of impurities in the plasma.

Another useful quantity is the number of ionisations per photon ( $S/XB$ ) for a given transition, known as  $\mathcal{SXB}$ . This quantity is frequently used in regions of the plasma where ionisation dominates over recombination to obtain an estimate of local impurity density, particularly, for example, near an impurity source at the edge of the plasma. The  $\mathcal{SXB}$  is defined as:

$$\mathcal{SXB}_{\sigma,j \rightarrow k} = \frac{S_{CD\sigma \rightarrow \nu}}{\mathcal{PEC}_{j \rightarrow k}} \quad (2.25)$$

When dealing with heavy species, some with many thousands of overlapping lines, storage of  $\mathcal{PEC}$  data for each transition becomes both wasteful of disk space and no longer particularly informative. For this reason, a wavelength resolved feature photon emissivity coefficient, ( $\mathcal{FPEC}$ ) has been created. This file tabulates the sum of the Doppler broadened  $\mathcal{PEC}$ s for all transitions of an ion as a function of wavelength, producing the spectra due to each ion, not the individual line  $\mathcal{PEC}$ . Again, this is a function of  $T_e$  and  $N_e$ .  $\mathcal{FPEC}$  files are stored within ADAS as ADF40 files.

### 2.3.3 GCR Coefficient Simplifications

The description in section 2.3.2 is the most complete form of the collisional-radiative model. It can, however, only be implemented at a high precision if all the fundamental data ingredients in section 2.2 are available. At the present time, and for the foreseeable future, this is only possible for a few selected ions of special diagnostic interest. Fortunately, it is also only necessary for approximately the same selection of ions. In this section the progressive simplification of the GCR sub-matrix is described, reducing the accuracy of the data but providing universal coverage in exchange. The reduction in accuracy is acceptable for baseline data: since the quality of the derived atomic data is dependent on the quality of the fundamental data, application of full GCR modelling to the baseline quality fundamental data would not actually provide more accurate coefficients, and

therefore simplifications are not detrimental.

For baseline quality data, the only data which is available for use in the calculation of CR coefficients is the set of energy levels, transition probabilities and collisional rate coefficients obtained from the Cowan Code. There are no separate state selective ionisation and recombination data sets available. Consider the 2x2 submatrix of equation 2.16, containing  $C_{\rho\sigma}$ ,  $C_{\rho j}$ ,  $C_{i\sigma}$  and  $C_{ij}$ . Split the ordinary excited states  $i$  and  $j$  into low lying (those responsible for emission) and high lying (as  $n \rightarrow \infty$ ). The Cowan data fills in the  $C_{\rho\sigma}$  and the low lying parts of  $C_{ij}$ . It is noted that the Born approximation used by Cowan does not calculate spin changing transitions, therefore the coefficients for these are unsound, which will affect in particular  $C_{\rho\sigma}$ . This is mitigated by two factors: for highly ionised elements the concept of metastables breaks down, therefore the  $C_{\rho\sigma}$  reduces to just the ground state. Also, for heavy species the energy between the ground and metastables is small, therefore the coupling would be strong and the populations can be approximated as Boltzmann distributions: introducing an artificial coupling to represent this again reduces the  $C_{\rho\sigma}$  to just the ground state. To all intents and purposes the metastable state can be treated as another excited state, and even if the coupling between it and the ground is not accurately modelled, the build up of population in this level is no longer so large that the overall effect is significant. This reduction to a 1x1 matrix is assumed for the baseline derived data.

Collisional couplings for the  $C_{\rho j}$ ,  $C_{i\sigma}$  and the low lying  $C_{ij}$  are dominated by non-spin-changing transitions, and therefore the calculations of Cowan are sound. The high lying  $C_{\rho j}$  and  $C_{i\sigma}$  cause only a small correction, and therefore can be omitted or, as in this work, be modelled in the configuration averaged approach. The high lying  $C_{ij}$  are filled usually by recombination, not excitation. Use can be made of a threshold quantum shell,  $n_{crit}$ , above which ions undergo Auger breakup, and below which the electron cascades to the ground. Thus the high level part of  $C_{ij}$  and the recombination submatrix  $r_{i\nu'}$  may be omitted.  $r_{\rho\nu'}$  can be replaced with the term where  $\rho = 1$ , which includes a sum over the submatrix  $r_{i\nu'}$  for  $i \leq n_{crit}$ . Similarly, ionisation into the high lying  $j$  will be small and therefore  $S_{\nu j}$  can be neglected.

In general the individual collision strengths for line emission require detailed modelling as their impact on the spectra radiated from the plasma is highly significant, as shown in

section 2.2.1. By contrast, the CR  $S_{CD}$  and  $\alpha_{CD}$  coefficients can be obtained from a variety of semi-empirical formulae when advanced methods are not available. Within ADAS there are a pair of routines, ADAS407/408, which generate the CR coefficients based upon the contents of an ADF04 file and some of these empirical formulae. This file contains, for one ionisation stage of an ion, the energy levels, Einstein  $A_{j \rightarrow k}$  coefficients and collision strengths for each level and transition between levels. The final CR coefficients are stored as ADF11 files.

There are two sets of empirical formulae used to generate these coefficients, collectively called case A and case B. The case B formulations are more advanced than the case A, however there have been stability issues with the Case B calculations for DR. Therefore previous experimental interpretation usually relies on a mix of case A and case B as appropriate. An outline of the approximations used in each case is given in this section, along with the method for estimating the power radiated by the processes involved.

### Ionisation Rate Coefficient, $S_{CD}$

In the Case A approximation the semi-empirical formulation of Lotz[54] for electron-impact ionisation is used. In this case the cross section,  $\sigma$  is:

$$\sigma(E) = \sum_{i=1}^N 4.0 \times 10^{-14} \left( \frac{I_H}{I_i} \right)^2 \left( \frac{I_i}{E} \right) \ln \left( \frac{E}{I_i} \right) \zeta_i \quad (2.26)$$

where  $N \leq 2$ ,  $E$  is the incoming electron energy in eV,  $\zeta_i$  is the number of equivalent electrons,  $I_i$  is the ionisation potential for electrons in the shell  $i$ , where  $i = 1$  is the outermost shell,  $i = 2$  the second outermost and so on. Converting to a rate coefficient,  $S_{CD}$ , gives:

$$S_{CD}(T_e) = \sum_{i=1,2} \left\{ 1.42^{-6} \left( \frac{I_H}{kT_e} \right)^{3/2} a \zeta \left[ \frac{E_1(I_i/kT_e)}{I_i/kT_e} - \frac{be^c E_1(I_i/kT_e + c)}{(I_i/kT_e + c)} \right] \right\} \quad (2.27)$$

Where  $E_1$  is the first exponential integral, and  $a, b$  and  $c$  are constants given for each shell.

The Case B approximation improves upon this picture by including not only direct electron-impact ionisation, but also excitation-autoionisation. The formulation used here is that of Burgess and Chidichimo[55], with the cross section given by:

$$\sigma(E) = C \sum_i W(E/I_i) \left( \frac{I_H}{I_i} \right)^2 \left( \frac{I_i}{E} \right) \ln \left( \frac{E}{I_i} \right) \zeta_i \quad (2.28)$$

Where  $W(E/I_i)$  is a threshold parameter, introduced to account for the deviation from linear behaviour near the ionisation threshold. In order to account for the effects of excitation/autoionisation, adjustments are made to the ionisation potential  $I_i$  and number of equivalent electrons  $\zeta_i$ , as described in [56]. The values of these adjustments were obtained by fitting against the experimental data available at the time of the paper. Again, converting to a rate coefficient, the result is:

$$S_{CD}(T_e) = \sum_I c_I \sum_{i \in I} 2.1715^{-8} c \zeta \left( \frac{I_H}{I_i} \right)^{3/2} \left( \frac{I_i}{kT_e} \right)^{1/2} E_1(I_i/kT_e) W(E/I_i) \quad (2.29)$$

A comparison of the results for  $S_{CD}$  calculations for the two cases is shown in 2.2. Due to the significant contributions that excitation-autoionisation makes to the ionisation rate, case B will be used in the rest of this thesis.

### Recombination Rate Coefficient, $\alpha_{CD}$

Both dielectronic recombination and radiative recombination are treated separately due to the need to account for the capture or Auger breakup from autoionising states in the dielectronic recombination reaction. Radiative recombination is modelled using hydrogenic formulae in both case A and case B. Capture into excited  $n$ -shells up to a cut off  $n_{crit}$  is treated as purely hydrogenic with a unit Gaunt factor. Above  $n_{crit}$ , which is determined by the difference in energy between the recombining and recombined ion it is assumed that electrons autoionise. For capture to the ground state, the hydrogenic picture can be improved upon by use of an occupancy phase factor to account for other electrons in the recombining ion's valence shell. In case B, the effective principal quantum number is used instead of the actual principal quantum number, while a temperature dependent factor is also introduced. The case B approximation will be used for radiative recombination throughout the rest of this thesis.

For dielectronic recombination the Burgess general formula[57] is used to calculate the case A cross sections. The dipole transitions from the ground state are split into two groups, typically corresponding to  $\Delta n = 0$  and  $\Delta n = 1$ . The general formula is used for both sets and summed, then a density dependent multiplier is applied to account for re-ionisation from high  $n$  shells. The case B uses a basic implementation of the Burgess Bethe General Program[58], which explicitly calculates and then sums the coefficients for each

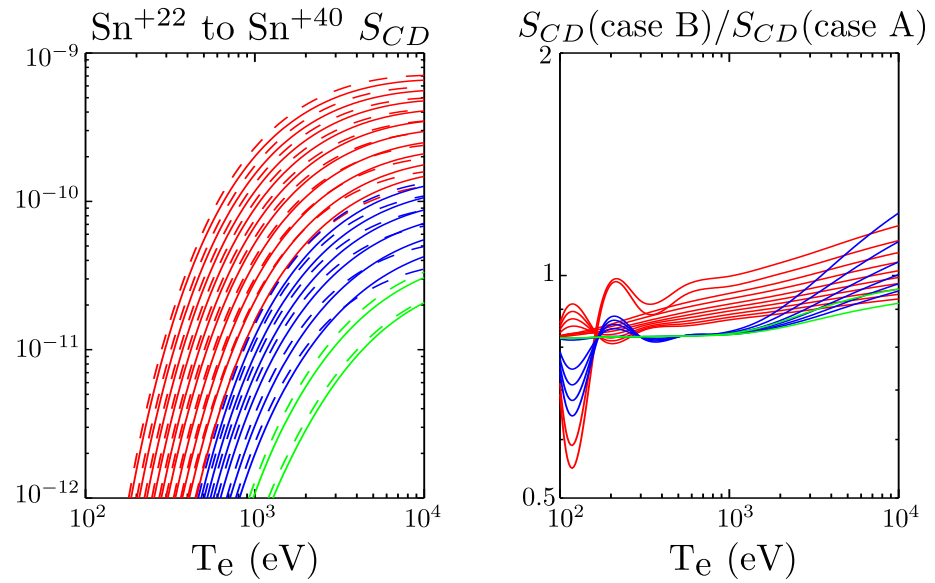


Figure 2.2: The  $S_{CD}$  ionisation coefficients for the  $n = 3$  shell of Sn. The lines are colour coded depending on the  $l$  quantum number of the outermost electrons in the ground state: red is the  $d$  shell, blue is the  $p$  shell and green is the  $s$  shell. In the left hand plot, the dashed line indicates the case A coefficient, and the solid the case B. The right hand plot shows typical ratios for the case B to the case A coefficient. The ringing at low temperature is due to the division of two very small numbers, and is not, therefore significant in experimental analysis.

$nl$  shell and then applies the density reduction multiplier more precisely. The transitions are again split into groups, although this time more carefully according to the change in  $n$  and  $l$ . This allows the application of specific Bethe correction factors for each transition set.

Unfortunately, the Case B approximation occasionally fails due to a numerical instability (currently, in approximately 5% of stages for tungsten). Work is ongoing to resolve this issue. A comparison of data for several stages of Sn in the case A and case B approximations for DR and RR is shown in figure 2.3. Clearly there are significant differences between the two for the DR case, and it is the case B data that is a significant improvement over the case A. Since it is possible to interchange case A and case B data for individual stages, use of case B data for individual ions where the calculation is stable would be preferable. However, since this work is dealing with baseline data with the requirement that such data be easily generated and reliable, and that the errors in the case B case must raise questions about the calculations accuracy, for consistency the case A approximation will be used throughout this work for DR.

### **Radiated Power coefficients, $\mathcal{PRB}$ , $\mathcal{PRC}$ and $\mathcal{PLT}$**

The power radiated by the recombination, excitation and charge exchange processes are divided into three separate coefficients, the  $\mathcal{PRB}$ ,  $\mathcal{PRC}$  and  $\mathcal{PLT}$  coefficients for recombination-bremsstrahlung, thermal charge exchange and electron impact excitation. Of these three, the  $\mathcal{PLT}$  is usually dominant, and is certainly so for heavy elements in fusion plasmas. A comparison of the  $\mathcal{PRB}$  and  $\mathcal{PLT}$ , and the relative magnitude of the contributions of the processes discussed below for each, is shown in figure 2.4

The  $\mathcal{PRB}$  coefficient contains radiation stemming from cascades where initial population of the excited state is due to a recombination event, either DR or RR. To this is added the Bremsstrahlung contribution to the radiation. All three of these processes are treated identically in both case A and case B, though for the DR and RR this is based upon a different rate coefficient.

Bremsstrahlung, which arises from deflection of free electrons by the electrostatic field of the ions in the plasma, is assumed to be hydrogenic, with a Gaunt factor of unity,

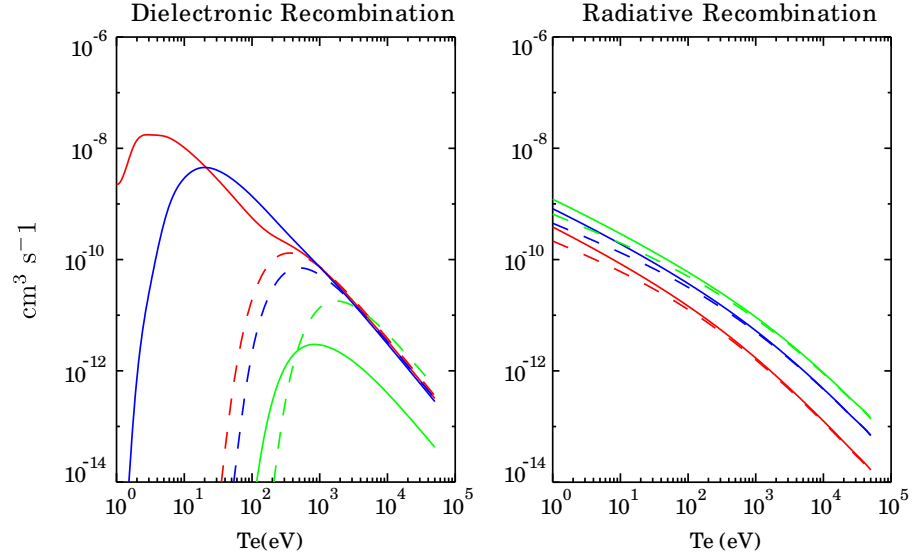


Figure 2.3: A comparison of the contributions to the  $\alpha_{CD}$  recombination coefficient for (left) dielectronic and (right) radiative recombination for selected stages of tin. Red:  $\text{Sn}^{+23}$ , Blue:  $\text{Sn}^{+32}$ , Green:  $\text{Sn}^{+38}$ . The solid line is case B and the dashed line is case A. Significant discrepancies are noted between the two cases for dielectronic recombination, with case B being a significant improvement over case A.

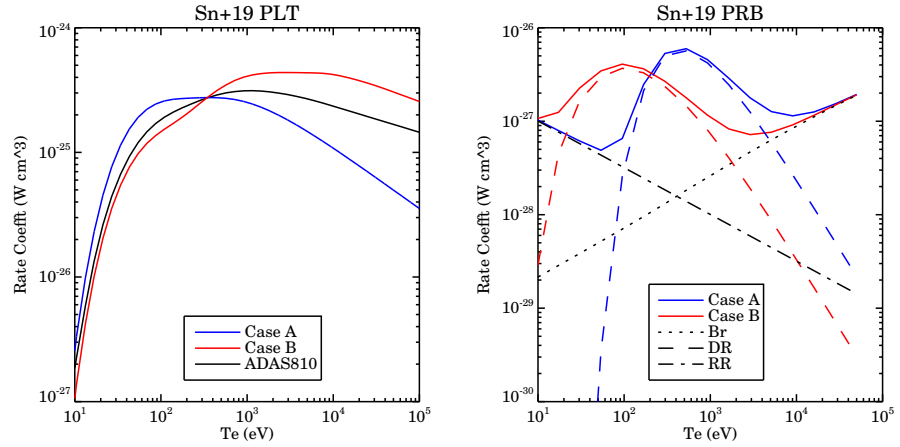


Figure 2.4: The collisional radiative excitation line power,  $\mathcal{PLT}$ , and recombination-bremsstrahlung radiated power,  $\mathcal{PRB}$ , for  $\text{Sn}^{+19}$ . For  $\mathcal{PRB}$  data, the bremsstrahlung (Br) and radiative recombination (RR) are identical in case A and case B.

giving:

$$P_B = 5.7 \times 10^{-32} z_1^2 \left( \frac{kT_e}{I_H} \right) W cm^3 \quad (2.30)$$

The  $z_1^2$  dependence of radiated power is why heavy species impurities are unwelcome in a fusion plasma: they are efficient radiators of plasma energy and therefore high concentrations of them cannot be tolerated.

For RR, the radiated energy per reaction is assumed to be the ionisation potential of the recombined ion. The energy radiated by a DR event is equal to the stabilisation photon energy plus the cascade energy (equal to the parent transition energy plus the ionisation potential).

The energy radiated by a charge exchange reaction is taken to be the ionisation potential of the recombined ion, as with RR. This is tabulated separately in the *PRC* file as the reaction rate is dependent on neutral hydrogen density, not electron density.

As stated earlier, by far the dominant part of the radiated power is the line emission from excitation, not recombination, tabulated in the *PCT*. This is treated differently in both case A and case B. In both cases, the zero density assumption that all excitation leads to spontaneous emission is made. In case A, the transitions are split into two groups as for DR in case A. The radiated power coefficient is then the energy weighted sum of the excitation rate coefficients for the groups evaluated in the simple effective Gaunt factor approximation. In case B, the total radiant power is first evaluated by summing every transition energy weighted excitation rate coefficient from the ground in the ADF04 file at every tabulated electron temperature. Then the two groups are considered, as for Case A, but with the effective Gaunt factor replaced by the Van Regemorter[59] temperature dependent P function. Adjustable parameters multiply the two groups. In Case B, these parameters are optimised against the explicitly summed zero density *PCT* to give the values for archiving.

It is noted, however, that once the collision strengths have been calculated for an ion, which will routinely be done as part of this work, it is possible to calculate the actual total radiated line power simply by summation instead of using a formula and fit. Therefore for most of this work the preferred approach will be to use the *PCT* calculated in this manner. Since the ADAS code used to generate this data is ADAS810, this shall be known

as ADAS810 data to differentiate it from case A and case B when necessary.

## 2.4 ADAS

The ADAS package, which is used extensively throughout this thesis, consists broadly of two separate parts. The first is an archive of atomic data, taken from experiments or calculations reported in the literature, or calculated using the ADAS codes. The second part consists of the ADAS codes: as well as data access routines to the database, these include complex codes for the generation and/or use of the atomic data available (examples so far mentioned include the Cowan structure code, which is implemented in ADAS as ADAS801, and the CR coefficient generation routines ADAS407 and ADAS408).

The database consists of files for many different types of atomic data. All are stored as ADAS Data Format (ADFxx) files, with the ‘xx’ a number indicating the data class. Those used in this thesis are listed in table 2.2. Data files generally contain the exact calculated values of a particular quantity (e.g. photon emissivity coefficient) on a grid of energies, temperatures, densities or other factors as appropriate. When extracting data, interpolation is used to obtain data for values between those on the grid.

Other data formats are driver files for codes within ADAS (e.g. ADF34, which is a driver data set listing the configurations to include in the structure calculation in ADAS801). Extensive use is made of such driver files throughout ADAS. To enable reproduction or adjustment of calculations it is often more beneficial and efficient to archive these driver files than the calculation results, and therefore they are archived as ADAS Data Formats.

The codes within ADAS are all identified by three digit codes, e.g. ADAS801. The first digit refers to the ‘series’ of codes: for example, series 8 codes are all concerned with calculation of atomic structure, while series 4 deals with ionisation and recombination. Frequently, to obtain the required data, it is necessary to use a chain of codes and data files within ADAS (see, for example, figure 3.1). This system provides frequent break points at which improved data can be substituted if required, for example an improved ADF04 specific ion file could be substituted after an ADAS801 run (to obtain the structure) but before ADAS810 is initiated (to obtain the  $\mathcal{P}\mathcal{E}\mathcal{C}$ s). A list of the codes used in this work is

File	Description
ADF00	Ground configurations and ionisation potentials.
ADF01	Bundle-n and bundle-nl charge exchange cross sections
ADF03	Parameter sets for generating recombination and ionisation coeffs.
ADF04	Specific ion fundamental data collections
ADF11	Iso-nuclear CR coefficients
ADF12	Charge exchange effective emission coefficients
ADF15	Photon emissivity coefficients
ADF26	Bundle-n and bundle-nl populations of excited states in beams
ADF34	Driver data sets for ADAS801 (Cowan code)
ADF40	Feature photon emissivity coefficient
ADF42	Driver data sets for ADAS 810
ADF49	Master files for charge exchange extrapolation
ADF54	Promotional rules files for ADAS808

Table 2.2: The ADAS data formats used in this work.

Code	Description
ADAS315	Generate arbitrary species CX cross sections
ADAS316	Bundle-n CX emissivity generation
ADAS407	Prepare iso-nuclear parameter sets
ADAS408	Prepare iso-nuclear master data from parameter sets
ADAS416	Superstages - repartition ADF11 datasets
ADAS801	Cowan Structure Code
ADAS808	Prepare driver files for ADAS801
ADAS810	Generate $\mathcal{PEC}$ and $\mathcal{FPEC}$ .

Table 2.3: The ADAS codes used in this work.

given in table 2.3

## Chapter 3

# Improved Heavy Species Baseline Calculations

### 3.1 Motivation

Analysis of spectroscopic observation of impurity ions in plasmas has long been a staple of tokamak diagnostics. Successful interpretation of these observations requires several different types of derived atomic data. In this chapter the mechanics of generating such data for an arbitrary element will be discussed, and improvements to the framework for this will be described.

Until recently, calculation of atomic physics data concentrated on the light elements - those with  $Z \leq 26$ . This was due to a combination of computational limits (these calculations are much smaller, and models are closer to being accurate) and also the fact that these elements were those of interest to the fusion and astrophysics community. Therefore a great deal of effort has been spent on generating high quality atomic data for these elements. With the move from mostly carbon lined machines (e.g. JET and ASDEX-U) to ones containing large areas of tungsten (ASDEX-U today, ITER when built and the JET ITER-like wall project) there is a need for coverage of a different range of ions.

The move to these heavier elements, with vastly increased number of stages, also introduces some practical limits, some human, some computer based. Previously, the most studied impurity elements were light ones, particularly carbon. Carbon has only six

stages, all with a fairly simple atomic structure. This makes detailed examination of data for each stage to check for defects, omissions, or other problems feasible. With the move to larger elements, manually reviewing 74 stages of tungsten data becomes less practical. The size of the data files (the Maxwell-averaged rate coefficients for tungsten used in this work total more than 1.5Gb) produced for stages with complex electron structure, as well as the number of stages being dealt with, require an attempt to make the process more robust through greater automation to ensure that self-consistent data are produced and that this data can easily be used in further modelling.

As an example, Sn and In were used in the experimental section of this study, but many other elements were investigated but then rejected (Ag, Au, Hf, Pd and others). There is little data in the literature for these elements, and generation of very high quality data for them would not have been possible if it had been required. Therefore the baseline models described in section 2.2.2 were used to rapidly provide the required data.

These *baseline* calculations must meet several requirements to be of practical use to experimental physicists. The first requirement is that the models used must be accurate enough to be useful for experimental analysis - there is no point in producing completely inaccurate data. The second requirement is that the codes used to generate this must be sufficiently robust so that an inexpert user can create the required data<sup>1</sup>. The third requirement, linked to the second, is that the codes should be as robust as possible, to avoid constant crashes, exceptions and work-arounds which frustrate the use of baseline data. The fourth requirement is that they should be able to run in a reasonable amount of time. Again, reasonable is a relative term, but waiting many years to generate data to analyse an experiment is clearly not ideal (see, for example, the Iron Project[60], which is still ongoing after 13 years). Finally, as the data is only of baseline quality, ideally the model and implementation should be sufficiently modular that where higher quality data is available and useful it can be substituted for the baseline calculation to improve results.

The modular format of the ADAS codes allows for substitution of improved data where available. The codes for generation of the baseline data have, however, proved to sometimes be less robust than is ideal, and certainly byzantine to anyone not deeply familiar with

---

<sup>1</sup>Inexpert is here a relative term; some familiarity with atomic physics is to be expected, but not necessarily with the underlying computer codes that produce the data.

the underlying system. Therefore the opportunity was taken in this work to improve the robustness of the codes and their application to plasma diagnostics.

### 3.1.1 Electron Impact Excitation Cross-Sections

The baseline technique used for generation of electron impact excitation cross sections is the Cowan Structure Code (see section 2.2.1), implemented in ADAS as ADAS801. The Cowan code generates the atomic structure, then implements the Plane Wave Born (PWB) method to calculate the electron impact excitation cross sections.

The important results to note here are the range of validity for the data. The PWB model does not include any mechanism for the effects of resonances which typically occur at lower energies. Therefore the model works better when the energy of the free electron is considerably greater than the energy transferred to the ion. The model also performs better for near neutral stages, however this is tempered by the fact that the structure calculation becomes less reliable in this limit; in general the net result is that data for higher ionisation stages is deemed to be more robust.

As electron impact excitation is the main method for populating excited states of atoms in fusion plasmas, these calculations are the most important for the generation of  $\mathcal{PECs}$ . Ideally for transitions of interest the data for lines of spectroscopic important data from more sophisticated techniques would be used, but if no such data is available then this data can be used provided a wide margin of error ( $\approx 40\%$ ) is acceptable.

When dealing with more general quantities, such as total radiated power (of interest when dealing with impurities cooling the plasma, for example) the inaccuracies in individual lines become less important. This makes this method generally acceptable for such measurements.

To obtain cross sections, a calculation of the atomic structure is required first. Assuming that the calculation method has already been decided (in this case, the Cowan code), the other main factor which influences the results and the calculation size are the included configurations. Optimally, for baseline calculations, the configurations selected should allow the calculation to (a) be performed relatively quickly (in this case, roughly less than a day per ion), (b) include any lines required for spectroscopic purposes and (c) work - there is no point in running codes that become unstable and produce unreliable

results.

The lower limit on this calculation size is to ensure that the configurations involved in all the relevant/interesting transitions are included. The upper limit can be both computer processing time/memory available and hard coded limits on the dimensions of the calculations with the Cowan Code. Both of these limits can be changed to a degree, but there is limited benefit in pushing such a calculation to infinite size. The final limit, requiring stability, is usually only an issue for neutral and sometime singly ionised ions, where the code frequently fails while calculating individual electron wavefunction. No satisfactory solution to this problem has yet been found excluding omitting the offending configurations from the calculation, therefore this is what has been done in this work.

Due to the vast amounts of data being produced by these codes for heavy elements, a high degree of automation and scripting has been implemented in the code, resulting in the main inputs being simply the coupling scheme to be used in the calculation (intermediate coupling (*ic*), Russell-Saunders coupling (*ls*)[31] or the faster, less detailed configuration averaged (*ca*) approach) and the list of configurations to be included. A brief description of the coupling schemes is given in section 2.2.1.

Once the code has finished the outputs are the ion's energy level structure, the collision strengths between levels within the ion, and Einstein A-values for transitions between each of the levels present. These are provided in an ADF04 data format to enable further processing by other ADAS codes. At this point, if improved data was available for some stages, it could be swapped in by replacing or amending the relevant ADF04 file. Further processing can then be performed to produce  $\mathcal{P}\mathcal{E}\mathcal{C}$ s (code ADAS810) and GCR coefficients (ADAS407/408); again if better estimates for these values exist they can be used instead. Figure 3.1 shows an outline of this chain of codes.

### 3.1.2 Configuration Selection by Promotion Rules

The main complexity in initiating Cowan's Code for an entire element is usually the correct selection of the configurations to be used for each stage in the calculation. In an attempt to simplify this process, a code has been written which selects the configurations to be included and then generates all the relevant driver files for an ADAS801 calculation based upon a set of (user-editable) rules. This code is now part of ADAS as ADAS808. The

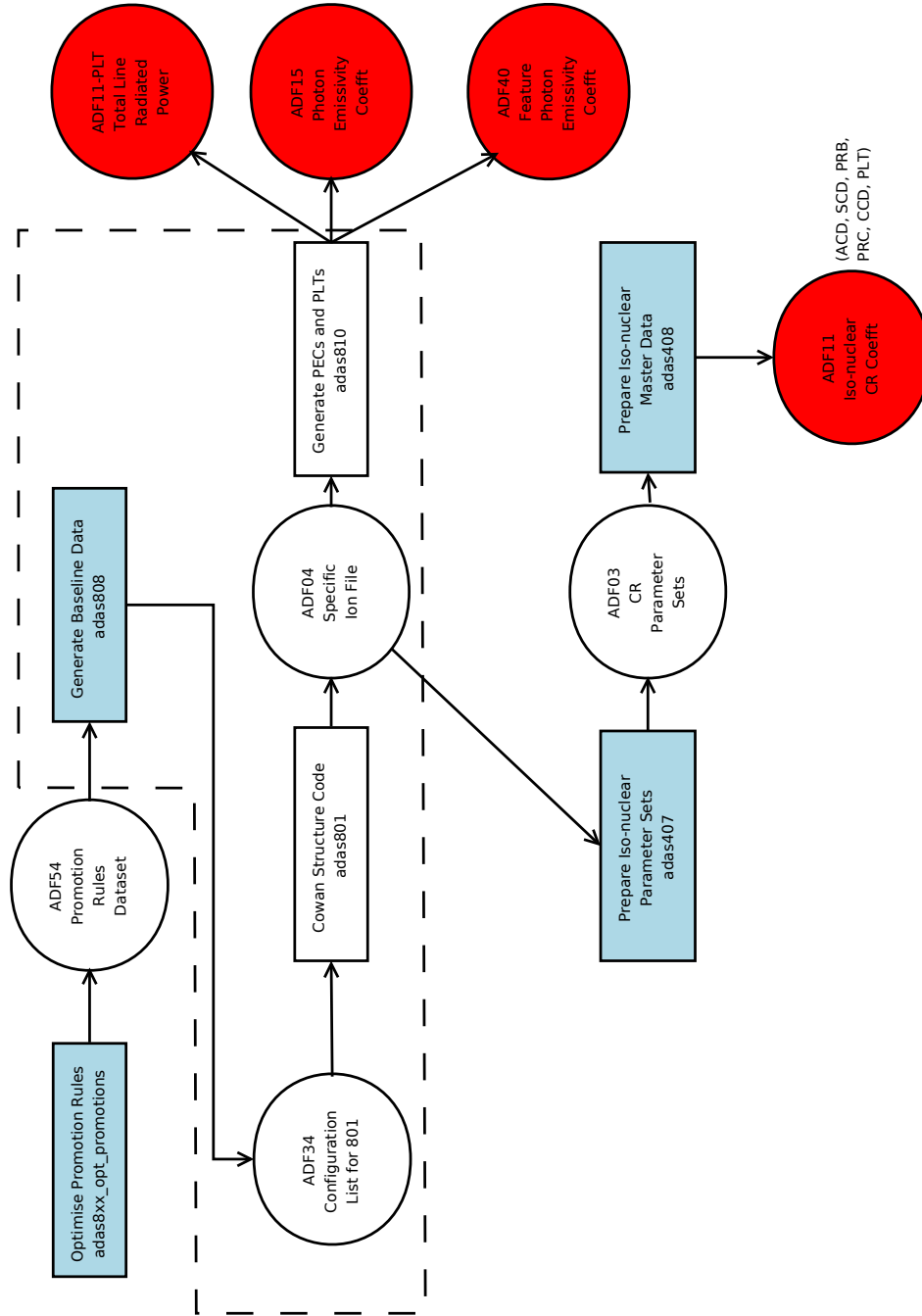


Figure 3.1: A schematic of the adas8xx code suite. Rectangles indicates codes, with white box codes running automatically and blue requiring manual initiation. Circles indicate files, with red circles indicating derived data useful for experimental analysis.

code functions by reading in the ground configuration of the element, and consulting a table of promotion rules (archived as an ADF54 file). These rules list changes that can be made to this ground configuration to obtain new configurations to put in the calculation. Three sets of these rules have been generated, for different sizes of computers, with the promotion rules therein being selected manually to provide a master list of rules.

Consider an atom of neutral tungsten ( $W^0$ ) as an example. This element has a complete set of core shells up to  $4f^{14}$ :

$$1s^2 2s^2 2p^6 3s^2 3p^6 3d^{10} 4s^2 4p^6 4d^{10} 4f^{14}$$

and an outer part:

$$5s^2 5p^6 5d^4 5f^0 5g^0 6s^2$$

This configuration consists of two closed shells (5s and 5p), 2 empty shells (5f and 5g) and 2 open active valence shells (5d and 6s). Different promotion rules define the range of promotions which can be made. There are separate rules dealing with n and l shell promotions from the first valence shell (6s), the second valence shell (if present, in this case 5d) and closed shells (the exact range of which can be defined later, but may for example include 5s and 5p). For example, one pair of rules dictates the change in n shell allowed from the 6s valence shell:

$$\delta n_{v1_{max}} = 1$$

$$\delta n_{v1_{min}} = 1$$

These rules would allow the 6s electron to move to any nl shell with  $n_{v1} + n_{v1_{min}} \leq n \leq n_{v1} + \delta n_{v1_{max}}$ . In this case, since the 5s shell is full, this would add only the configuration (omitting the inner part for brevity)

$$5s^2 5p^6 5d^4 5f^0 5g^0 6s^1 7s^1$$

Similar rules exist for limiting the range of l shells which electrons can be promoted to.

$$\delta l_{v1_{max}} = 2$$

$$\delta l_{v1_{min}} = -1$$

Adding this expansion would allow transitions to any nl shell which meets the criteria  $l_{v1} + \delta l_{v1_{min}} \leq l \leq l_{v1} + \delta l_{v1_{max}}$ . Combining with the above rules for n, this would now add the configurations

$$\begin{aligned}
 &5s^2 5p^6 5d^5 5f^0 5g^0 6s^1 \\
 &5s^2 5p^6 5d^4 5f^0 5g^0 6s^1 6p^1 \\
 &5s^2 5p^6 5d^4 5f^0 5g^0 6s^1 6d^1 \\
 &5s^2 5p^6 5d^4 5f^0 5g^0 6s^1 7p^1 \\
 &5s^2 5p^6 5d^4 5f^0 5g^0 6s^1 7d^1
 \end{aligned}$$

Similar sets of rules exist to define allowed promotions from the second valence shell and from closed shells. A further set of rules determines which closed shells to allow promotions from. The set

$$\begin{aligned}
 n_{cl_{max}} &= 5 \\
 n_{cl_{min}} &= 5 \\
 l_{cl_{max}} &= 1 \\
 l_{cl_{min}} &= 0
 \end{aligned}$$

would allow promotions from the  $5s^2$  and  $5p^2$  closed shells. Finally, there are a few miscellaneous rules which it is useful to include:

closed shell	promote from inner shell closed shells (on/off)
fill $v1$ $n$ shell	add all nl configurations of outer valence shell n (on/off)
fill same parity only	if fill n add only opposite parity else add both parities (on/off)
extra 4f ground	shift one valence electron to unfilled 4f as an extra ground (on/off)
ground complex	include configs of same complex as the ground config (on/off)

For each unique ground configuration for every element up to Radon ( $z_0 = 86$ ) there is a different set of promotion rules. Due to differing ground configurations along iso-electronic sequences, particularly with near-neutral stages, this totals 180 different configurations. Three master sets of these rules have been predefined to allow calculations to run on different powers of computer, and are stored as ADF54 files within central ADAS.

### 3.1.3 Optimisation of Promotion Rules

Attempts to utilise the ADF54 data sets created manually to obtain useful atomic data encountered several early problems. Some of these were related to the stability of the codes, which failed to converge for one of the configurations for neutral or near neutral ions. Alternatively, the calculation produced would be unacceptably large and could not be performed on the available computing resources in a reasonable time. It became apparent that computational limitations would have to be taken into account while generating these rule sets. It also became apparent that there were many stages for which the promotion rules were producing very small calculations, which could easily accommodate greater numbers of configurations. Therefore optimisation of the rules used was clearly required.

One of the limiting factors on the configurations which can be included in the Cowan Code is the size of the computation, which rises almost linearly with the number of levels (*ls* and *ic* resolution) or the number of configurations (*ca* resolution). For most purposes, a calculation with approximately 1000 levels present will enable the calculation to run in a few hours and is usually large enough to encompass the major radiating transitions. There are however certain situations where larger calculations are necessary, in particular those ions with open 4f shells where even a minimalist calculation with only the ground and one excited configuration will have over 3000 levels.

The ideal structure/cross-section computation will capture as much of the radiated power as possible in a reasonably sized calculation. To enable custom limits to be placed on calculations, another set of routines has been designed for optimising the databases of rules used in ADAS808. Originally it was hoped that the predefined rule sets could be used to hold this data in its entirety, however it turns out that there are often differences in the optimum promotion rules between different ions even when they share the same ground configuration. The reason for this is twofold: the computation will automatically reject certain combinations of configurations which cause instability, which may differ between isoelectronic stages; and the strongest radiating transitions can change from element to element along an isoelectronic sequence.

The principle on which the optimisation code operates is fairly straightforward. Since the objective of the optimisation is to include the main radiating transitions,

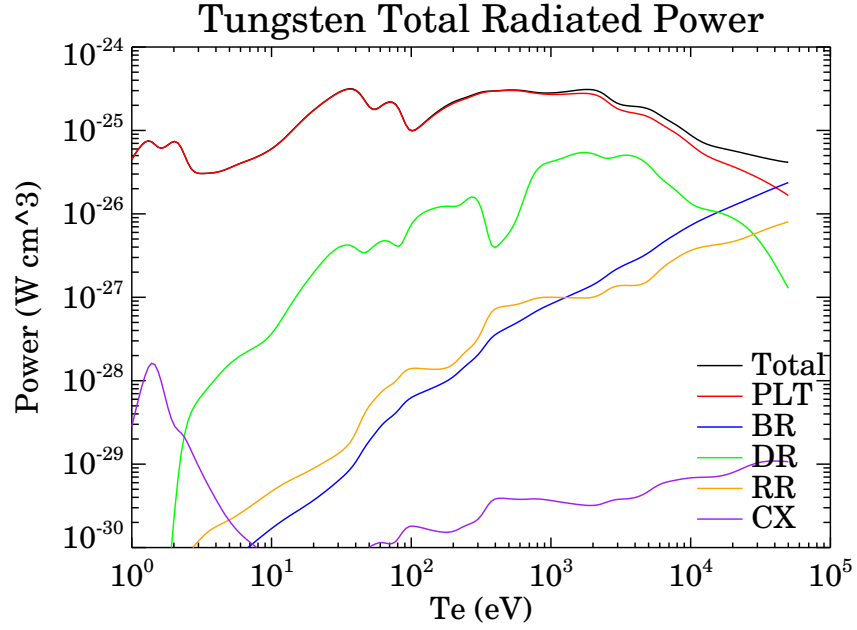


Figure 3.2: The total radiated power from tungsten as a function of  $T_e$ . The contribution of the different processes to the total power is shown - PLT is the total line power, DR is dielectronic recombination, BR is Bremsstrahlung, RR is radiative recombination and CX is thermal charge exchange.  $N_e = 1 \times 10^{13} \text{cm}^3$  and  $N_{H^0} = N_e(N_{H^0}/N_H)|_{eq}$  is assumed.

and the vast majority of the impurity emission is line radiation from collisional excitation/spontaneous emission (see figure 3.2), the figure of merit has been chosen to be the ratio  $\Delta \mathcal{P} \mathcal{L} T / \Delta n_{levels}$ , that is the increase in total line power vs increase in number of levels.

Given a starting configuration, a reference  $T_e$  and  $N_e$ , and the element and stage of interest, a very minimalistic set of promotion rules is used. The code progresses iteratively, trying each of 16 different rule changes (listed in table 3.1). For each rule which produces a new configuration set the Cowan Code is run in *ca* only mode (this mode is chosen due to its rapid run time, measured in seconds, while *ic* and *ls* runs can take days with complex configuration sets), and the post processed to obtain the  $\mathcal{P} \mathcal{L} T$ . Assuming this run is successful, the  $\Delta \mathcal{P} \mathcal{L} T / \Delta n_{levels}$  ratio is calculated and stored. After all 16 changes have been attempted, the change which produced the largest ratio is chosen as the reference

ID	Rule	Change	ID	Rule	Change
1.	$\delta n_{v1_{max}}$	+1	10.	$\delta n_{cl_{min}}$	-1
2.	$n_{v1_{min}}$	-1	11.	$\delta l_{cl_{max}}$	+1
3.	$\delta l_{v1_{max}}$	+1	12.	$\delta l_{cl_{min}}$	-1
4.	$\delta l_{v1_{min}}$	-1	13.	ground complex	1
5.	$\delta n_{v2_{max}}$	+1	14.	fill $v1$ $n$ shell	1
6.	$\delta n_{v2_{min}}$	-1		fill same parity only	1
7.	$\delta l_{v2_{max}}$	+1	15.	fill $v1$ $n$ shell	1
8.	$\delta l_{v2_{min}}$	-1		fill same parity only	0
9.	$\delta n_{cl_{max}}$	+1	16.	extra 4f ground	-1

Table 3.1: The changes to promotion rules attempted in each iteration of `adas8xx_opt_promotions_control`. An explanation of these rules is given in the text.

case, and the process is repeated, using this data set as the initial conditions for the next 16 changes. This continues until the number of levels reaches the target number chosen at the beginning. An example of the step by step nature of this process is shown in figure 3.3, while the structure of the code is shown in figure 3.4.

Once finished the code writes the data to an ADF54 file, allowing an ADAS808 run to be performed as before. Figure 3.1 shows the place of this code in the chain of fundamental data generation.

## 3.2 Sample Results

The technique outlined above provides several useful benefits. Purely practical benefits include: the removal of the requirement for detailed knowledge of atomic physics from the user in order to produce useful data; increased chance of a stable outcome, due to error checks on the Cowan code during the promotion rule selection; and the ability to manage the calculation size to suit the user. The additional physics benefit, beyond the stability issue, is that it becomes simple to estimate the “missing” radiated power due to the configurations which cannot be included in full  $ic$  and  $ls$  calculations.

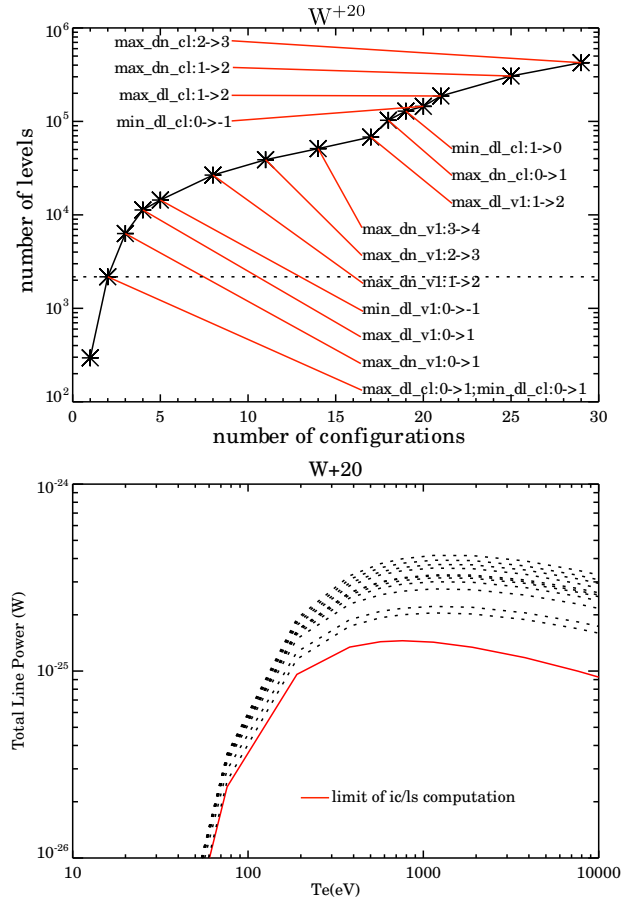


Figure 3.3: The step by step nature of an `adas8xx_opt_promotions_control` run, for  $W^{+20}$  (ground configuration:  $4d^{10} 4f^8$ ). *Top:* Starting from the ground configuration, promotion rules are amended gradually adding to the total number of configurations. The dotted line indicates where a reasonably large *ic* or *ls* coupled calculation would have stopped. *Bottom:* The gradual increase in  $\mathcal{P}LT$  with each step in the above calculation. In this case the total radiated power is underestimated by a factor of between 2 and 3 when compared with the limit of the *ic/ls* calculations.

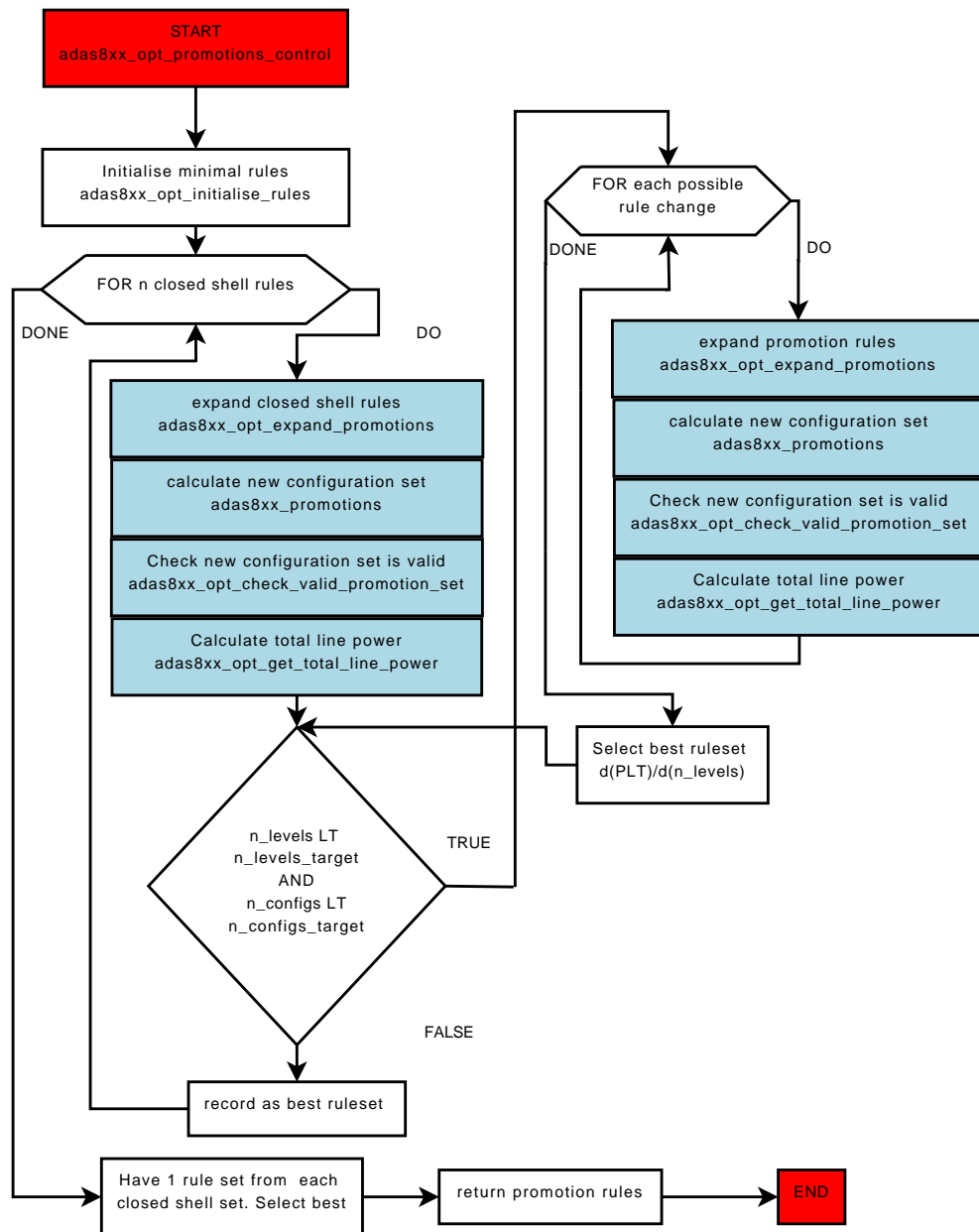


Figure 3.4: The structure of the promotion rule optimisation code. The promotion rules applied during each iteration of *adas8xx\_opt\_expand\_promotions* are listed in table 3.1. In the first iteration, a electric dipole allowed transition is forced to occur to initiate the process.

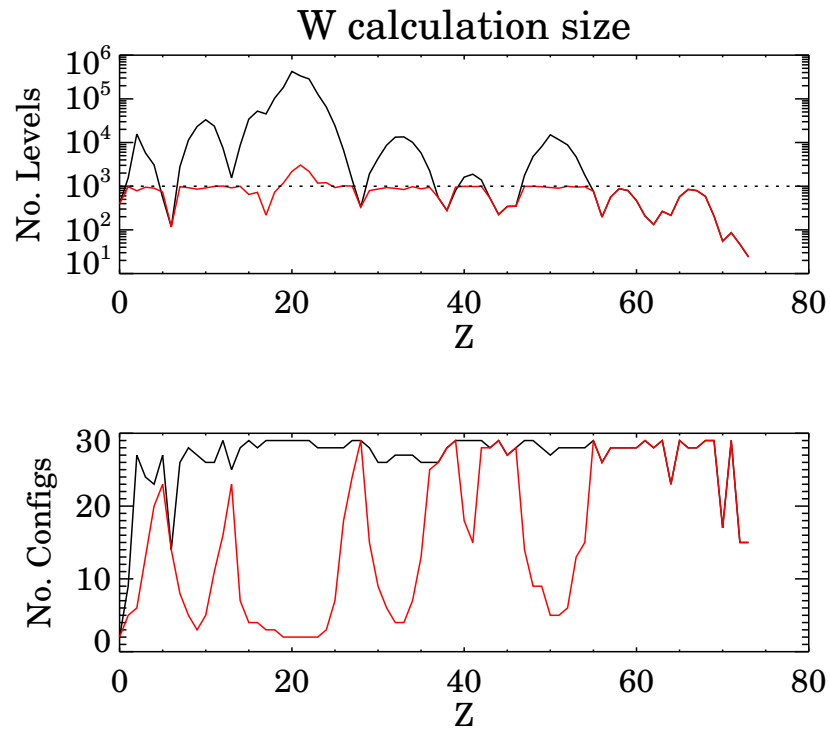


Figure 3.5: The number of configuration and levels present in the data sets produced by the normal (red) and large (black) sized runs of ADAS808. The dashed line in the upper graph indicates the target calculation size for the normal sized run, 1000 levels.

To this end, for each element calculations have been performed in two limits. The first set was limited to 1000 levels, or 30 configurations, whichever limit was encountered first. The second set was limited only to the 30 configurations, with an infinite number of levels allowed. The relative sizes of these calculations are shown in figure 3.5. Tungsten will be focused on as an example for the different results, but calculations have also been performed successfully using these methods for all stages of W, Xe, Sn, In, Kr, Fe, Ar, Al and C.

### 3.2.1 Ionisation Balance

One of the primary uses of this data, in transport modelling for experimental analysis, requires knowledge of the collisional radiative (CR) coefficients (section 2.3.2). In particular

in the regime here, the ionisation ( $S_{CD}$ ) and recombination ( $\alpha_{CD}$ ) coefficients are required. These will therefore be discussed before continuing to the missing power calculations.

The method which will be used here to determine these coefficients is that employed by ADAS codes 407/408, which apply simple parametric forms for these values. These are described in section 2.3.2: it is sufficient here to recall that there are two main categories, called case A and case B. There are known problems with the case B calculation of dielectronic recombination rates, and until recently there were also problems with the radiative recombination power calculations<sup>2</sup>. It is possible to use the case B calculation for all but the dielectronic recombination rate coefficient.

Due to the issues with the case B method it has been customary to use the case A approximations for most ionisation balance calculations. However, as is shown in figure 3.6, the case B coefficients do have a significant effect on the ionisation balance and therefore use should be made of them where possible. Therefore in this work the case B methods will be used for all processes except dielectronic recombination, which will use case A.

### 3.2.2 Line Radiated Power from Individual Stages

The emission of light from individual stages is of interest for several reasons. Firstly, line emission from individual stages can be used for the various spectroscopic measures outlined at the start of chapter 2. Secondly, it forms a significant part of the total power which is radiated from the plasma, and therefore an accurate calculation is required to ensure that the total radiated power is computed correctly.

Figure 3.2 shows the power radiated by tungsten, assuming a steady state ionisation balance. It also shows the constituent parts that form this radiation, consisting of Bremsstrahlung, radiative recombination, dielectronic recombination, and electron impact excitation line emission. As can be seen, line radiation dominates the emitted power, and therefore it is this form of radiation which requires the most attention.

#### Total Line Radiated Power

Comparing the  $\mathcal{PCT}$  calculations for different coupling schemes can be informative. Such a comparison is shown in figure 3.7 for two ionisation stages of tungsten. It is actually found

---

<sup>2</sup>The radiative recombination power issues have been resolved as part of this work.

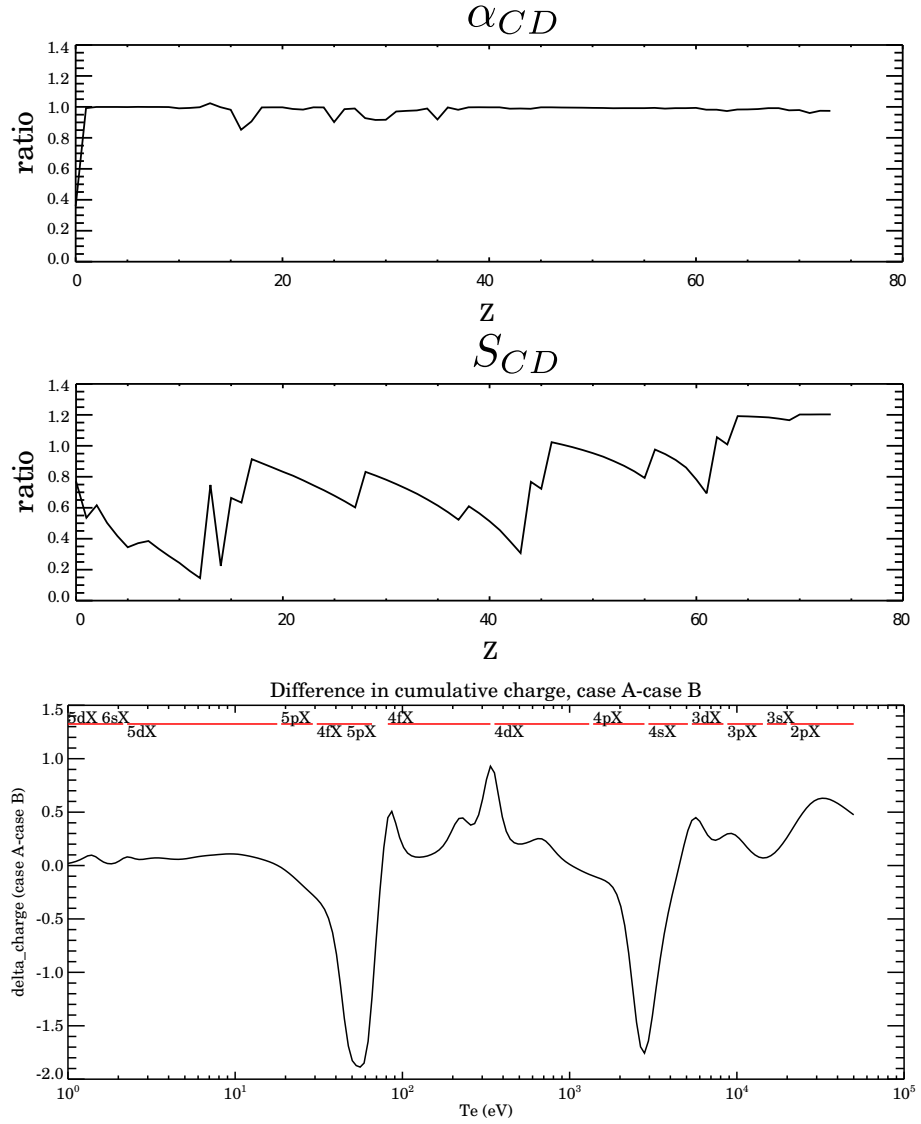


Figure 3.6: *Top 2 panels:* The ratio (case A/case B) of the recombination and ionisation rate coefficients  $\alpha_{CD}$  and  $S_{CD}$  for tungsten.  $T_e$  = ionisation potential of each ion. Note that for the  $\alpha_{CD}$  case B only radiative recombination is calculated using the case B method. *Bottom:* The difference between the total charge  $z_1, = \sum_z [N_z \times (z + 1)]$  for case A and case B steady state ionisation balances for tungsten in a plasma with  $N_e = 1 \times 10^{13}$ . The two methods can produce a shift in ionisation balance equivalent to ionising every stage twice more in the case B approximation, particularly near  $n$  shell boundaries.

that the  $\mathcal{P}\mathcal{L}\mathcal{T}$  for different coupling schemes can vary quite widely, particularly in stages with open d and f shells (about 14 stages of tungsten are affected). These discrepancies always follow the pattern of  $ic$  being the most heavily reduced, then  $ls$ , then  $ca$ . These differences are attributed to the energy of the ground state in each model being different: the energy of the ground configuration of the  $ca$  model is approximately the weighted mean of the levels of the  $ic$  model for the same configuration. This leads to systematic differences in the radiated power for systems where there is a large distribution of energies in the ground configuration. As the  $ic$  calculation is the most accurate for heavy species, it is assumed to be the true radiated power for the included configurations.

The ability to run the configuration averaged calculations for large numbers of configurations with no real constraints on the number of “levels” included (levels being irrelevant in the  $ca$  picture) provides a method for estimating the missing power due to omitted configurations. For most stages this is a relatively small difference, as the contribution to the radiation from each additional configuration reduces as  $n$  increases. However, for some stages, such as those with the open 4f shells, the  $ic$  calculations are limited to two or three configurations. The  $ca$  calculation can then be run for a much larger configuration set, and the difference between the radiated power from the large and normal  $ca$  and runs can be added to the  $ic$  results for the smaller calculation to obtain a better estimate of the total radiated power from all configurations.

An example of this is shown in figure 3.8, where the calculated  $\mathcal{P}\mathcal{L}\mathcal{T}$ s from various different coupling schemes are compared. As can be seen, particularly in the  $T_e \approx 200\text{eV}$  region, there is a significant reduction in the line emission calculated using the normal sized configuration sets. This temperature range also corresponds to the dominant ionisation stages having open 4f shells, which restrict the calculations to only 2 or 3 configurations. The extra power which can be obtained from the large  $ca$  calculations is shown for various elements in figure 3.9: the “power gap” for the open 4f shell is considerable, and explains the drop.

The effect of compensating for this gap is shown by the  $ca\_large$  line in figure 3.8. It can be seen that the sharp drop in line radiated power at 200eV disappears. For comparison with the data from this work, earlier work by Whiteford[61] is also shown in the figure, labelled ADW. The same features, and the same dip due to reduced configuration selection,

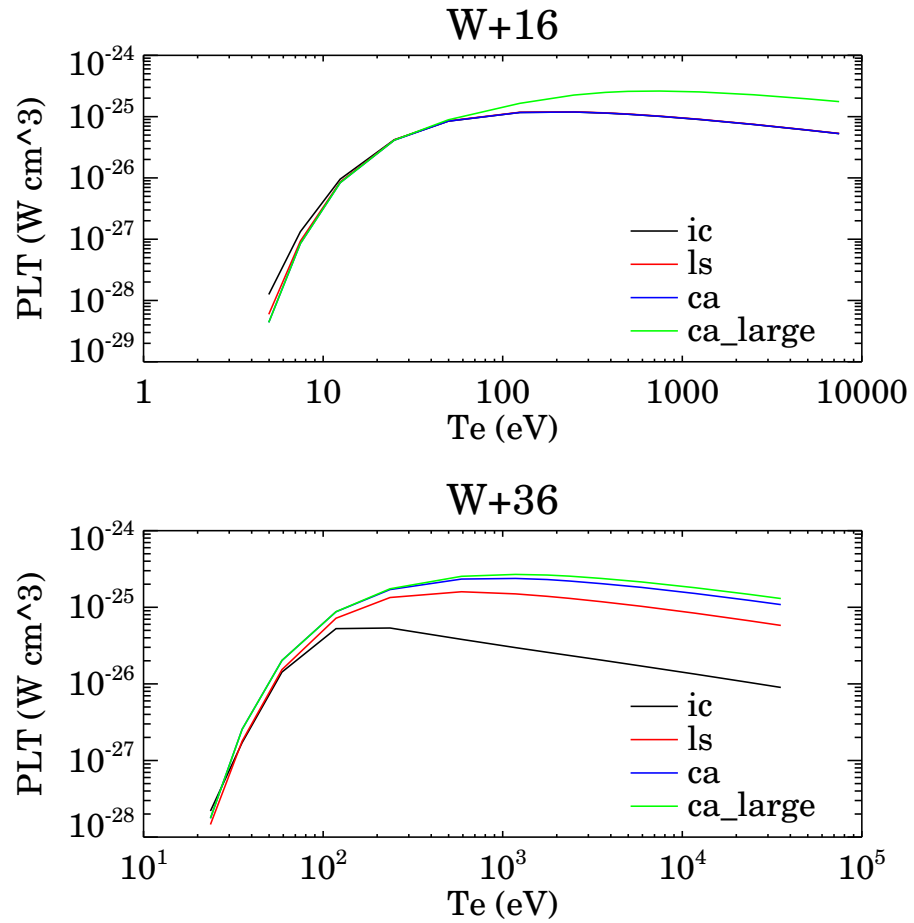


Figure 3.7: The total radiated line power calculations for different coupling schemes for two different ions, taken from the results of an ADAS 808 run. For most stages there is good agreement between different coupling schemes, as shown in the upper figure (the *ic*, *ls* and *ca* lines lie on top of each other at high  $T_e$ ). However, for those stages with open d and f shells the *ic* a difference opens up, as the configuration averaged approach overestimates the radiated power due to the spread of term energies within the ground configuration. The difference between the two *ca* calculations can still be used for the radiated power top up.

is found in the Whiteford data, although there is a shift in the temperatures at which they are observed associated with differences in the ionisation balances used.

### Line Emission

Another use of this technique, as well as estimating the omitted power, is the ability to estimate the wavelength of the emission from missing transitions. An example of this is shown in figure 3.10, which compares the feature photon emissivity coefficient for different *ca* and *ic* coupling with that for the larger *ca* calculation. The *ic* calculation reveals the structure of the transition array at 64Å, while the large *ca* calculations reveal the wavelengths of the many other transitions present.

While the *ca* approximation cannot be used for line spectroscopy, it can be used to gauge the approximate spectral region in which spectral features are likely to appear. Such features include the transition arrays of heavy elements which contain a large number of transitions, making accurate *ic* modelling difficult. As the nuclear charge increases along an iso-electronic sequence, the transition arrays move to lower energies, as is shown for two of such arrays in figure 3.11. It should be noted, however, that a significant shift is observed in the wavelength for these lines when compared to predicted spectra. Compare figure 4.8 with figure 3.11: the peak at  $\approx 135\text{\AA}$  in the former is from the two transition arrays of Sn shown in the latter, however they have shifted 30Å when changing from *ic* to *ca* coupling. This is due largely to the increased ground configuration energy as explained above. This leads to a considerable shift in energy between the two approximations, which leads to the spectral shifts observed.

## 3.3 Superstages

### 3.3.1 The Need for Superstaging

Plasma modelling with light elements has routinely been performed using methods which will be described and utilised in section 4.5. The assumptions of toroidal symmetry and constant plasma conditions along a magnetic flux surface which this code makes are, however, only valid in the core of the plasma. At the plasma edge, and in particular in the scrape off layer, the field lines are no longer closed and phenomena such as plasma-surface

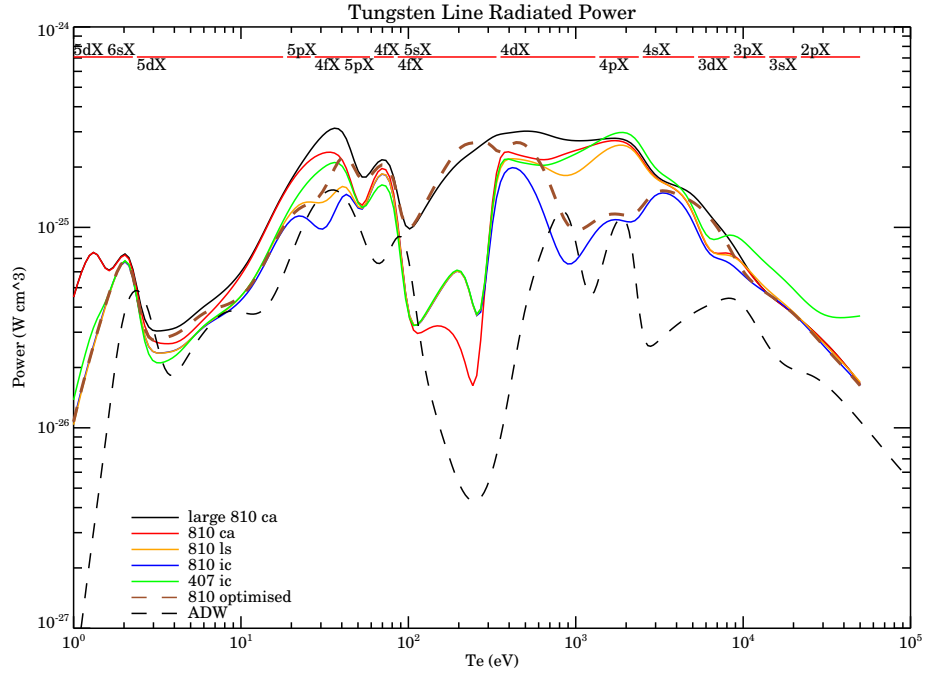


Figure 3.8: A comparison of total line power ( $\mathcal{P}_{LT}$ ) calculations for different coupling schemes and calculation methods. The parametric forms of ADAS 407 are compared to the results from an ADAS 808/801/810 run. The results of [61] are shown for comparison, labelled ADW. An equilibrium ionisation balance is assumed with  $N_e = 10^{13}\text{cm}^{-3}$ . The “large” run denotes the ADAS808 run with unlimited numbers of levels included, and run only in the *ca* coupling scheme. The “optimised” data set is the 810\_ic+ $\Delta$ 810\_ca, to account for missing power. The bar at the top indicates the open shells in the ground configuration of the dominant stage at each temperature.

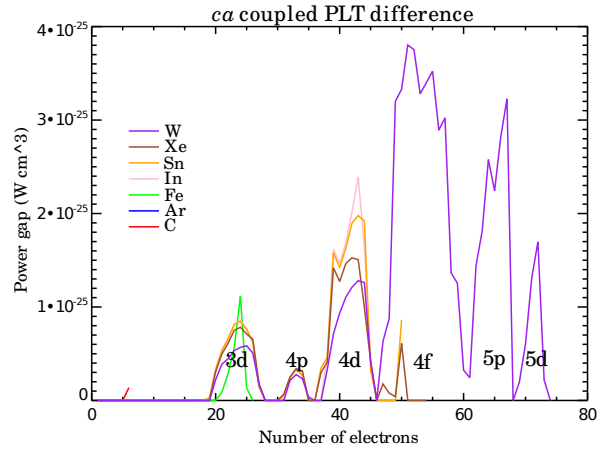


Figure 3.9: The difference in line radiated power in the *ca* coupling scheme for the *ca\_large* and *ca* calculations ( $\mathcal{PLT}_{ca\_large} - \mathcal{PLT}_{ca}$ ). The open shells at each peak are noted on the graph.  $T_e =$  ionisation potential for each ion,  $N_e = 1 \times 10^{13} \text{cm}^{-3}$ .

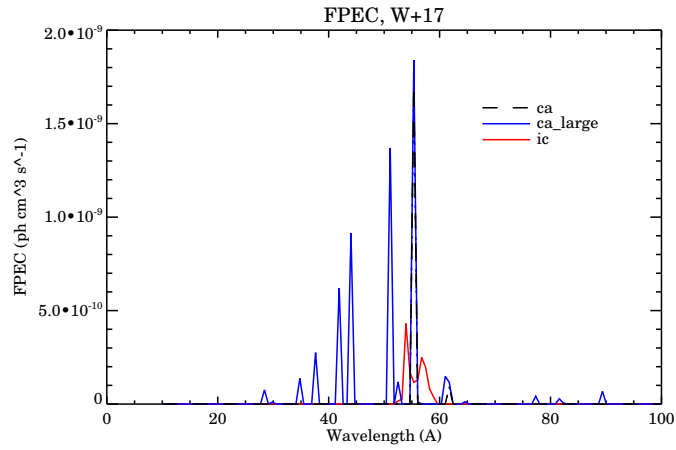


Figure 3.10: The feature photon emissivity coefficients obtained from the different coupling schemes and calculation sizes for  $\text{W}^{+17}$ .  $T_e = 419 \text{eV}$  and  $N_e = 1 \times 10^{13} \text{cm}^{-3}$

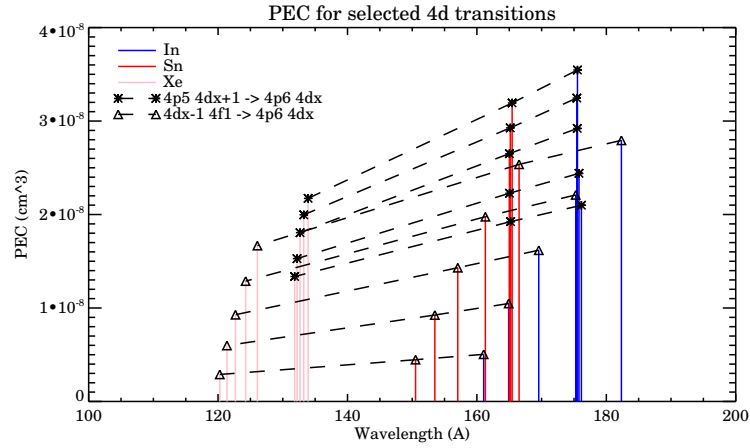


Figure 3.11: The  $\mathcal{PEC}$  for the  $4p^5 4d^{x+1} \rightarrow 4p^6 4d^x$  and the  $4p^6 4d^{x-1} \rightarrow 4p^6 4d^x$  transition arrays. The movement of the features to lower wavelength along an isoelectronic sequence (connected by dashed lines) can be seen. The Rb-like (37 electrons) to Nb-like (41 electrons) stages are shown.

interactions and interaction with significant numbers of cold neutral atoms lead to these assumptions breaking down.

To model these regions with more success, 2 dimensional codes such as B2[62], EDGE2D[63] and others have been developed. These codes model the plasma as a series of fluids, with each different ionisation stage of each ion being a separate fluid, described by macroscopic variables such as the density,  $N(x, t)$ , velocity,  $N(v, t)$ , and pressure,  $p(x, t)$ , as opposed to a kinetic model where individual particle values are tracked, which would be computationally much more intensive. The fluid model is acceptable in the edge region due to the high plasma collisionality (that is the relatively low temperatures make the mean free path for the ions considerably less than the vessel size). However it is limited in the number of different fluids that can be included in the model. Currently, EDGE2D routinely handles up to 12 ion fluids - 2 for hydrogen, 3 for helium and 7 for carbon. Inclusion of all 75 stages of tungsten is not possible due to a combination of calculation size limits and stability issues - with a large number of cells where the population for many stages will be 0 or not significantly greater than this, results can easily become skewed due to a division by a very small number.

It is therefore necessary to reduce the number of different fluids which need to be modelled in the simulation to increase stability. This provides the motivation for superstaging.

### 3.3.2 The Superstage Model

To reduce the number of species present in a plasma simulation, the superstage model groups together many different stages to form a superstage. Within each superstage, it is assumed that the fractional abundances of the constituents of the superstage are in coronal equilibrium. As an example, consider carbon - though it is probably not worth superstaging an element with so few stages, it is easier to explain the concept with fewer stages present.

There are 7 stages of carbon, from  $C^{+0}$  to  $C^{+6}$ , which for this work have been divided into a total 12 metastable states (see figure 3.12). The *metastable resolved root partition layer*, which is always labelled ‘00’, can be defined as:

```
//#00/p00/ 00/p01/ 01/p02/ 02/p03/ 03/p04/ 04/p05/ 05/p06/ 06/
      p07/ 07/p08/ 08/p09/ 09/p10/ 10/p11/ 11/p12/ 12/p13/ 13/
```

where the ‘p’ labels the superstage and the numbers following list the superstages of the parent partition layer. Since this is the root partition, the parent is the individual metastables. If these were to be grouped into superstages, with each corresponding to a single ionisation stage of the ion, the child ionisation state would be labelled as:

```
//#01//p00/ 00 01 02 03/p01/ 04 05/p02/ 06 07/
      p03/ 08/p04/ 09 10/p05/ 11/p06/ 12/
```

So far, although the terminology of superstaging has been used, this has simply been grouping coefficients together. In theory, the results from this should be equivalent to comparing metastable resolved and unresolved data. But the notation for the process is maintained throughout, so if the data is now superstaged with, for example, the  $C^{+1}$  to  $C^{+3}$  are grouped together, and the  $C^{+4}$  and  $C^{+5}$ , this is written:

```
//#02/p00/ 00/p01/ 01 02 03/p02/ 04 05/p06/ 06/
```

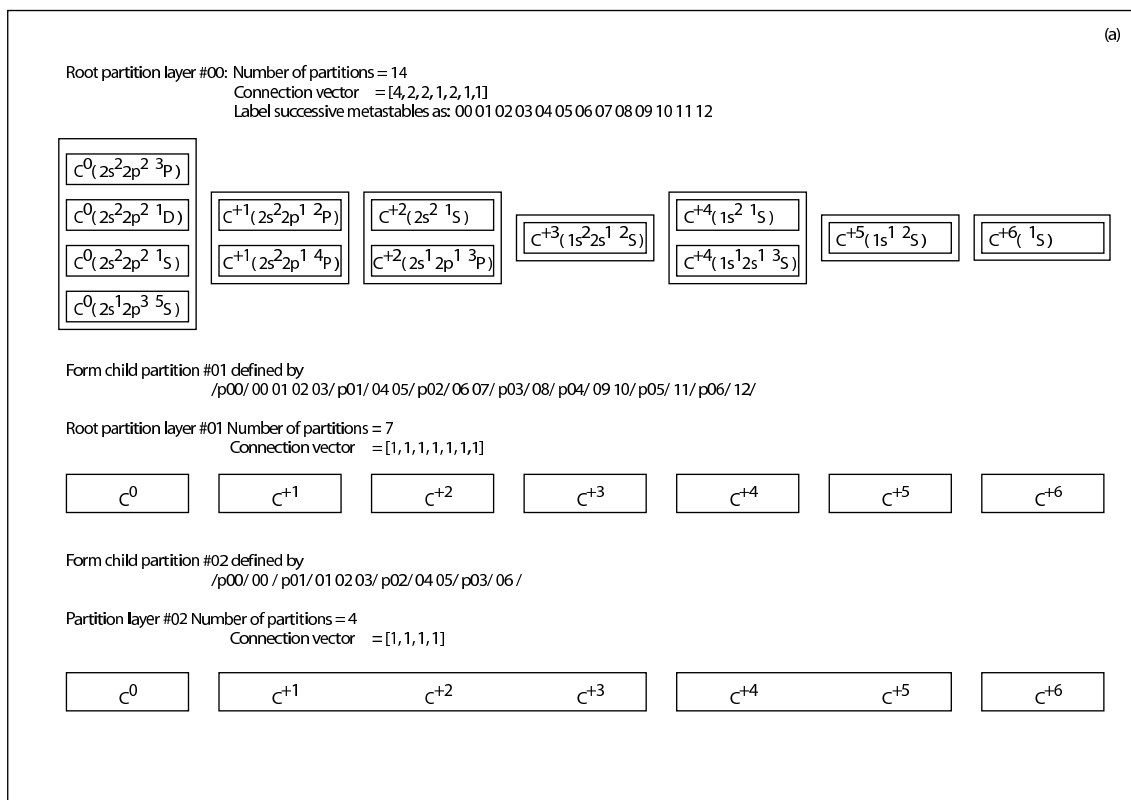


Figure 3.12: The superstaging method, applied to carbon. If starting from the metastable resolved case, the root partition is #00 (top row). In this example, bundling has been applied to move from the resolved to the unresolved child partition (top row to middle row). Similarly, if starting from the unresolved case, the root partition is labelled #01 and the child partition is #02, as shown here when superstaging carbon into 4 stages (middle row to bottom row).

This process can be carried on with superstages being further combined forming a third and fourth partition layer should the need arise, although the circumstances in which such a process would be beneficial are not immediately clear.

In the cases used for superstaging in this work, the heavy species baseline data is not metastable resolved, and the root partition is the set of ionisation stages, not metastables.

//#01/p00/ 00/p01/ 01/p02/ 02/p03/ 03/p04/ 04/p05/ 05/p06/ 06/

Take as an example the case of superstaging from this unresolved baseline data partition, #01, and assembling a superstaged partition, #02. The population of superstage  $i$  in partition level  $k$  is denoted  $N^{[\#k](i)}$ . The time dependence of the populations of the superstages in the #01 layer is given by:

$$\begin{aligned} \frac{dN^{[\#01](i)}}{dt} &= N_e S_{CD}^{[\#01](i-1 \rightarrow i)} N^{[\#01](i-1)} \\ &\quad - N_e \left( S_{CD}^{[\#01](i \rightarrow i+1)} + \alpha_{CD}^{[\#01](i-1 \rightarrow i)} \right) N^{[\#01](i)} \\ &\quad + N_e \alpha_{CD}^{[\#01](i+1 \rightarrow i)} N^{[\#01](i+1)} \end{aligned} \quad (3.1)$$

Where the first and last terms represent ionisation and recombination into the superstage, and the middle term represents ionisation and recombination out of the superstage. The coefficients of this #01 partition are the collisional-radiative coefficients  $S_{CD}$  and  $\alpha_{CD}$  introduced in section 2.3.2, because the superstages of this partition are simply the individual ion stages of the element.

Consider a child partition layer, layer #02. If superstage  $j$  in this partition consists of the  $i_0$  to  $i_1$  superstages of the #01 partition, and quasi-static equilibrium (i.e.  $dN/dt = 0$ ) is enforced for each of the superstages in the #01 partition:

$$\begin{aligned} N^{[\#01](i_0)}|_{eq} &= \left( \alpha_{CD}^{[\#01](i_0+1 \rightarrow i_0)} / S_{CD}^{[\#01](i_0 \rightarrow i_0+1)} \right) N^{[\#01](i_0+1)}|_{eq} \\ N^{[\#01](i_0+1)}|_{eq} &= \left( \alpha_{CD}^{[\#01](i_0+2 \rightarrow i_0+1)} / S_{CD}^{[\#01](i_0+1 \rightarrow i_0+2)} \right) N^{[\#01](i_0+2)}|_{eq} \\ &\vdots \\ N^{[\#01](i_1-1)}|_{eq} &= \left( \alpha_{CD}^{[\#01](i_1 \rightarrow i_1-1)} / S_{CD}^{[\#01](i_1-1 \rightarrow i_1)} \right) N^{[\#01](i_1)}|_{eq} \end{aligned} \quad (3.2)$$

and the populations are assumed to be normalised such that

$$N^{[\#02](j)} = \sum_{i=i_0}^{i_1} N^{[\#01](i)}|_{eq} \quad (3.3)$$

then the effective ionisation and recombination rates for the partition  $k$  superstage  $j$  can be defined as:

$$\begin{aligned}\alpha_{CD}^{[\#02](j \rightarrow j-1)} &= \alpha_{CD}^{[\#01](i_0 \rightarrow i_0-1)} \left( N^{[\#01](i_0)} / N^{[\#02](j)} \right) |_{eq} \\ S_{CD}^{[\#01](j \rightarrow j-1)} &= S_{CD}^{[\#01](i_1 \rightarrow i_1+1)} \left( N^{[\#01](i_1)} / N^{[\#02](j)} \right) |_{eq}\end{aligned}\quad (3.4)$$

which is to say that the superstage ionisation and recombination rates are determined by the population and rates for the stages at the upper and lower edges of the superstages respectively. For conciseness define the fractional population  $F_{i,j}^{[\#k]}$  as the steady state ionisation balance of the stage within the superstages. In the general case this is:

$$F_{i,j}^{[\#k]} = \left( N^{[\#k](i)} / N^{[\#k+1](j)} \right) |_{eq} \quad (3.5)$$

Other collisional-radiative coefficients, such as the total radiated power, are dealt with in a similar fashion to the  $\alpha_{CD}$  and  $S_{CD}$ s, except that the total power is dependent on the fractions of all the stages present in an superstage:

$$P_{tot}^{[\#02](j)} = \sum_{i=i_0}^{i_1} P_{tot}^{[\#01](i)} F_{i,j}^{[\#00]} \quad (3.6)$$

Looking at a more general case than just the #01 partition, there may be multiple partition members in this case. For a general parent to child condensation, with results applicable to any  $\#k \rightarrow \#k+1$  condensation, it is more useful to work with matrices than equations. The matrix  $\mathbf{F}$  represents the fractional abundance of each of the superstages in the parent partition, re-normalised so that the population of each child partition superstage has a total fractional abundance of 1.

$$\mathbf{F} = \begin{bmatrix} [\mathcal{F}_{0,0}^{[\#k]}] & 0 & \cdot & 0 \\ 0 & [\mathcal{F}_{1,1}^{[\#k]}] & \cdot & 0 \\ \cdot & \cdot & \cdot & \cdot \\ 0 & 0 & \cdot & [\mathcal{F}_{N_c, N_c}^{[\#k]}] \end{bmatrix} \quad (3.7)$$

Define a form of the identity matrix which identifies those superstates which are present

in each partition:

$$\mathbf{I} = \begin{bmatrix} \mathcal{I}_{ij}^{[\#k]} & 0 & \cdot & 0 \\ 0 & \mathcal{I}_{ij}^{[\#k]} & \cdot & 0 \\ \cdot & \cdot & \cdot & \cdot \\ 0 & 0 & \cdot & \mathcal{I}_{ij}^{[\#k]} \end{bmatrix} \quad (3.8)$$

with  $\mathcal{I}_{ij}^{[\#k]}$  a vector which is 1 for stages within the superstage and zero for those which fall outside it.

The collisional radiative matrix  $\mathbf{C}$  can then be formed from the sub-matrices of the parent superstage:

$$\mathbf{C} = \begin{bmatrix} \mathcal{C}^{[\#k](0 \rightarrow 0)} & N_e \alpha^{[\#k](1 \rightarrow 0)} & \cdot & \cdot \\ N_e \mathcal{S}^{[\#k](0 \rightarrow 1)} & \mathcal{C}^{[\#k](1 \rightarrow 1)} & \cdot & \cdot \\ \cdot & N_e \mathcal{S}^{([\#k]1 \rightarrow 2)} & \cdot & \cdot \\ \cdot & \cdot & \cdot & \cdot \end{bmatrix} \quad (3.9)$$

The collisional radiative matrix for the child partition, which shall be called  $\mathbf{D}$ , is then given by  $\mathbf{D} = \mathbf{I}^T \mathbf{C} \mathbf{F}$ . In words, that is the collisional radiative matrix for a superstage in the child partition is determined by the fractional abundance of each of the parent superstages in the partition, multiplied by the CR matrix elements.

$$\mathbf{D} = \begin{bmatrix} \mathcal{C}^{[\#01](0 \rightarrow 0)} & N_e \alpha^{[\#01](1 \rightarrow 0)} & \cdot & \cdot \\ N_e \mathcal{S}^{[\#00](0 \rightarrow 1)} & \mathcal{C}^{[\#00](1 \rightarrow 1)} & \cdot & \cdot \\ \cdot & N_e \mathcal{S}^{[\#00]1 \rightarrow 2)} & \cdot & \cdot \\ \cdot & \cdot & \cdot & \cdot \end{bmatrix} \quad (3.10)$$

from which the CR coefficients for a given element may be extracted. This formalism applies to a completely general parent to child condensation, as opposed to just the #01 to #02 condensation dealt with earlier. For the remainder of this work only the #01 to #02 will be looked at, but it is notable that the technique works for any partition level.

The thermal charge exchange coefficient has not been addressed here, but a similar system to that used above can be used to obtain a  $\mathbf{CX}$  matrix instead of  $\mathbf{C}$  by replacing  $\mathcal{R}$  with the thermal charge exchange sub-matrix  $\mathcal{R}^{CX}$ .

### 3.3.3 Bundling Schemes - The Natural Partition

Once the possibility of superstaging ionisation states (or *bundling*) stages together becomes possible, the choice of which stages to bundle together and which to leave isolated arises.

Spectroscopically observable line emission from ions in the plasma mostly originates from stages with closed shell electron configurations and those adjacent to it. Ions with half full shells tend to produce many overlapping lines of lower intensity - see the 135Å feature of Sn observed in chapter 4 as an example. An optimal bundling scheme for spectroscopic observation would isolate the stages likely to produce strong line emission, and group together those where the line emission become indistinct. Such a bundling scheme is called the *natural partition*.

By looking at the fractional variation of the ionisation potential  $I$  of successive ions,  $2(I_{z+1} - I_z) / (I_{z+1} + I_z)$ , a bundling scheme can be selected, as shown in figure 3.13 for tungsten. Where this ratio is small, ionisation stages are grouped. Where it is larger than the running mean of seven adjacent stages plus a deviation  $\sigma$ , the ions are kept as individual stages.

This procedure maintains the isolation of stages with one or two electrons, which are the stages for which advanced methods such as R-matrix can be used, therefore this system allows high quality data for these stages to be substituted where it exists, while superstaged baseline data can be used elsewhere.

For application to spectroscopy using the superstaged ions, the superstaged envelope feature photon emissivity function,  $\mathcal{FGTN}$  are useful. In a wavelength range  $[0, 1]$ :

$$\mathcal{FP}\mathcal{E}\mathcal{C}^{[\#02][0,1](j)} = \sum_{i=i_0}^{i_1} \mathcal{FP}\mathcal{E}\mathcal{C}^{[\#01][0,1](i)} \left( N^{[\#01](i)} / N^{[\#02](j)} \right) |_{eq} \quad (3.11)$$

For the #01 partition of baseline data, which is not metastable resolved, the partition members are the ionisation stages and the  $\mathcal{FP}\mathcal{E}\mathcal{C}$  are in fact the  $\mathcal{FP}\mathcal{E}\mathcal{C}$  coefficients for each stage:

$$\mathcal{FP}\mathcal{E}\mathcal{C}^{[\#01][0,1](z)} = \mathcal{FP}\mathcal{E}\mathcal{C}^{[0,1](z)} \quad (3.12)$$

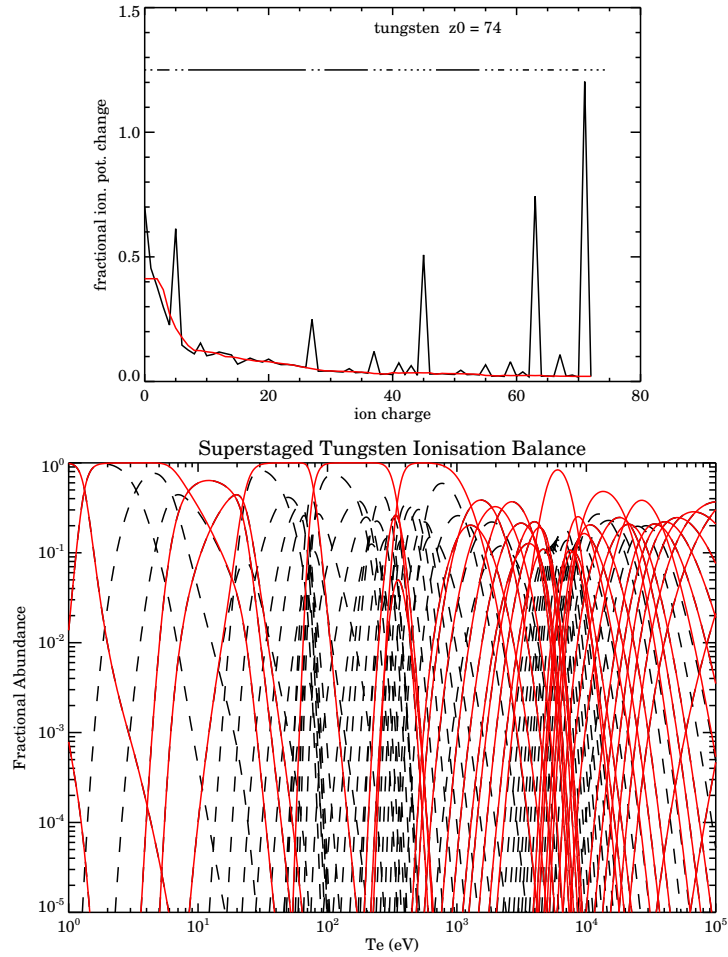


Figure 3.13: *Top*: The fractional change in ionisation potential for tungsten. The red line shows the running mean of 2 adjacent stages. Where the change falls above a specified deviation  $\sigma$  from the running mean, the stage is isolated as an individual stage. *Bottom*: The single ion (black) and superstaged (red) fractional abundances for 35-stage naturally partitioned tungsten.

This allows features from superstages with many ions in one bundle to be tracked in the superstage model.

### 3.3.4 Superstaging in Modelling Codes.

Generating a superstaged partition that can be used in fluid codes requires more details to be observed. The treatment of the neutral atom by these codes is significantly different from the other ions due to the fact that they are not affected by the magnetic field in the plasma. Therefore the neutral atom must be kept as a separate stage. Similarly the singly ionised state should be kept separate as well, as this is connected to the neutrals. Due to a current issue with the estimation of the total line radiated power by the superstaging codes, the fully stripped ion must also be kept as a separate ion to avoid underestimating the radiated power. This will hopefully be resolved in the near future. Finally, stages which are not likely to be present in the plasma can be safely bundled into a single large superstage - e.g. in JET plasmas it is possible to safely bundle  $W^{+47}$  to  $W^{+73}$  together as these stages will not exist in significant quantities in the plasma.

Modelling codes make use of the ion charge  $Z$ , the ion charge squared  $Z^2$ , and the ionisation potential  $I_p$  of the ions in the plasma. For superstaged data, these are no longer constants for an ionisation stage, but have become a function of the local plasma conditions, which affect the ionisation balance within the superstage. Therefore collisional radiative coefficients are defined for the three quantities, labelled  $Z_{CD}$ ,  $Y_{CD}$  and  $E_{CD}$  respectively.

Calculation of the  $Z_{CD}$  and  $Y_{CD}$  terms is simple - the charge is given by the fractional abundance of each ion within the superstage:

$$\begin{aligned} z_{cr}^{[\#02](j)} &= \sum_{i \in p_j^{[\#02]}} z_{cr}^{[\#01](i)} F_{i,j}^{[\#01]} \\ (z^2)_{cr}^{[\#02](j)} &= \sum_{i \in p_j^{[\#02]}} (z^2)_{cr}^{[\#01](i)} F_{i,j}^{[\#01]} \end{aligned} \quad (3.13)$$

This is shown for a typical superstage of tungsten in figure 3.14.

The ionisation potential,  $E_{CD}$ , is not so straightforward. It is implicitly assumed in the non-superstaged picture that the neutral atom has zero ‘‘birth energy’’, which can be considered the ionisation potential of the -1th stage: the birth energy of the neutral atom

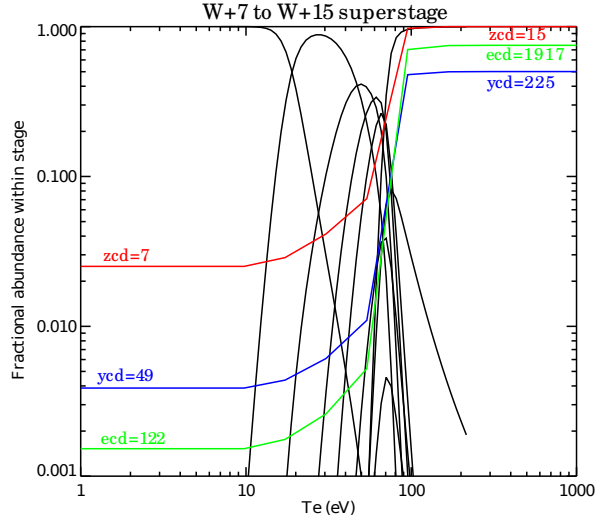


Figure 3.14: The fractional abundance of the components of the  $W^{+7}$  to  $W^{+15}$  superstage. Overlaid are the  $Z_{CD}$ ,  $Y_{CD}$  and  $E_{CD}$  coefficients, on a linear scale.

provides a reference point for the ionisation potentials of all the other stages. But if a superstage incorporates the neutral and at least one other ion this is no longer necessarily true, therefore the  $E_{CD}$  requires an additional set of data (known as a block) for the first superstage. In the case of the root #01 partition, this block is zero at all points, since the birth energy is zero in the unresolved case. However, for both resolved data and superstages incorporating the neutral, the  $E_{CD}$  incorporates excitation energies from within the superstage as well as ionisation energies to the next stage. The augmented excitation/ionisation energy matrix can be written:

$$\mathbf{E} = \begin{bmatrix} 0 & \mathcal{E}^{[\#00]}(-1 \rightarrow 0) & \cdot & \cdot & \cdot \\ \cdot & \mathcal{E}^{[\#00]}(0 \rightarrow 0) & \mathcal{E}^{[\#00]}(0 \rightarrow 1) & \cdot & \cdot \\ \cdot & \cdot & \mathcal{E}^{[\#00]}(1 \rightarrow 1) & \mathcal{E}^{[\#00]}(1 \rightarrow 2) & \cdot \\ \cdot & \cdot & \cdot & \mathcal{E}^{[\#00]}(2 \rightarrow 2) & \cdot \\ \cdot & \cdot & \cdot & \cdot & \cdot \end{bmatrix} \quad (3.14)$$

where the  $\mathcal{E}^{[\#00]}(1 \rightarrow 1)$  terms represent the sub-matrix of excitation energies within super-

stage 1, while the  $\mathcal{E}^{[\#00](0 \rightarrow 1)}$  represent the ionisations from superstage 0 to superstage 1 (or, in the case of the -1 to 0 “ionisation”, the formation energies of the members of the superstage).

The values of the  $\mathcal{E}$  come from the ADAS adf00 files, which tabulate the ionisation potentials of the different ionisation states. For some elements, these extend to metastable resolved data. Once the  $\mathcal{E}$  have been obtained, an augmented fractional abundance matrix  $\mathbf{G}$  is formed:

$$\mathbf{G} = \begin{bmatrix} 1 & 0 \\ 0 & \mathbf{F} \end{bmatrix} \quad (3.15)$$

where  $\mathbf{F}$  is as defined in equation 3.7. The child matrix is then  $\mathbf{G}^T \mathbf{E} \mathbf{G}$ , from which the child  $E_{CDS}$  can be obtained as for the other coefficients.

### 3.3.5 Sample Application - 1D and 2D Plasma Modelling

The superstaged tungsten information prepared as described in the above have been used with the JAMS code suite at JET. This incorporates both the SANCO 1.5-D model in the core and the 2-D EDGE2D at the edge. As well as the data preparation, it was required to modify these codes to deal with the non-integer and changing  $Z$ ,  $Z^2$  and  $I_p$ . In the 1D case, several different superstaging schemes were tried with nickel and tungsten for comparison with standard stage to stage data. Some characteristics of the JET plasma used are shown in figure 3.15.

There is no obvious single figure of merit to show that the superstaged data works well, however as a general guideline in the 1D case agreement with the non-superstaged data would be hoped for. One proposed measure of the method for a given plasma is the departure from the coronal equilibrium ionisation balance. This varies as  $\propto \sum (I_{z+1} S_z N_z - I_z R_{z+1} N_{z+1})$ . Looking at the results for nickel in figure 3.16, it can be seen that in the core the difference between the techniques is negligible, while at the edge a variation of up to 20% occurs. This is attributed to the departure from coronal equilibrium of the injected impurity in the edge. Comparison of several different bundling schemes of tungsten, including one that reduces tungsten to 9 superstages, in the same

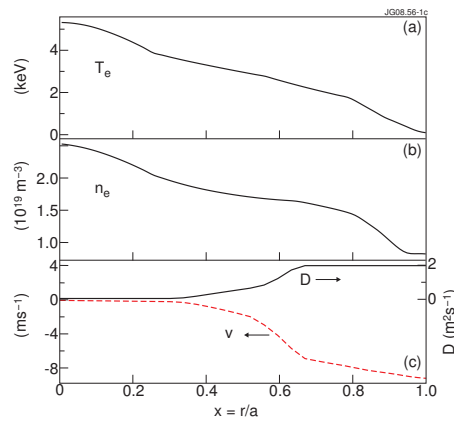


Figure 3.15: The theoretical plasmas which were used for the SANCO comparison runs for different superstaging systems. From [64].

background plasma shows a very good agreement with the unsuperstaged data for the plasma conditions here.

Further tests with the tungsten superstaging using the 1D model were implemented for a typical ITER plasma. An initial distribution of tungsten was allowed to evolve in a constant plasma. The distribution of tungsten after 10 seconds is shown in figure 3.17, and it is found that they are virtually indistinguishable.

### Two Dimensional Models

Testing the superstage theory in 2D models is harder than in the 1D case. The motivation for superstaging is to enable the use of heavy species atomic data in 2D models. It therefore follows that it is not possible to run the unsuperstaged case in these to compare with the results of superstaging. Therefore the comparison will be between two different superstaging schemes for tungsten. The two schemes are based upon the natural partitioning scheme, but with more aggressive bundling applied to the low stages for one case than the other. Both meet the EDGE2D constraints of 9 superstages and the neutral, singly ionised and fully ionised stages being isolated. The partition information is given in table 3.2.

A trace amount of tungsten was injected into the edge of simulated plasmas, and the results for the two runs are shown in figure 3.18. The two agree on the features present.

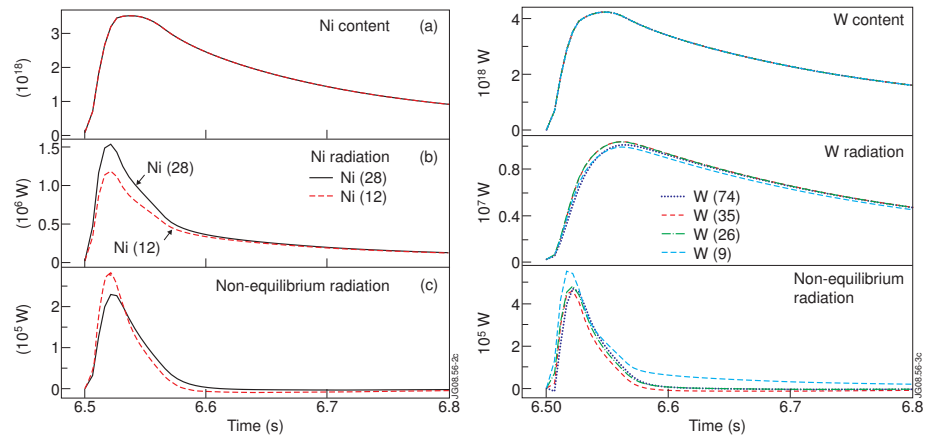


Figure 3.16: A comparison of the effect of different bundling schemes on the radiated power from nickel and tungsten. It can be seen that compressing tungsten to just 9 stages still produces very similar radiated powers to the individual stage results. From [64].

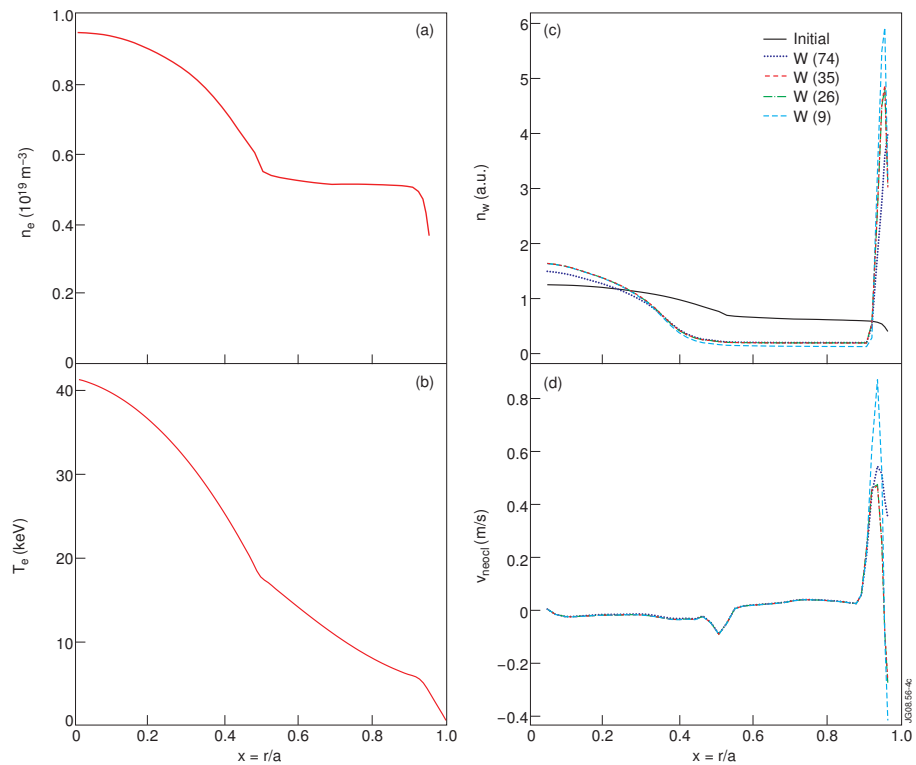


Figure 3.17: The predicted ITER plasma conditions used with superstaged tungsten, and the results of SANCO simulations using this data.

Superstage	Red	Black
p00	00	00
p01	01	01
p02	02-07	02-05
p03	08-12	06-07
p04	13-16	08
p05	17-18	09-12
p06	19-20	13-20
p07	21-26	21-26
p08	27-73	27-73
p09	74	74

Table 3.2: The two superstaging schemes used with tungsten in EDGE2D. The red and black labels refer to the colours used in figure 3.18

There is a discrepancy in the results for the two runs, however the magnitude of this discrepancy is small - the tungsten concentration is  $1 \times 10^{-6}$  that of the main impurity, carbon, so the differences being noticed here are very small. Also, the solution of EDGE2D is iterative, and tends to “bounce” around the correct solution. Given the small tungsten concentrations being observed here, it is not possible to say how much of this discrepancy is due to such bouncing. Even if this is negligible, the two bundling schemes do provide very similar results, which gives confidence that the superstaging of data in EDGE2D is functioning correctly and can be used for further modelling.

### 3.4 Conclusions

A system for generating a baseline set of atomic data using the Cowan code for any element has been created, allowing the rapid creation of the entire set of collisional-radiative coefficients and photon emissivity coefficients for use in experimental analysis. An automated system for selecting an appropriate set of configurations to include in these calculations has also been created.

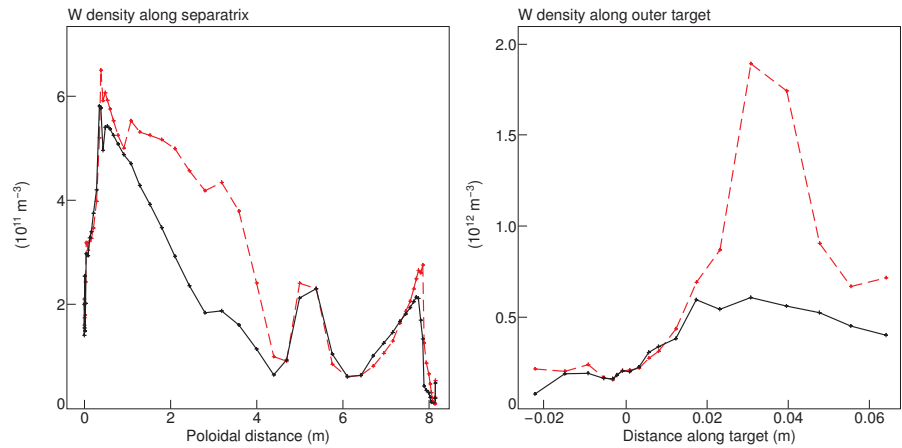


Figure 3.18: The density along the separatrix and the outer target obtained for different partitioning of tungsten, as detailed in table 3.2. For comparison the carbon impurity density is  $\approx 1 \times 10^{17} \text{m}^{-3}$ .

This data has been successfully used to analyse an experiment using the 1.5-D fluid code SANCO in chapter 4. For use with 2-D data, a system of superstaging has been developed, which groups together metastables to form a superstage in plasma modelling. This system has been developed in such a way as to preserve the flexibility to introduce high quality metastable resolved data for ionisation states of interest while bundling of other stages greatly reduces the computational intensity of the calculation while improving the numerical stability.

The superstage method has been used successfully to compress tungsten to 9 stages, allowing it to be used in EDGE2D simulations of JET and ITER plasmas. The superstaged data is found to be comparable to the un-superstaged data in the 1D case, and in the 2D case, where direct comparison is not possible, it is found that the effect of different bundling schemes is relatively minor. This gives confidence in the use of superstaging, which allows 2D fluid modelling at JET in the JAMS code suite for the first time.

## Chapter 4

# Experiments on MAST

Tungsten wall tiles are to be used for the majority of the ITER divertor due to the high melting point of tungsten and its resistance to the heat fluxes which will arrive at the divertor. It is estimated in [65] that the power flux to the divertor will average  $10\text{MW}/\text{m}^2$ . The divertor is designed to cope with transient events depositing up to  $20\text{MW}/\text{m}^2$  for up to 10 seconds. During this phase the erosion rate of the divertor tiles will be up to  $16\text{nm}/\text{s}$ . In the case of a rapid thermal quench of an ITER plasma (i.e. a disruption), the estimated power flux to the divertor leaps to  $100\text{GW}/\text{m}^2$  for 1ms. This leads to an erosion rate of  $\approx 35\mu\text{m}/\text{disruption}$  for the carbon tiles and, due to the formation of rapidly eroded melt layers on the surface of metallic components, up to  $25\text{-}75\mu\text{m}/\text{disruption}$  of Be and W.

The specifications in the ITER design state that the wall tiles should last for  $\approx 3000$  discharges. Using the assumptions on erosion above, this gives rise to an average loss of more than 6cm per tile during its lifetime. This can have several effects: in the worst case scenario, excessive erosion focused on one part of a tile may lead to a gap opening in the tile; in a less severe scenario, it may lead to an effective change in the divertor geometry which may impact on other components. In both cases, a method is required to identify when the tiles are about to erode beyond an acceptable limit.

One proposed method for erosion monitoring is implantation of impurity doped layers into the tiles of the ITER vessel wall. As the tile erodes the impurity layer is gradually exposed, causing a release of the impurity into the plasma. If such an impurity was to be observable spectroscopically then the occurrence of significant damage could be identified

and appropriate remedial action could be taken. The use of different elements in different parts of the vessel would enable the localisation of the damage to certain parts of the vessel, although this localisation is limited by the number of suitable elements available to use as dopants.

The doped layer method is an improvement over current inspection techniques used for tokamaks which is necessary as investigation of the inner surface of the ITER wall or, indeed, that of a working power plant would prove difficult if not impossible due to the radiation and, in the case of Be walls, toxicity issues inside the vessel. Certainly, shutting down a power plant for inspection would be less ideal than a passive monitoring system informing when a replacement is required.

There are several other possible methods of observing the depletion of the tile, the two most promising of which are the use of (at least) one force balance on each tile to measure the change in mass as time progresses, and a laser based system for measuring the distance from a fixed point to the tile, therefore measuring the erosion by the change in tile thickness. The former technique is seen as a fully viable method for measuring the erosion, however it does require the installation of many thousand force balances, taking up precious space in the vessel. This is unlikely to be a significant barrier to use, but ideally a mechanism would be found without this requirement. The second (laser based) mechanism works well in other industrial applications with accuracies of  $< 10\mu m$ , but is very expensive and the laser equipment could not be operated continuously, it would have to be moved into position occasionally and switched on.

Returning to the doped layer method, observation of the impurity in the plasma would ideally be done by existing (or already planned) spectroscopic systems. This would ensure that the technique is not financially prohibitive and does not require any further space in the already crowded ITER wall. The main determinant on this is the observability of the impurity in the plasma. There are two points at which the impurities can be observed: at their production immediately adjacent to the wall, or in the core plasma. The benefits of the wall observation are that any damage can be even further localised than it can be by simply using different elements. The disadvantage is that it requires spatially resolved impurity spectroscopy of the entire vessel surface. Core observation is simpler, and can be performed through single line of sight measurements in the vacuum ultra violet (VUV,  $\approx$

100 to 1000Å) or soft x-ray (SXR,  $\approx 10$  to 100Å) regions of the electromagnetic spectrum, however localisation is harder and there is a requirement for the impurity to reach the plasma core instead of redepositing immediately elsewhere on the wall.

Impurity studies have been carried out on nearly all tokamaks, either to study the impurities directly or to study features of the plasma, such as rotation or heat transport. Commonly extrinsic impurities are introduced to the plasma by laser ablation from a target made from the material of interest (e.g. [66]) or, in the case of gaseous elements, puffed into the vessel from a source at the edge (e.g. [67]). Intrinsic impurities can originate from the surfaces of plasma facing components, either being the elements from which they are made (usually graphite or metals such as nickel and iron) or deposited impurities such as oxygen from water vapour which accumulates during engineering breaks while the vessel is not under vacuum.

Experiments were carried out on MAST using both divertor and midplane sources to introduce impurities to the plasma by erosion instead of laser ablation or gas puffing. Heavy elements were chosen for the midplane probe - indium and tin (atomic number 49 and 50 respectively) - while the lighter element aluminium was used additionally on the divertor target as it has a lower sputtering threshold than the heavy elements and the power flux in this region on MAST is much lower than at the midplane. These experiments had several objectives:

- Demonstrate the release of heavy species by erosion from a fabricated probe tip into the core plasma.
- Observe spectral line features of neutral heavy species at the source and higher stages in the core.
- Identify the spectral line features.
- Establish relationship between source sputtering/influx and core concentration by comparing experimental results with theoretical transport modelling.

These experiments will be described in this chapter, starting with a brief description of the plasma-surface interaction model used here.

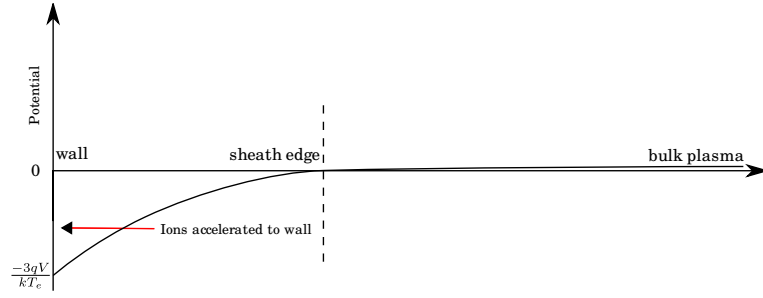


Figure 4.1: The potential drop at a floating surface in a plasma. The ions in the sheath edge are accelerated by the electric field produced by this potential drop. There is a small positive electric field in the bulk plasma (typically  $10^{-5}E_{sheath}$ ).

## 4.1 Plasma Surface Interactions Model

The models used in this work for the interaction between the plasma and the impurity samples will be described in this section. It will be used to obtain the energy of the ions colliding with the walls and then to estimate the physical sputtering yield for the impurities. It assumes the majority of the ion energy is gained on approach to the surface as the ion passes through the plasma sheath, and is based on a description in [68].

Electrons and ions which are at the same temperature in the bulk plasma, have different velocities due to their differing masses. The faster moving electrons collide with an electrically floating surface (such as walls or the impurity samples in these experiments) more rapidly than the ions. This leads to a build up of negative charge on the surface, which creates an electric field between the wall and the plasma, in a region known as the sheath. This sheath region is typically treated as having a width of a few Debye lengths, but in reality it is an artificial construct and therefore does not have a definable size. The electric field in the sheath acts to repel electrons and accelerates ions towards the surface, until the flux of both to the wall is equalised. This occurs when the plasma is floating at a potential of  $V = -3q/kT_e$ . The potential drop in the sheath is shown in figure 4.1.

Ions moving in the scrape off layer (SOL) of the plasma have a Maxwellian velocity distribution. Making the common assumption that within the SOL  $T_e = T_i$ , the velocity of the ions which collide with the walls can be estimated. As they approach the sheath edge, the Bohm criterion [69] shows that the ions form a drifting Maxwellian, with bulk

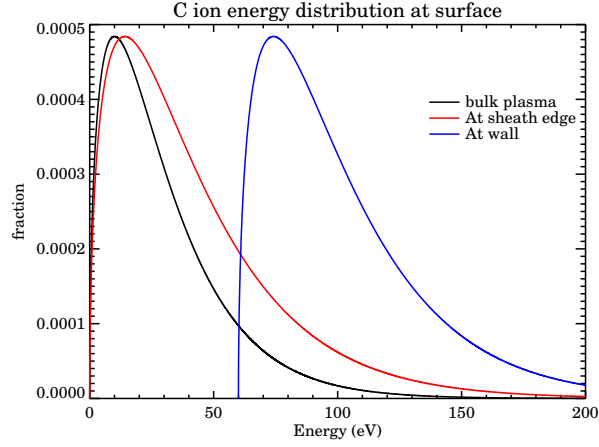


Figure 4.2: The increase in energy of a  $C^{+1}$  ion approaching a surface at 20eV. In the bulk plasma, the energy has a Maxwellian distribution (black curve). At the sheath edge, a drifting Maxwellian has formed with drift velocity equal to  $\sqrt{2}c_s$  (red curve). The ions then undergo an acceleration due to the sheath electric field, gaining energy  $3kT_e$  (blue curve).

velocity equal to  $\sqrt{2}$  times the ion sound speed,  $c_s$ :

$$v = \sqrt{2}c_s = \sqrt{\frac{4kT_e}{m_i}} \quad (4.1)$$

Once in the plasma sheath, each ion undergoes an acceleration due to the electric field, gaining energy  $3kT_e$ , as shown in figure 4.2. This assumption of a shifted Maxwellian velocity distribution is not, in fact, an accurate representation of the ions which will collide with a surface: in reality, there are no backward travelling ions, for example. It is found however that for the purposes of sputtering calculations this representation gives good results provided that the ion energies are not below the sputtering threshold for the element. Therefore this assumption will be used in this work.

For determining the flux of ions to the surface, the assumption is made that any ions which cross the sheath edge will collide with the surface. The flux  $\Gamma$  of ions to the target is therefore determined by the drift velocity in the bulk plasma (or SOL) :

$$\Gamma = N_{ion}c_s \quad (4.2)$$

## 4.2 Experimental Setup

The experimental setup for the two different sets of experiments differed slightly due to the locations of the different impurity sources and the different availability of spectrometers. The midplane experiments were performed first, from 19th August 2005, with the divertor experiments following from 12th April 2007.

### 4.2.1 Introduction of Impurities

For the midplane impurity source experiments, use was made of the existing MAST reciprocating probe (RP) system. This system is designed for taking measurements of the scrape off layer and edge plasma conditions in the MAST device using Langmuir probes[70] to obtain temperature, density, Mach number and flow measurements using a variety of interchangeable heads. The probe is mounted horizontally on the outboard midplane of the MAST vessel. It can be moved radially inwards until the tip is at a radius of 1.2m from the centre column, although since the typical MAST plasma radii are  $\approx 1.4$  this full extent is not used. The probe is capable of reciprocating up to 10cm during 300ms using a pneumatic drive. For SOL measurements this allows the probe to be kept away from the plasma during start up and disruptions while measuring during the relatively stable part of the shot. For impurity introduction this is ideal as it allows the impurity to be introduced again only during the relatively stable steady-current of the shot.

Previous experiments had been carried out using an old impurity probe on the RP system in 2004 - a schematic of the head used is shown in figure 4.3. These experiments had tried to introduce silicon and silver into the MAST plasma using two small coupons of silicon, one of which was coated with silver. Significant difficulty was found in introducing observable quantities of material without disrupting the plasma, although silicon was eventually successfully observed in the core plasma. The main source of the difficulty appeared to be that the graphite used for blackening the end of the probe to avoid interference with other optical diagnostics redeposited in significant quantities on the impurity samples, resulting in significantly reduced impurity erosion.

A new impurity head was therefore designed for use on the RP system, aiming at enhancing the introduction of impurities. The new design is shown in figure 4.4. The

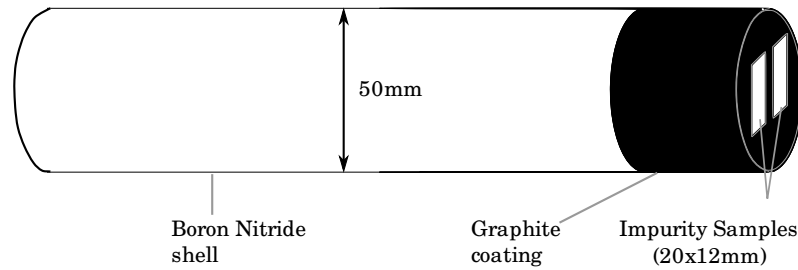


Figure 4.3: The old materials probe head used in the M3b campaign in 2004. The impurity samples were mounted flush with the end of the probe and were found to be rapidly coated with carbon from adjacent areas of the probe tip.

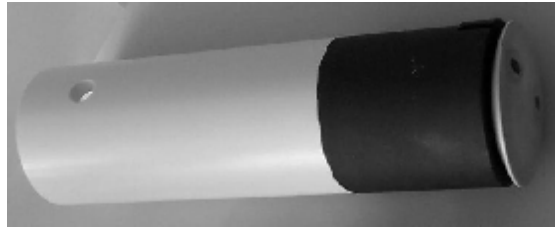


Figure 4.4: The new materials probe designed for use in midplane impurity experiments. This probe was used in the experiments in this work.

domed upper surface was designed to maximise the area of impurity exposed to the plasma. The “mushroom” shape acts to shield the upper surface of the impurity from redeposition of the carbon coating on the probe tip - the majority lands on the underside of the head. Two Langmuir probes were mounted in the probe tip to allow for local measurements of  $T_e$  and  $N_e$ .

To accurately represent the proposed erosion diagnostic it would be ideal to use either a doped carbon layer on the impurity surface or to use an impurity coating covered with a carbon layer. However such an approach is not practical on MAST: due to the much lower power fluxes compared with those of ITER, no appreciable erosion was expected in the available three experimental sessions, and there was no scope for extending the work — the reciprocating probe system is in high demand on MAST and only one head can be used at a time, with a four day change over time. Therefore the decision was made to use pure impurity layers.

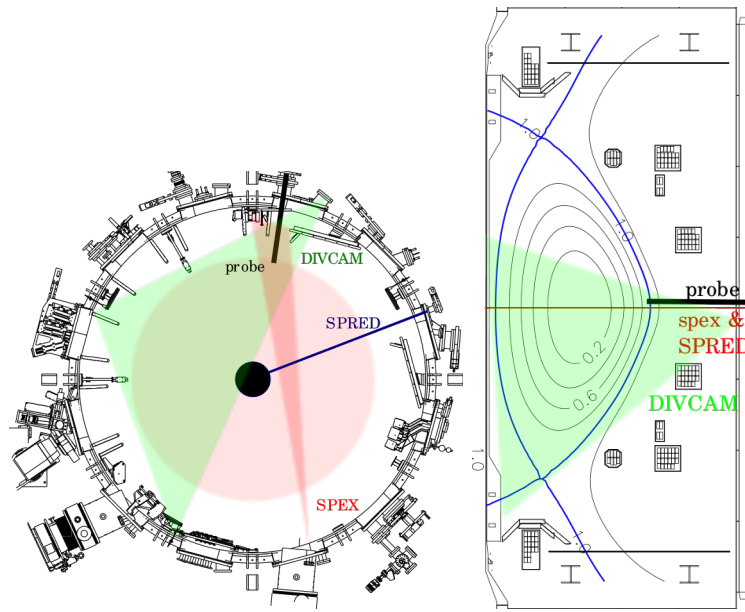


Figure 4.5: The positions and field of view of the spectrometers and cameras used in the midplane experiments: DIVCAM (green), SPRED (blue) and SPEX (red).

The choice of tin and indium as the elements was made based upon the observability of their spectrum lines in a MAST plasma (with carbon, helium, nickel and iron as the other main impurities present) given the spectroscopic coverage available (see section 4.2.2). Another important consideration was the practicality of the element for coating the substrate, in this case boron nitride, which led to the choice of transition metals.

### 4.2.2 Spectroscopy

The spectroscopic suite on MAST used to analyse these experiments was similar for all experiments, although filters used with cameras changed between experiments. There were also differences in the location and/or viewing angle for some of the visible spectrometers. The layout for the midplane experiments is shown in figure 4.5.

#### SPRED

The SPRED spectrometer[71] is a grazing incidence multi channel VUV spectrometer attached directly to the vessel vacuum. The line of sight of the spectrometer is a pencil-

beam horizontal chord on the midplane of the vessel, pointing radially inwards to the centre column. The time resolution of the spectrometer is 16.7ms during full detector operation. By reducing the number of pixels which are being read the frame rate can be increased, however this was done only once during these experiments.

The exact wavelength coverage of the spectrometer is determined by the holographic grating in use: in normal operation the 450g/mm (grooves per millimeter) grating is used providing coverage from 100Å to 1000Å, with energy resolution  $E/\Delta E$  of 260. The other grating used here is the 2105g/mm,  $E/\Delta E = 380$ . Wavelength calibrations of SPRED are relatively simple as the major impurity lines likely to appear in its spectrum are well known. The last absolute calibration (which converts between the voltages recorded by the spectrometer and photon intensities) was performed in 2002, more than three years before these experiments began, when the 450g/mm grating was calibrated against a helium source. No records of calibration for the 2105g/mm grating could be found, therefore an ad-hoc cross calibration between the two gratings involving the He<sup>+1</sup> Lyman series lines had to be used for analysis.

## SPEX

The SPEX spectrometer consists of a SPEX 1870 0.5m monochromator with a EG&G PARC 1420 linear diode array as the detector. This combination provides a spectral range of any 300Å wavelength band in the visible region. There is a rapid decline in the sensitivity of the system due to the low transmittance of the glass fibre below 4000Å, and at long wavelength the sensitivity drops due to low photon energy, therefore the ideal operating range is between 4000Å and 7000Å.

SPEX is connected to the vessel by a 38m optical fibre, which can view the plasma through any available window. The fibre can be moved easily around the torus and the precise viewing angle is dictated by the properties of the lens. The emission from heavy species in the visible region is from neutral and near-neutral stages, therefore for these experiments the views selected were aimed towards the probe head. A view from almost opposite the probe was used with a narrow field of view to encompass the entire probe head and the light in the immediate region around it. The diameter of the viewing cone is 18cm at the probe surface.

An absolute calibration of SPEX was performed with an integrating sphere after each experiment was concluded. A separate calibration was required in each case to account for changes in fibre, lens and/or wavelength.

### **Ocean Optics**

The Ocean Optics HR4000 spectrometer used in these experiments is a much smaller spectrometer than the SPEX system, with similar time but much lower spectral resolution. It does, however, cover the entire visible range from 4000Å to 7000Å.

When it was in use, the Ocean Optics spectrometer shared the optical fibre used by SPEX, with a beam splitter inserted. During the midplane experiments, the spectrometer was not connected to the MAST timing system, therefore the data recorded were useful only for noting lines which did not fall in the range of SPEX. During the divertor experiments the system was fully integrated to the system and so quantitative measurements could be obtained after calibration with an integrating sphere.

### **DIVCAM**

The DIVertor CAMera was installed on MAST in early 2005. It consists of two telecentric CCD cameras which share exactly the same view. Filters in front of each CCD enable the capture in 2D of emission from two different spectral lines simultaneously. The filters can be changed remotely, allowing shots to be repeated to analyse the line emission from further species as desired. Filters were purchased to allow observation of Sn and Al lines as listed in table 4.1. The time resolution of the diagnostic is variable but for these shots was kept at or above 20ms to ensure reliable operation.

The DIVCAM was mounted behind the probe during midplane experiments, viewing the impurity sample from behind. It was not absolutely calibrated, but was used to give a general perception of where the Sn was ionising. Attempts were made to use it during divertor impurity experiments but the probe was not within the line of sight of any of the viewports on which the camera can be mounted.

Filter ID	Species	Transition	$\lambda(\text{\AA})$	Transmission(%)
452.7/2/25D	Sn I	$5p6s \ ^1P_1^o \rightarrow 5p^2 \ ^1S_0$	4524.7	62
	Al III	$2p^64d \ ^2D_{3/2} \rightarrow 2p^64p \ ^2P_{3/2}^o$	4528.9	57
	Al III	$2p^64d \ ^2D_{5/2} \rightarrow 2p^64p \ ^2P_{3/2}^o$	4529.2	57
532FS03-25	Sn II	$5s^26d \ ^2D_{3/2}^o \rightarrow 5s^26p \ ^2P_{1/2}$	5332.4	37

Table 4.1: The filters available for studying impurities using cameras. No filters were used for indium due to the cameras being used for other experiments during those sessions.

### 4.3 Midplane Impurity Probe Results

Several experimental sessions were spent using the midplane probe. The initial, and more successful, experiments were performed with tin as the impurity sample. Therefore the description here will describe the tin experiments initially and then return to indium where the results differ.

The Sn probe was introduced to both upper and lower single null plasmas (USN and LSN), with ohmic heating only and with auxiliary heating in the form of neutral beam injection (NBI). Tin was successfully observed at the source and in the core of the plasma for all configurations, although the NBI heated configurations were found to be less stable, tending to disrupt when interacting with the probe, while ohmic ones were more resilient. Typical plasma parameters are shown in figure 4.6. Impurity lines of tin were successfully observed on both the visible and the VUV spectrometers in all plasma configurations, although the signals observed when using NBI heated plasmas were intermittent due to the instability of the plasma.

The objective in the plasma scenarios chosen for this work was to obtain a LSN plasma which was identical to the USN plasma used, but inverted. It is, however, not possible to achieve this full reversal without reversing the direction of the main plasma current. This can, and is, done on MAST but requires dedicated campaigns, of which this experiment was not a part, therefore these plasmas are not exact replicas. Nevertheless, there are significant similarities in the two plasmas, as shown in figure 4.6. The plasma temperature and density profiles are very similar and the MHD activity is similar, if much less

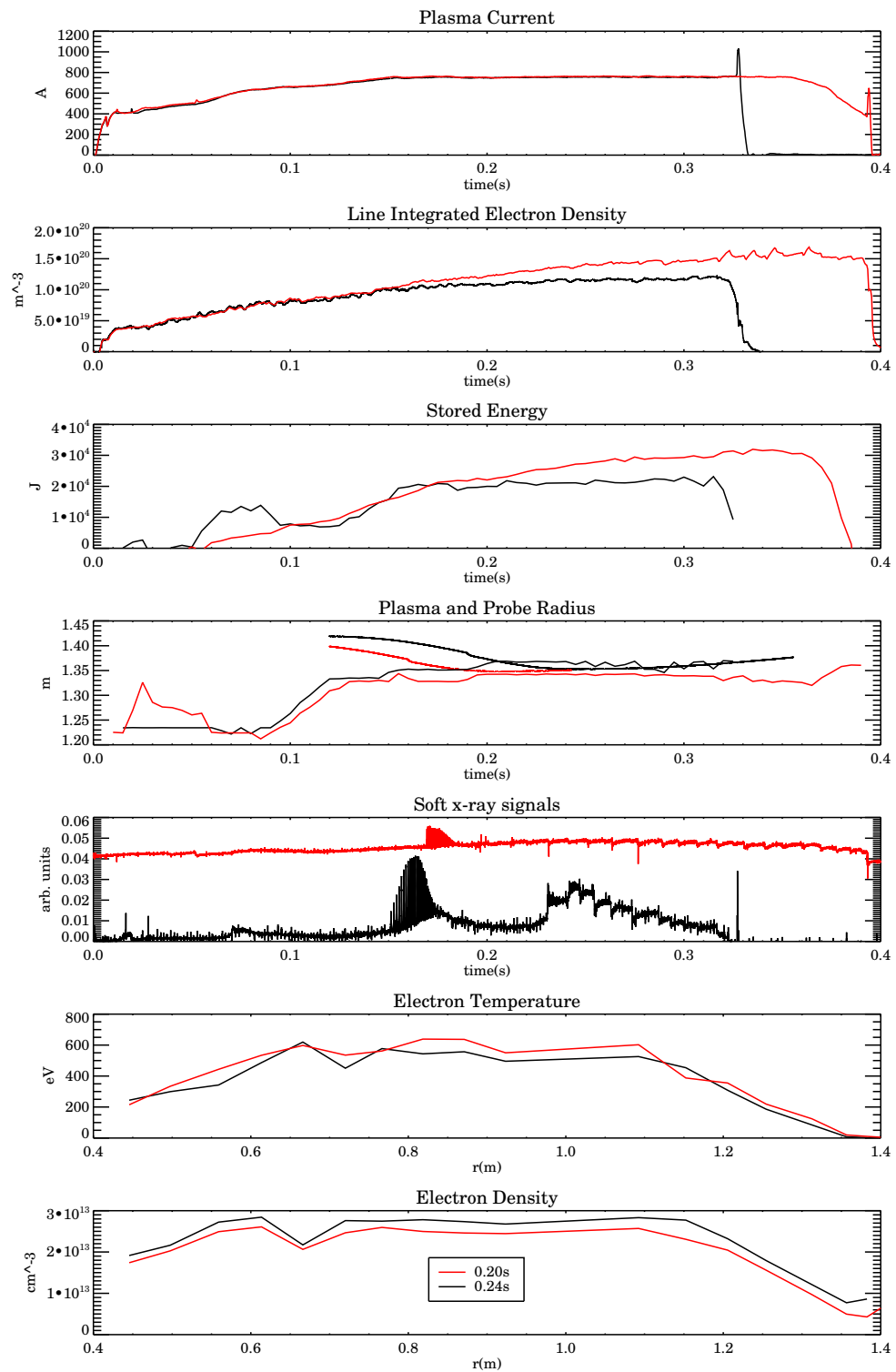


Figure 4.6: Typical plasma parameters for USN shot 13835 (black) and LSN shot 14480 (red) MAST plasmas used with the midplane probe on MAST.

pronounced in the LSN case, as is shown in the soft x-ray trace. One major difference is the stored energy in the plasma: it is frequently observed on MAST that the USN plasmas have only 2/3 of the stored energy of LSN ones, and this was also the case for these plasmas.

Analysis of these results requires a significant use of atomic data as described in chapter 2. Here, the existence of the atomic data will be assumed. It was, in fact, required to generate all the data from scratch, as there is little to no existing atomic data for tin and indium. This was done as described in chapter 3.

### 4.3.1 Core Impurity Observations

Sn was successfully observed in the core of the MAST plasmas in both USN and LSN plasma configurations. During the first session, SPRED was used operating on the standard 450g/mm grating. A sample spectrum is shown in figure 4.7. All observed tin lines were found to be in the  $< 300\text{\AA}$  region, therefore the grating on SPRED was changed to the 2105g/mm to provide a higher resolution of these lines. The feature at  $130\text{\AA}$  arises from the  $4p^6 4d^{x-1} 4f \rightarrow 4p^6 4d^x$  and  $4p^5 4d^x \rightarrow 4p^6 4d^{x-1}$  transition arrays from all the stages of Sn from  $\text{Sn}^{+8}$  to  $\text{Sn}^{+13}$ . The line features have been identified in table 4.2.

A sample spectrum for two LSN shots, 14479 for Sn and 15100 for In are shown in figure 4.8 and figure 4.9 along with a simple predicted spectrum using the temperature and density profiles of the shot. These simple predictions are made assuming a steady state ionisation balance and an even distribution of tin across the tokamak - clearly this is unlikely in the current experiments. However the simple prediction and observation do provide a qualitative match.

Comparing the time history of the observed impurity lines with the distance between the probe and the plasma shows, as expected, a strong correlation between the two. This is shown in figure 4.10 for two lines from the Zinc like stages of the impurities.

### 4.3.2 Edge Impurity Observations

The observations at the edge of the plasma were used primarily to estimate the erosion of impurity from the probe tip, and therefore its influx into the core.

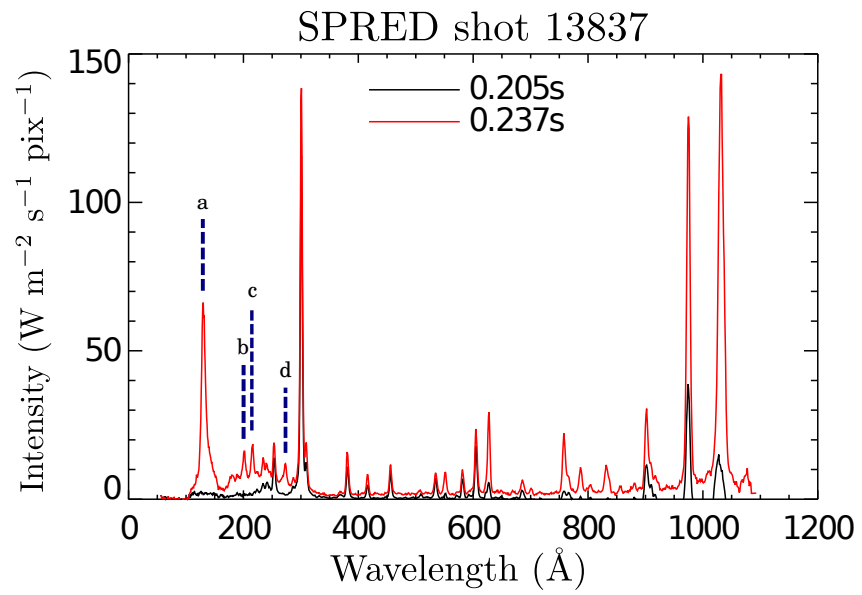


Figure 4.7: The VUV spectra recorded on SPRED for shot 13837. The black line is data recorded before any significant probe-plasma interaction occurs, the red during the peak interaction. Lines attributed to tin are marked by a vertical blue dashed line, and are described in table 4.2. There are other lines which appear or greatly increase in amplitude, these are attributed to carbon emission.

Label	$\lambda_{\text{obs}}$ (Å)	$\lambda_{\text{Cowan}}$ (Å)	$\lambda_{\text{lit}}$ (Å)	Species	Transition
a	$\approx 135$	-	-	Sn IX-XIV	$4p^5 4d^x \rightarrow 4p^6 4d^{x-1}$
b	204	211.3	204.8	Sn XXI	$4s4p \ ^1P_1 \rightarrow 4s^2 \ ^1S_0$
c	219	219.0	219.0	Sn XXII	$4p \ ^2P_{3/2} \rightarrow 4s \ ^2S_{1/2}$
d	276	271.0	276.1	Sn XXII	$4p \ ^2P_{1/2} \rightarrow 4s \ ^2S_{1/2}$
e	$\approx 145$	-	-	In VIII-XIII	$4p^5 4d^x \rightarrow 4p^6 4d^{x-1}$
f	218	224.0	216.9	In XX	$4s4p \ ^1P_1 \rightarrow 4s^2 \ ^1S_0$
g	233	232.5	232.6	In XXI	$4p \ ^2P_{3/2} \rightarrow 4s \ ^2S_{1/2}$
h	289	283.6	288.9	In XXI	$4p \ ^2P_{1/2} \rightarrow 4s \ ^2S_{1/2}$

Table 4.2: The observed (obs), calculated (cowan) and true (lit) wavelengths from [72] for the Sn and In lines which were observed on the SPRED spectrometer in the VUV region. The feature at  $\approx 135\text{Å}$  is a composite of many lines for transitions for many stages of Sn, as is the feature at  $145\text{Å}$  in In, therefore no wavelength is listed. There is another resonance line of Sn XXI at  $301.7\text{Å}$ , but this is obscured by the He II line at this wavelength and is therefore not considered here.

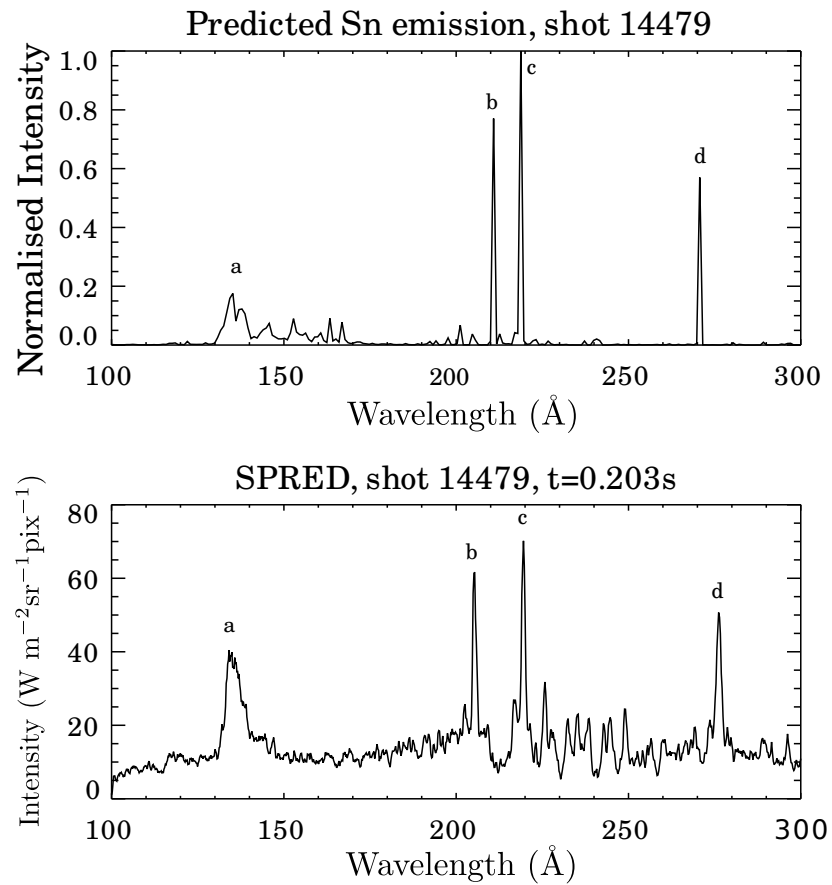


Figure 4.8: The (upper) predicted and (lower) observed spectra for Sn in MAST shot 14479. The labels correspond to those in table 4.2

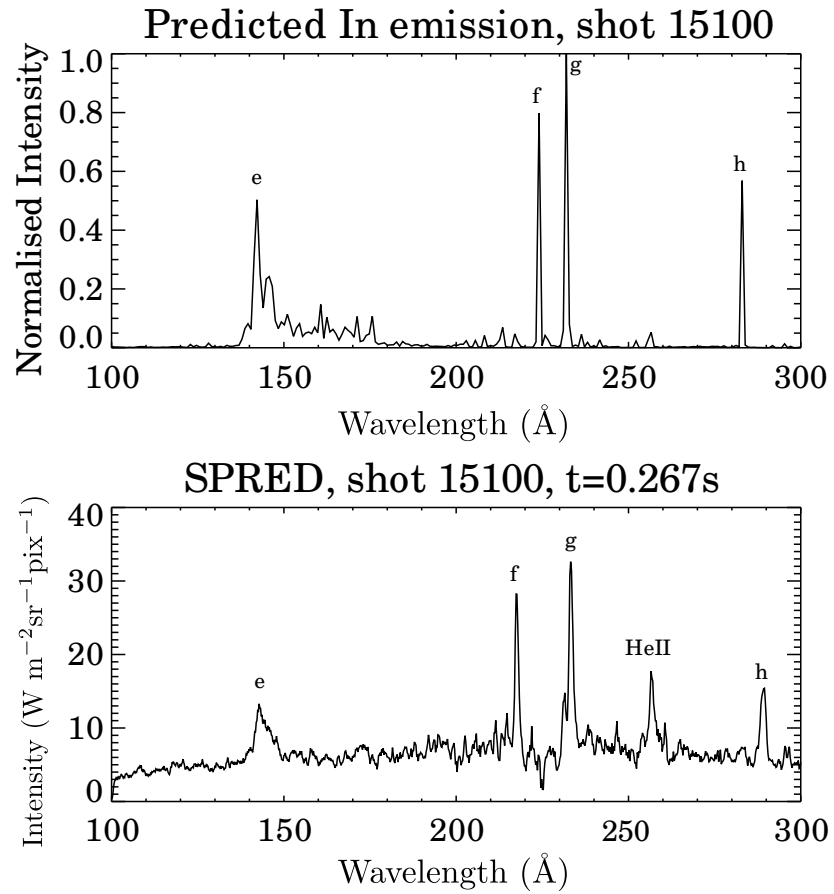


Figure 4.9: The (upper) predicted and (lower) observed spectra for In in MAST shot 15100. The strong line which appears at  $256\text{\AA}$  is from He II. The labels correspond to those in table 4.2

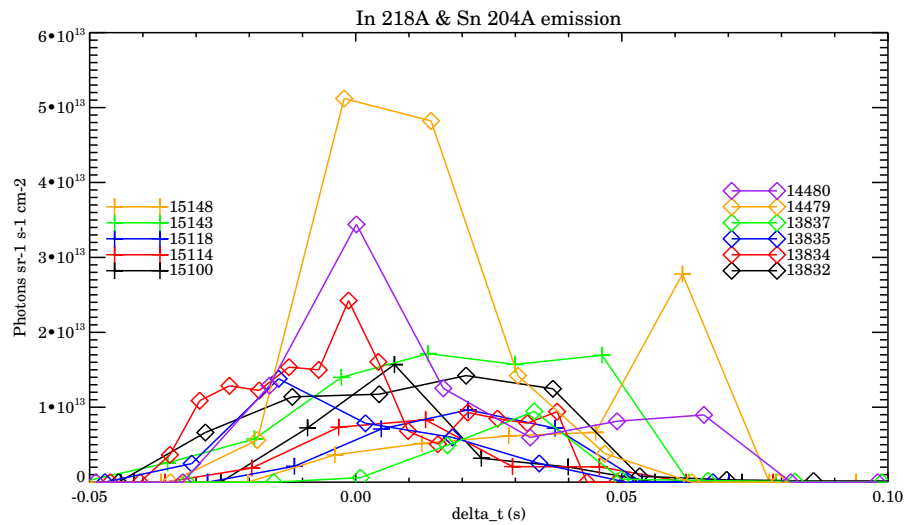


Figure 4.10: The time history of a (diamonds) Sn XXI and (crosses) In XXII line observed on SPRED from the shots in which they were successfully observed in the core of the plasma. Time  $t=0$  is taken to be when the probe to plasma distance is minimised, corresponding (approximately) to the peak interaction between the probe and plasma.

## DIVCAM

An image observed during a shot is shown in figure 4.11. This image shows the probe from the rear, comparing the deuterium-alpha ( $D_\alpha$ ) emission and the Sn II emission. The image is of little quantitative value, but it does provide a useful confirmation that nearly all the Sn II emission occurs within the field of view of the SPEX spectrometer, which at the probe tip has a diameter of 18cm. Due to this, the assumption will be made that all the Sn II emission in the plasma has been captured by this lens.

## SPEX

Both Sn and In lines were successfully observed on SPEX during the midplane experiments. Spectra showing these lines are shown in figure 4.12, and the lines are identified in table 4.3. Line identification was performed by comparison of predicted strong lines from Cowan with wavelengths obtained from NIST.

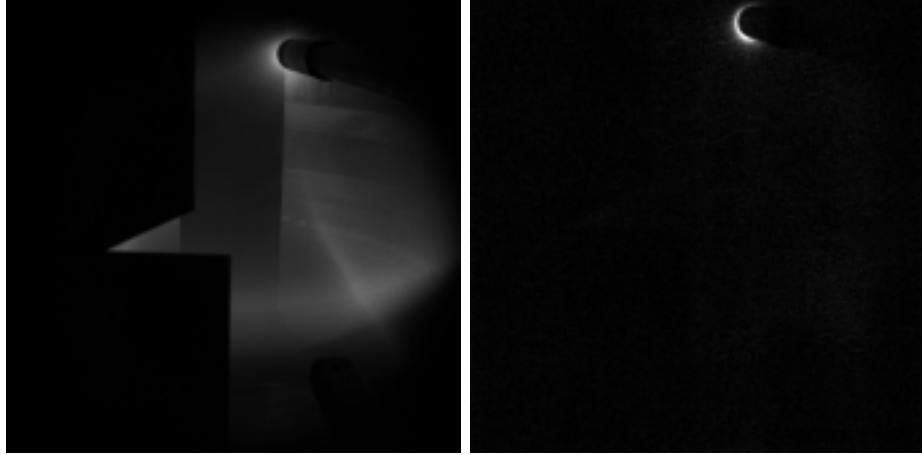


Figure 4.11: The DIVCAM image recorded at 0.259s for MAST shot 13835. The left panel shows the  $D_\alpha$  filtered emission while the right panel shows the image through the filter centred on the Sn II line at  $5798\text{\AA}$ . The probe can be seen interacting with the plasma, with a “halo” of Sn and  $D_\alpha$  emission surrounding the front.

Label	$\lambda_{\text{obs}}$ ( $\text{\AA}$ )	$\lambda_{\text{cowan}}$ ( $\text{\AA}$ )	$\lambda_{\text{lit}}$ ( $\text{\AA}$ )	Species	Transition
j	5333.5	5514.1	5332.4	Sn II	$5s^26d \ ^2D_{3/2} \rightarrow 5s^26p \ ^2P_{1/2}$
k	5350	5197.7	5349.4	Sn III	$5s6p \ ^3P_1 \rightarrow 5s5d \ ^3D_2$
l	5370	5221.2	5369.5	Sn III	$5s6p \ ^3P_0 \rightarrow 5s5d \ ^3D_1$
m	5564.5	5727.1	5562.0	Sn II	$5s^26d \ ^2D_{5/2} \rightarrow 5s^26p \ ^2P_{3/2}$
n	4513	4193.8	4511.3	In I	$6s \ ^2S_{1/2} \rightarrow 5p \ ^2P_{3/2}$

Table 4.3: The observed (obs), calculated (cowan) and true (lit) for the Sn and In lines which were observed near the probe tip on SPEX. The labels refer to those in figure 4.12. The wavelengths from the literature are from [73] for Sn and [74] for In

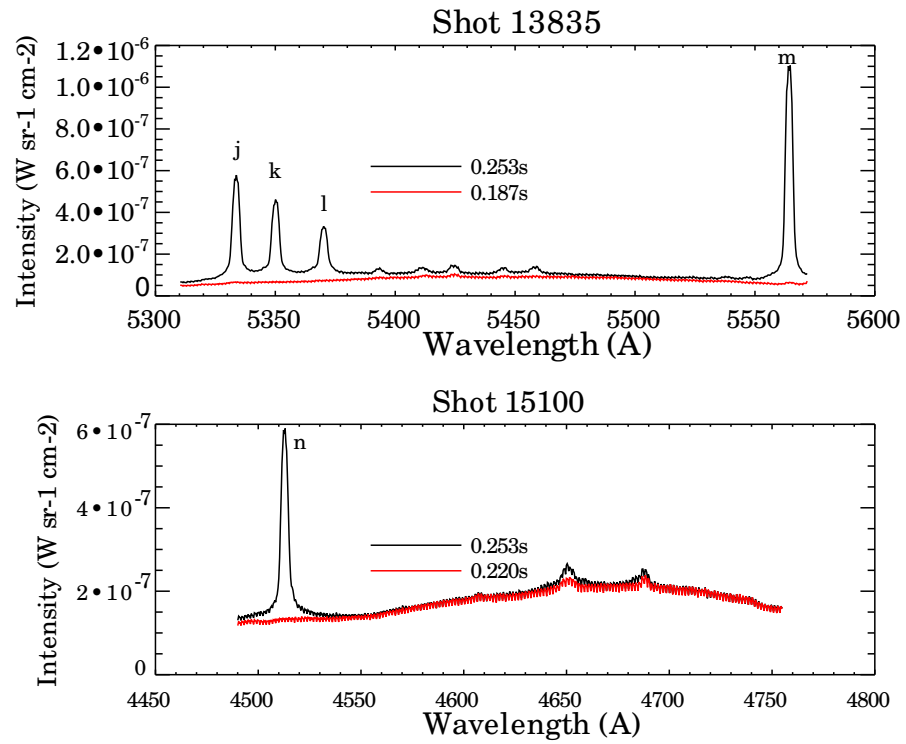


Figure 4.12: The spectra recorded on SPEX-A for two MAST shots, viewing the materials probe tip both before and during the plasma-probe interaction. The upper frame shows lines of Sn, the lower shows In. The lines are labelled by letters and are identified in table 4.3.

## 4.4 Influx Estimates

In order to estimate the influx of impurity into the plasma, two methods have been utilised. The first method is the use of the  $\mathcal{SXB}$  ratio[75], defined in section 2.3.2, to estimate the influx. As was observed on DIVCAM in figure 4.11, the emission from the neutral and singly ionised states of Sn and In is from very close to the probe tip. Using Thomson scattering measurements to obtain the local  $T_e$  and  $N_e$  in this region, and making the assumption that all Sn and In that is observed enters the plasma, it is possible to obtain an influx measurement.

The second method that was utilised was the Stopping Range of Ions in Matter (SRIM) package[76], which calculates the damage done to a surface by bombarding it with a beam of atoms/ions, allowing the calculation of the sputtering yield of ions from the surface. By varying the beam parameters it is possible to simulate a plasma interacting with the surface, thereby gaining an estimate of the physical sputtering. More details of this are given in section 4.4.2

As can be seen in figure 4.13, there is little significant emission (and therefore, it is assumed, little sputtering) until the probe approaches within one Larmour radius of the plasma edge; indeed, in many cases little is observed until the probe is inside the LCFS. It should be noted that, as well as errors in the measurement of the position of the LCFS, any particle within 1 Larmour radius of the separatrix can be deemed to be in the confined plasma as it will be inside it for 50% of the time. Therefore any sputtered ions are highly likely to enter the core without being involved in any significant SOL interaction. For this reason it was decided in the end that SOL modelling would not be useful for analysing these experiments.

### 4.4.1 $\mathcal{SXB}$ Influx

The  $\mathcal{SXB}$ [75] ratios for the four Sn and one In line observed have been calculated. These are shown in figure 4.14 as a function of temperature. It is noted from these plots that the ratios are highly sensitive to temperature, so much so that the influx ratios, as shown in figure 4.16, can vary by several orders of magnitude between shots.

Between the early shots with Sn (shot numbers less than 14000) and the later shots, a

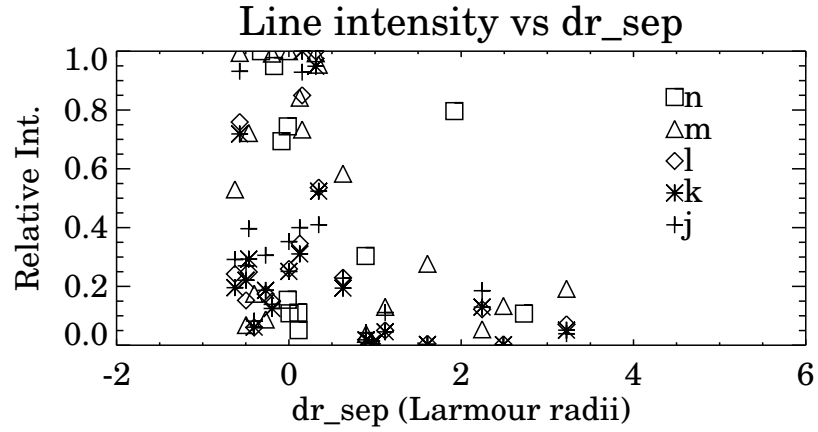


Figure 4.13: The intensity of the different lines observed on SPEX as a function of the probe to separatrix distance,  $\delta r_{\text{sep}}$ . The distance is given in units of Larmour radii ( $\approx 2\text{cm}$  for singly ionised Sn and In ions depending on plasma conditions). The line intensities are normalised against the maximum line intensity observed during all shots. The different symbols refer to the line indices in table 4.3

major upgrade to the MAST Thomson scattering system came on line[77]. This upgrade uses a large collection lens to observe the edge region of the plasma, and therefore obtains a much better spatial resolution and accuracy. The effect of this is shown in figure 4.15. It has been assumed that the probe tip conditions are best described in these latter shots, therefore the numbers which will be used here originated from these estimates.

A plot of these estimated influxes resulting from these  $\mathcal{SXB}$  values for several shots is shown in figure 4.16. It is noted that the expected influx for shot 14479 (and 14480, though it is not shown) are much smaller than those for similar shots. This can be attributed to two main factors: during these shots the probe did not actually enter the core plasma, whereas in all others it did; and the improved TS system leads to measurement of a much lower electron temperature in this region. The latter fact may, of course, again be a factor of being outside the LCFS, but it is still true that in these regions the old system was not sensitive enough to reliably observe these points, leading to higher estimates of  $T_e$  in similar circumstances.

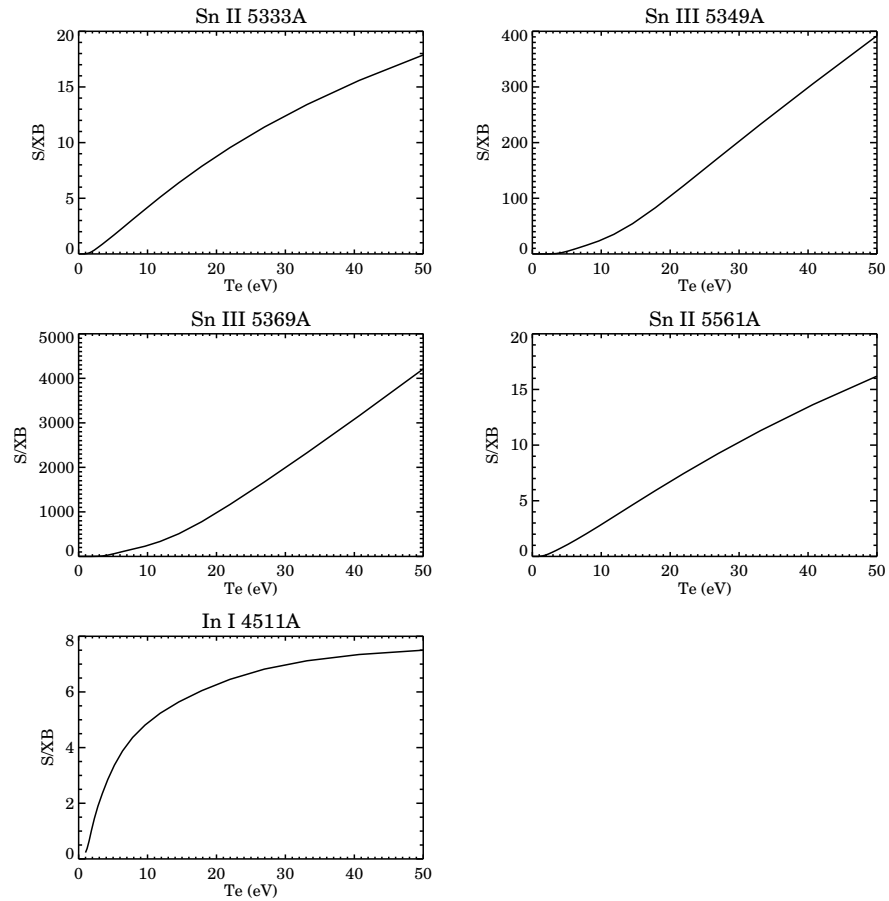


Figure 4.14: The  $SXB$  ratios for the observed Sn and In near-neutral stages as a function of  $T_e$ . The  $SXB$ s are a much slower varying function of  $N_e$ .  $N_e = 3 \times 10^{12} \text{cm}^{-3}$  has been assumed in these figures.

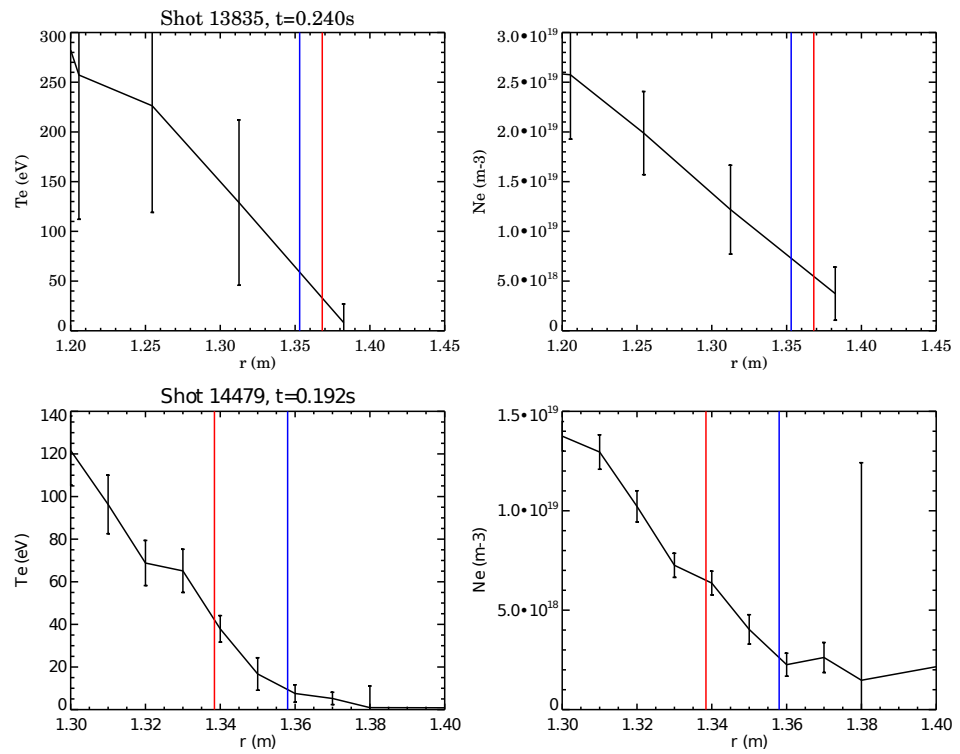


Figure 4.15: A comparison of the edge temperatures obtained before (shot 13835) and after (14479) the new edge Thomson Scattering system was installed. The blue line marks the probe position and the red the last closed flux surface. Note the different scales in each case.

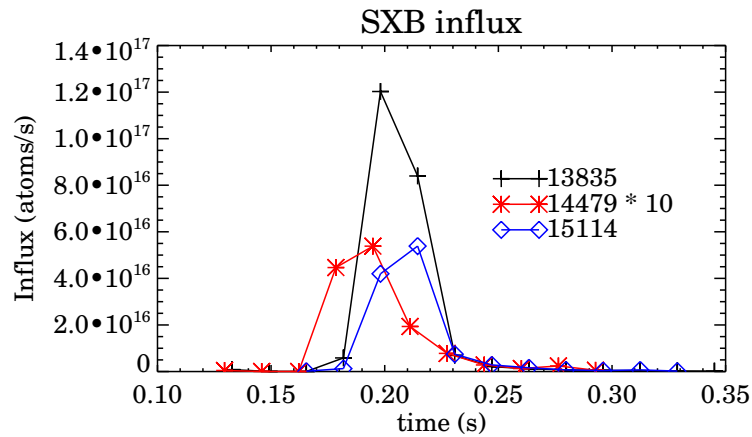


Figure 4.16: Influx estimates obtained for several shots from observed photon counts and  $SXB$  calculations. The influx for shot 14479 has been multiplied by 10 for clarity on the graph.

#### 4.4.2 Sputtering Calculations

The large uncertainties in the results for the  $SXB$  estimated influxes led to the use of a second method to cross-check the results. Unfortunately, the physical sputtering coefficient for an impurity by an ion is also highly dependent on plasma conditions, especially ion densities and temperature. In particular it is the non-linear dependence on impacting ion energy which matters the most. An example of this is shown for carbon and tin ions impacting on an Sn surface in figure 4.17. Deuterium sputtering of tin is negligible.

The SRIM[76] code uses a Monte-Carlo model to track an ion impacting on a material (substrate). It calculates collisions between any incoming particles and substrate atoms, and all resulting displaced substrate atoms are then tracked and so on until the entire cascade for the ion is dealt with. There is also a stopping power associated with the electrons in the substrate, which are treated as a free electron gas, resulting in an exponential decay in ion energy within the substrate on top of that due to ion-atom collisions. Any displaced ions which reach the surface of the substrate during these cascades and have an energy greater than the surface binding energy of the material are counted as sputtered, and are no longer tracked. Their trajectory and energy are recorded. The energy of the incoming ions is determined from the plasma sheath conditions, as described in section 4.1.

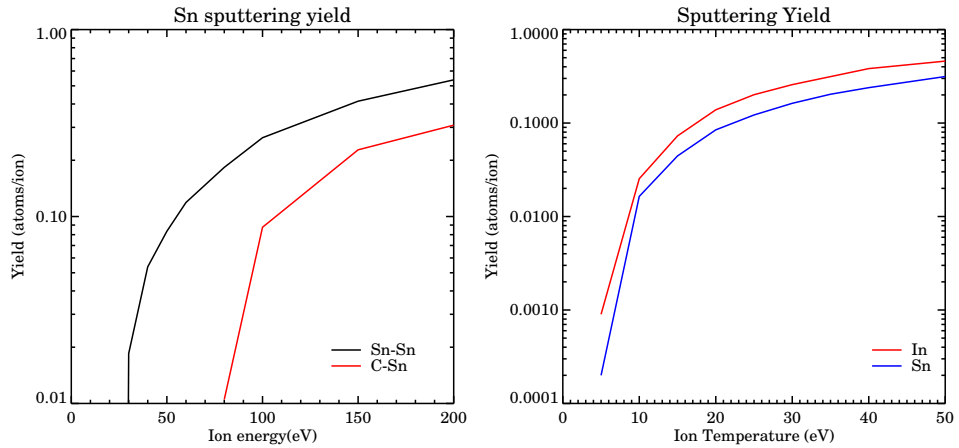


Figure 4.17: Physical sputtering estimates from SRIM[76]. The left panel shows the physical sputtering yield of Sn atoms as a function of impacting ion energy for Sn and C as the incoming ion. Deuterium sputtering is found to be negligible. The right panel shows the sputtering yield for C atoms with a Maxwellian energy distribution accelerated by the sheath before impacting on the probe.

The sputtering ions here have been assumed to be entirely carbon. The deuterium sputtering coefficient is negligible. While the Sn self sputtering coefficient is significant, the quantity of Sn in the SOL will also be negligible. All other trace impurities can also be ignored for similar reasons. The carbon content in MAST is an unknown figure, and here a figure of 1% of  $N_e$  has been used. This is, unfortunately, essentially a free parameter in the model. This is especially true since the carbon coating of the probe tip leads to significant carbon redeposition on the the tin surfaces, implying that whatever the global carbon content at the plasma edge, locally it may be higher.

The estimates obtained for the influx during several shots are shown in figure 4.18. Comparison with the influx obtained from the  $\mathcal{SAB}$ s (figure 4.16) shows that the SRIM estimates are approximately a factor of 5 larger than the  $\mathcal{SAB}$  derived influx. It should be noted, however, that the strong dependence of this data on both  $N_e$  and  $T_e$  lead to large error bars. It can, however, be said that to within an order of magnitude the two methods agree.

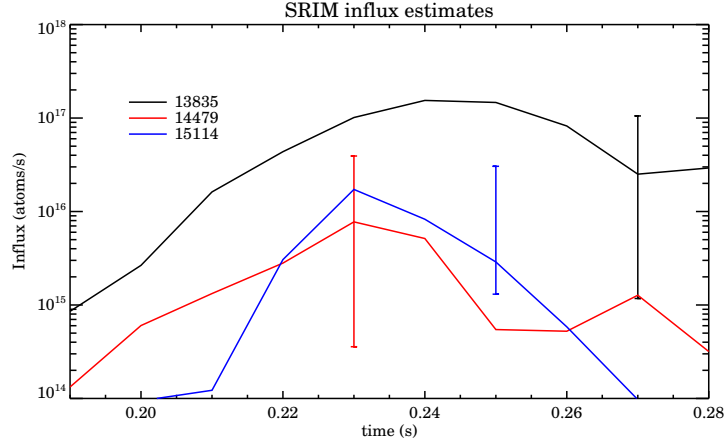


Figure 4.18: Estimates of the influx from the probe tip obtained from SRIM data. Details of the model are described in the text. A typical error bar for the calculation based on the errors in the Thompson scattering measurement of  $T_e$  and  $N_e$  is also displayed.

## 4.5 Transport Analysis

The aim of this experiment was to quantify the fraction of the impurity in the core for a given influx rate. It is therefore necessary to attempt to connect the impurity influx estimates and the core impurity line observations. This is performed using the 1.5D transport code SANCO[78], coupled with the Universal Transport Code (UTC) [79].

The SANCO code solves the particle continuity equation for the population  $N_z$  of impurity ion  $z$  at normalised radius  $\rho$ , time  $t$ :

$$\begin{aligned} \frac{dN_z}{dt}(\rho, t) = & -\nabla\Gamma_z(\rho, t) - S_{z \rightarrow z+1}N_z(\rho, t) + S_{z-1 \rightarrow z}N_{z-1}(\rho, t) \\ & - \alpha_{z \rightarrow z-1}N_z(\rho, t) + \alpha_{z+1 \rightarrow z}N_{z+1}(\rho, t) \end{aligned} \quad (4.3)$$

where the  $S$  and  $\alpha$  terms represent ionisation and recombination to and from adjacent stages, while the  $\Gamma_z$  term is the transport of the impurity in the plasma. The SANCO model reduces the complexity of the core plasma by assuming that all quantities may be treated as flux surface averages, with the geometry of these flux surfaces largely ignored beyond their thickness and volume. The code uses a fluid model of the plasma, in which the flux  $\Gamma_z$  of impurity  $z$  at radius  $\rho$  is:

$$\Gamma_z(\rho, t) = -D(\rho)\nabla N_z(\rho, t) + v(\rho)N_z(\rho, t), \quad (4.4)$$

The coefficients  $D$  and  $v$  are the diffusion and convection (or pinch) velocity terms. By convention, a positive  $v$  is in the direction of the plasma edge. These coefficients can, in theory be calculated from neoclassical theory, however the calculations and experimental estimates seldom agree. They are therefore treated as free parameters which must be determined empirically.

To obtain the ionisation and recombination rates for the plasma  $T_e$  and  $N_e$  must be supplied as a function of radius and time.  $N_H$  and  $T_H$  should also be provided if charge exchange is expected to be significant. On top of this, influx rates for impurity ions and the  $D$  and  $v$  coefficients are also required.

The outputs of SANCO are the impurity ion density  $N_z(\rho, t)$  throughout the shot. UTC, which is a wrapper for SANCO uses this information, combined with information on the line of sight of the spectrometer and the observed line intensity, the  $\mathcal{PEC}$  and the local plasma conditions to determine the goodness of fit. The transport coefficient and the influx estimate can then be altered either manually or through a fitting routine within UTC to obtain a better estimate of the transport coefficients.

This process was carried out for many of the shots in this study, with both In and Sn as the impurities. Figure 4.19 shows the results for 3 shots. Similar coefficients are found for other shots in these experiments. It was also found that the influxes obtained from the  $\mathcal{SAB}$ s could be used as the influxes to the plasma with a multiplier, between 5 and 10 for In and 20 to 30 for Sn.

The line intensities were found to be largely independent of the transport coefficients in the core ( $\rho < 0.7$ ). Indeed, for  $\rho < 0.5$  changing these coefficients has no measurable effect on the modelled emission. This is mainly due to the flat temperature profile of the shots used here (see figure 4.6). The core temperature, which varies between 500 and 700 eV depending on the shot, is in the region where the Cu- and Zn-like stages of In and Sn are long lived (figure 4.20). Since the line of sight of SPRED is a single radial chord, emission from different radial locations cannot be distinguished using just this instrument, therefore the modelled emission is identical for many different sets of transport coefficients.

It is possible to analyse this data further, using bolometry and soft x-ray data in an attempt to pin point the location of the impurity in the plasma. Such an analysis is performed in [80] using SANCO to study the accumulation of the carbon and iron

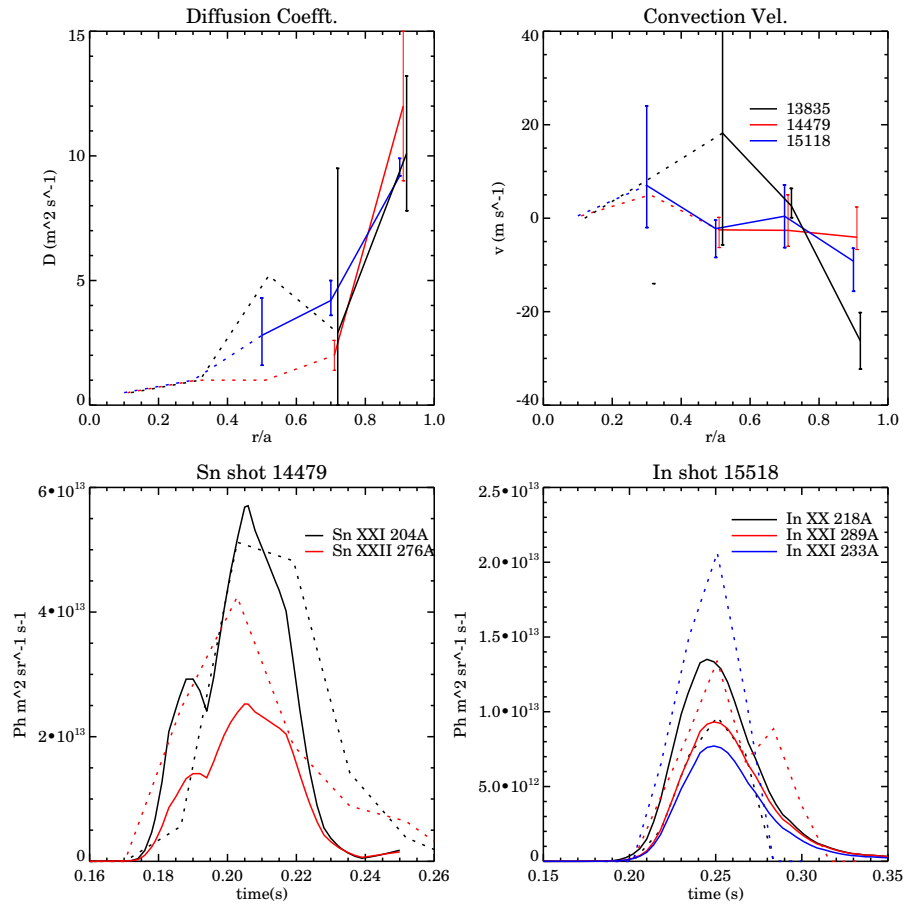


Figure 4.19: (Top) Estimates of the anomalous transport coefficients for three MAST shots. The dotted lines indicate regions of the plasma where the modelled line intensity for the impurities was independent of the transport coefficients. (Bottom) The modelled (solid lines) and observed (dotted lines) for the selected shots.

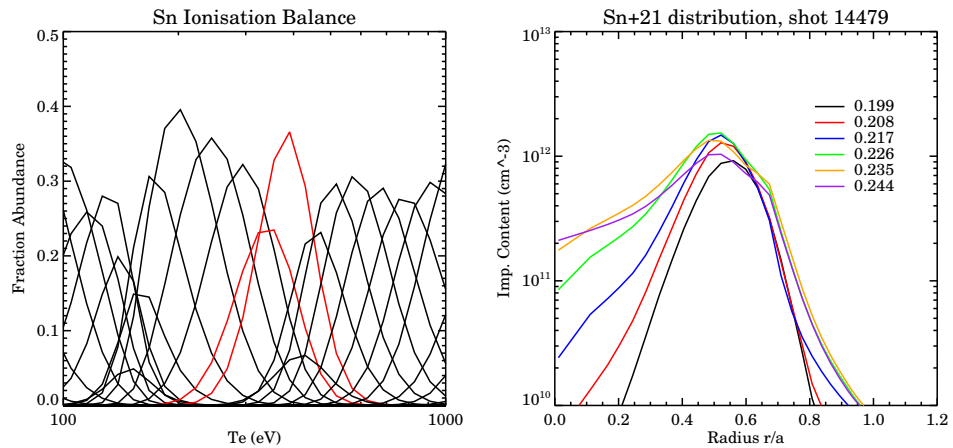


Figure 4.20: (Left) An ionisation balance for Sn as a function of temperature.  $N_e = 3 \times 10^{13} \text{cm}^{-3}$  is assumed. The stages Sn XXI and Sn XXII are highlighted in red. Due to core temperature of the plasma falling in the region where these ions dominate the stages exist throughout the plasma, as shown in the right panel where the Sn XXII distribution for different times is shown.

impurities in the start up phase of MAST plasmas, for example. However, at this point the primary objective of estimating the core impurity content required to provide observable and identifiable line emission, and relating that to the source term, has been achieved as well as possible.

The results of the midplane probe analysis indicate that the impurity can be successfully introduced into MAST plasmas via erosion. It has been possible to use the SOL, as opposed to the main plasma, to cause significant emission of both In and Sn impurity lines. The UTC-SANCO transport code has been used to identify the radial location of the main emission, although for many lines this has not successfully pinned down an exact radius due to the flat temperature profile in the plasma.

The source of the impurity has been modelled using both sputtering yield estimates and spectroscopic methods. These methods agree to within an order of magnitude, however there is a large dependence on the local plasma conditions at the probe tip, which are only loosely known. The influx required by the transport models to recreate the core emission agrees more closely with the magnitude of the sputtering code, although the

influx estimate based on spectroscopic measurements is used with a suitable multiplier to provide a plausible temporal dependence.

## 4.6 Divertor Experiment Results

Following from the successful observation of the core impurity from the midplane, experiments were conducted using a divertor source. The midplane impurity introduction on MAST is a reasonable simulation of the plasma conditions in the ITER divertor, however a divertor source would more realistically represent the geometry of a real plasma-divertor interaction. Therefore the Divertor Impurity Probe (DIP) was designed to introduce an impurity sample between gaps in the divertor tiles. The impurities selected for these experiments were tin and aluminium. Tin was chosen as there was familiarity with it from the midplane experiments. Aluminium was selected due to its light mass and therefore greater sputtering rate in the cooler divertor conditions.

### 4.6.1 Divertor Impurity Probe

As there was no existing divertor impurity source on MAST, nor any divertor probe system, the DIP had to be created from scratch. A manually driven probe system was designed and located on the upper port of MAST at a major radius of 0.975m, which is within the range of radii which the upper outer divertor leg strike point passes over (the outer strike points on MAST generally sweep outwards during the shot due to the changing solenoid field). A photograph of the complete system is shown in figure 4.21.

This system is based upon an old manual probe drive which was utilised on the START tokamak, and has lain dormant since decommissioning of that device. The impurity sample is mounted on the end of a stalk and introduced to the plasma between the gaps between the MAST tiles. Having to fit between the tiles dictates the shape of the sample head - it is a thin cuboid of boron nitride, coated in the impurity to be studied, with a slight slope of  $4^\circ$  on the end to match the slope of the imbricated divertor tiles. The probe is designed to be deployed either flush with the divertor tiles or protruding by up to 7cm. as is shown in figure 4.22. The intention was to have two different modes of operation, with the probe mounted flush with the divertor for prolonged erosion/deposition studies



Figure 4.21: The divertor impurity probe. The left hand picture shows the x-y table and the “cube” in which sample heads can be changed. The right hand picture shows the alignment ports used to check the probe would not collide with the divertor.

and protruding from the edge for impurity transport studies. In practice only the fully protruding position was used for experiments due to concerns about interference with other experimental campaigns.

The probe is entirely manual in operation, and is wound into position before operations, using the viewing ports in the base to check the alignment of the probe with the gaps in the divertor tiles. Any alignment errors can be corrected using the x-y table. As the probe cannot be moved remotely and the machine area is locked during operations, it was not possible to move the probe between shots, although this was not a major concern.

#### 4.6.2 Spectroscopic Setup

The majority of the spectrometers used in these experiments have been previously described in the section for the midplane experiments. The visible spectroscopy was changed to view the new probe location using a port on the bottom of the vessel to give a vertical view of the probe. The layout is shown in figure 4.23.

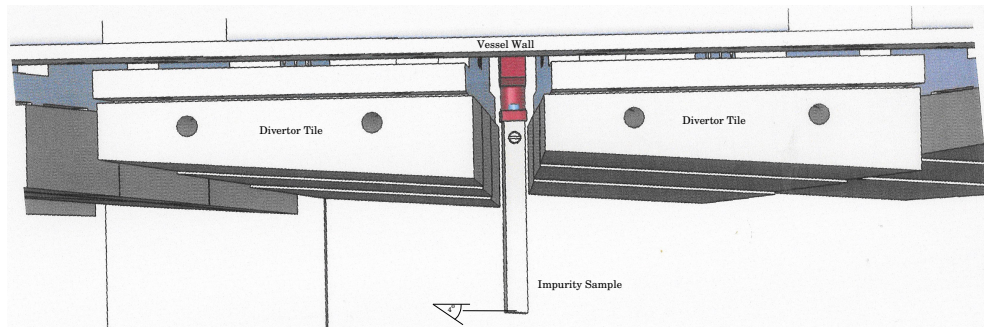


Figure 4.22: The divertor impurity probe protruding from the Mast Imbricated Divertor.

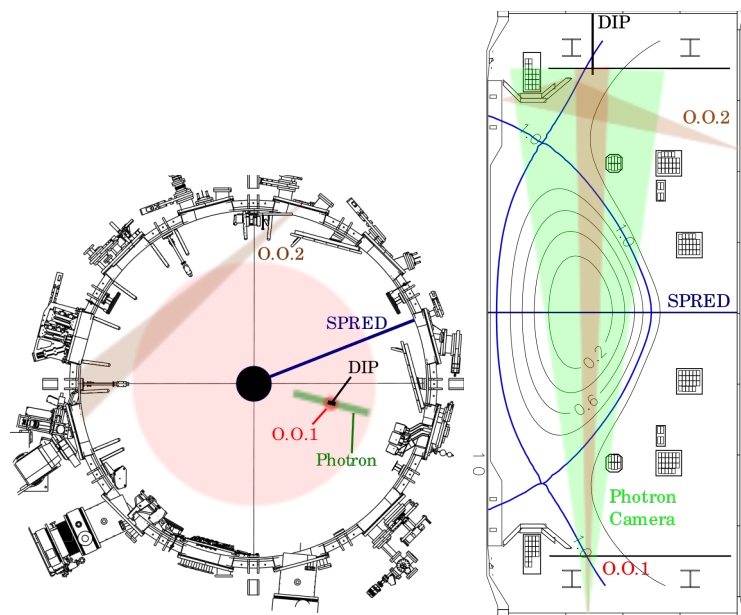


Figure 4.23: The lines of sight of the spectrometers used in the DIP experiments: the two Ocean Optics spectrometers (O.O., red and brown), the Photron camera (green) and SPRED (blue)

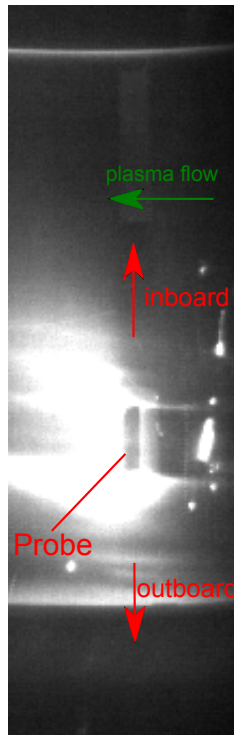


Figure 4.24: The view from the Photron camera, taken during the disruption at 0.317s in shot 18693.

### Photron Camera

The Photron camera is a high speed camera capable of recording an image of  $1024 \times 1024$  at frame rates of up to 5kHz. In normal use at MAST it is used to survey fast phenomena such as ELMs and L-mode filaments due to its high time resolution. For the divertor experiments the camera was mounted vertically looking upwards at the probe. The lens used provided a narrow field of view encompassing the probe tip, and the frame size was reduced to allow increased time resolution. This is shown in figure 4.24

DIVCAM was unavailable during the DIP experiments, due to a combination of poor line of sight and use in other experiments during the same session. The filters that were used in with DIVCAM were reused with the photron to provide a view of the probe in impurity light. The filters used are those listed in table 4.1.

### **SPEX & Ocean Optics Spectrometers**

Two viewing angles were used between the three available spectrometers. SPEX and one of the OO spectrometers used a similar line of sight as the photron camera. A collimator and a  $90^\circ$  prism were used to view vertically upwards, with a viewing diameter of 8cm at the upper divertor.

The other OO spectrometer was deployed looking at the upper divertor leg a short distance from the probe. A view was chosen to encompass the magnetic flux surface which runs through the DIP probe, with the aim of capturing emission from any impurity moving up the leg towards the core.

### **SPRED**

The SPRED spectrometer was unchanged from its use in the midplane experiments. As with the midplane sessions, The 2105g/mm grating was used during Sn experiments. The 450g/mm grating was used with Al to capture emission from a greater spectral range.

### **4.6.3 Plasma Conditions**

These experiments involved a large range of scenarios, which were mostly developed on the fly in an attempt to maximise the power flux to the impurity sample. Both upper single null and double null plasmas were utilised in an attempt to achieve this. The MAST plasma control system is designed to hold the outboard edge of the main plasma in position, not the divertor strike points, which sweep outwards during the shot. It was therefore necessary to “twist” the plasma to hold the strike point stable for any length of time. In the end the strike point would typically dwell within 2cm of the probe for about 100ms on successful shots.

Several scenarios were attempted in these experiments. It was found that it was necessary to have at least one of the neutral beam injectors operating in order to enable the strike point to form at or within the radius at which the probe was mounted (0.975m). It was assumed that single null plasmas would provide the maximum power to the probe tip, however there is a known (and unexplained) phenomenon that USN plasmas on MAST are much less stable and less dense than their DND or LSN counterparts. Therefore mainly

double null plasmas were used here.

#### 4.6.4 DIP Results

Both Sn and Al were successfully and clearly observed on the filtered camera image. An example is shown in figure 4.25, which clearly shows the strong interaction between the probe and the plasma. There was, however, a consistent problem in observing the impurity on the spectrometers. Despite the consistent strong signal present on the cameras there was no matching spectrum recorded on the spectrometers outside of a brief flicker during major disruptions. This lack of signal has proved difficult to explain. Initially, the alignment of the lens was checked, but this was found to be satisfactory. However no other plausible explanation other than misalignment of the lens has appeared: one possibility is that the lack of light was due to the flex of the vessel structure itself during a pulse. The MAST vessel buckles slightly during a pulse due to the forces induced by the currents in the various coils, leading to a bowing of the upper and lower plates of 2cm in the centre. At the location at which the camera and probe are mounted, this leads to a deflection of the vessel base of  $0.57^\circ$ , which is enough to move the viewing spot on the upper divertor, which is 4m away, by 10cm. The diameter of the viewing spot was only 8cm initially, so a 10cm shift results in the line of sight missing the probe by some distance.

Neither Sn nor Al was observed on either SPRED nor the second Ocean Optics spectrometers, making any attempt at transport estimates in the SOL pointless. However it was clear that a large quantity of impurity had been released into the plasma at the divertor. This influx was estimated using the same techniques as for the midplane probe, using the filtered Photron camera data as the spectroscopic measurement.

The camera was calibrated using an integrating sphere to obtain the sensitivity of each of the pixels. Local temperature and density measurements were taken from the Langmuir probe system. The data shown for shot 18426 which has Sn as the impurity, is shown in figure 4.26. There was a strong correlation between the strike point location and the signal observed on the camera, and between the strike point location and the electron density at the probe tip. The electron temperature, however, shows no variation with strike point location. Despite attempts to alter this, it was not possible to raise the  $T_e$  at the upper strike point; it remained  $\approx 4\text{eV}$  throughout these experiments with both Sn and Al.

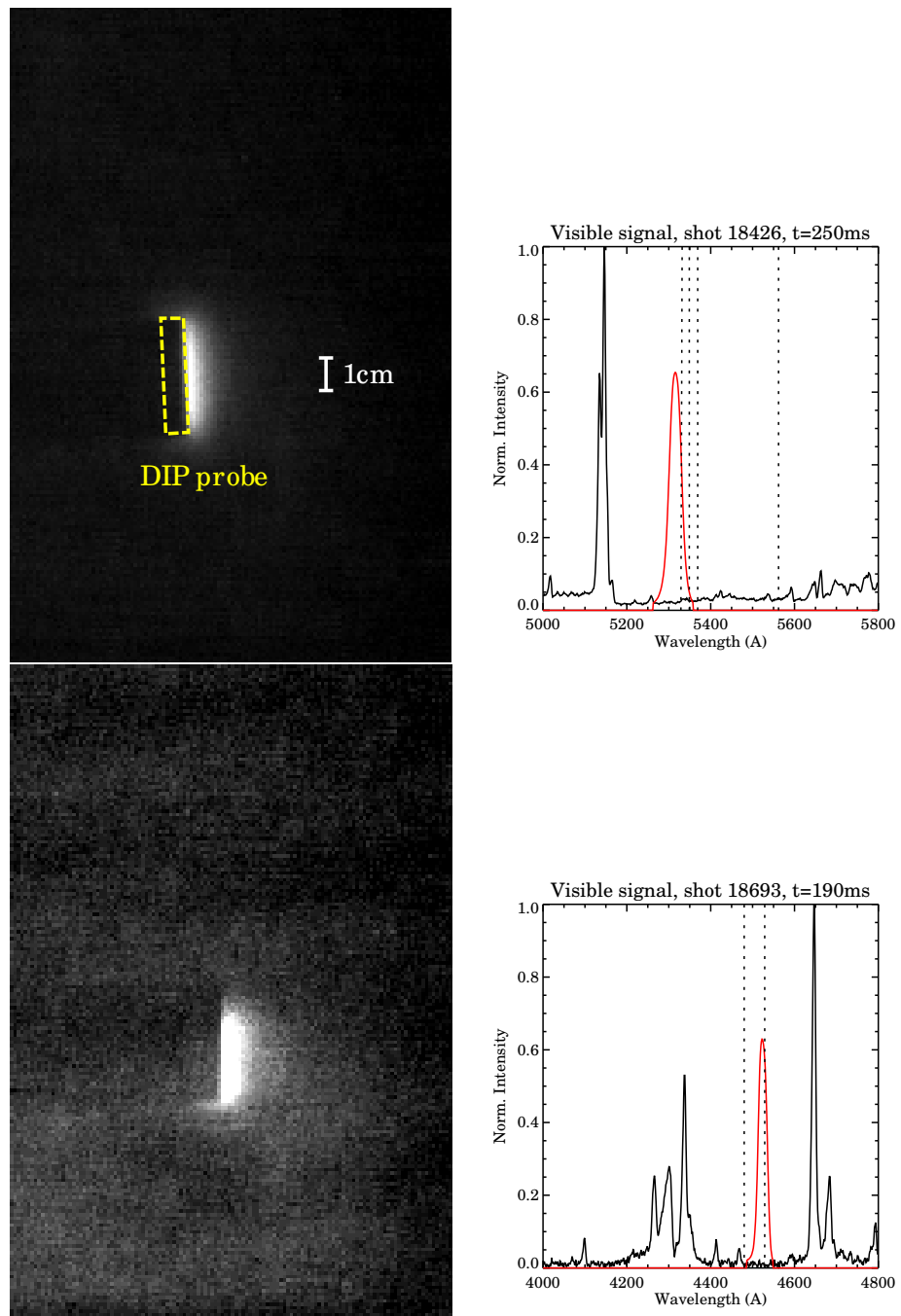


Figure 4.25: (Left) Images from the photron camera with Sn filter from shot 18426 at 250ms, and Al from shot 18693 at 190ms. (Right) The spectra recorded by the ocean optics spectrometer viewing vertically at this time. The red line shows the transmission curve of the filter used with the photron camera. The expected Sn and Al lines are marked with dashed vertical lines.

The final plot in figure 4.26 shows the estimated influx from both the  $\mathcal{SXB}$  and the SRIM models. No agreement is found between the two - indeed, the SRIM model influx was a factor of  $10^6$  smaller than the  $\mathcal{SXB}$  model at most times, and there was no general agreement in form between the two as the SRIM model varied by up to 6 orders of magnitude over the shot. However it should be noted that in the case of Sn, and the temperatures recorded at the probe tip, the energy is significantly below the threshold for physical sputtering ( $\approx 80\text{eV}$ ). It is known that in such energy regions, as described in section 4.1, the model used here is no longer a good representation of the plasma-surface interactions. More advanced models are required, but these are beyond the scope of this work. However, the lower sputtering threshold for lighter elements means that for aluminium the model is once again applicable.

Several problems were encountered during the Al experimental sessions. The photron camera failed to save any data for most shots, although it did display data during the experimental session. The target Langmuir probe arrays also failed to trigger on several shots. Finally the neutral beams were inconsistent, leading to the strike points forming too far outside the probe head for significant interaction. Combined, these factors left only one shot (number 18693) during which all the diagnostics were working and the probe-plasma interaction was significant. However it is noted that there were no Al lines observed on the visible spectrometers during any of the shots, excluding the disruption phase of shots 18685 and 18688 (figure 4.27 shows the camera image from shot 18685). For the one successful Al shot, shot 18693, the conditions at the probe are shown in figure 4.28. The flux of carbon atoms to the probe tip, on which the SRIM model is based, is calculated as  $\Gamma = N_e A'_{probe} v_{ion} C$  where:  $A'_{probe}$  is the effective area of the probe - the projected area normal to the magnetic field ( $\approx 27\text{cm}^2$ );  $v_{ion}$  is taken from the model described in section 4.1 and  $C$  is the fractional content of carbon in the plasma (in practice a free constant).

Using this simple model, and noting that the sputtering threshold problems encountered for the Sn influx do not affect the Al calculations, a strong correlation is found between the two calculation methods. Comparison of the two results gives a result of  $1.03 \times 10^{-3}$  for the constant C, implying that this is the carbon concentration. This value is significantly less than might be expected - typically it is assumed that carbon concen-

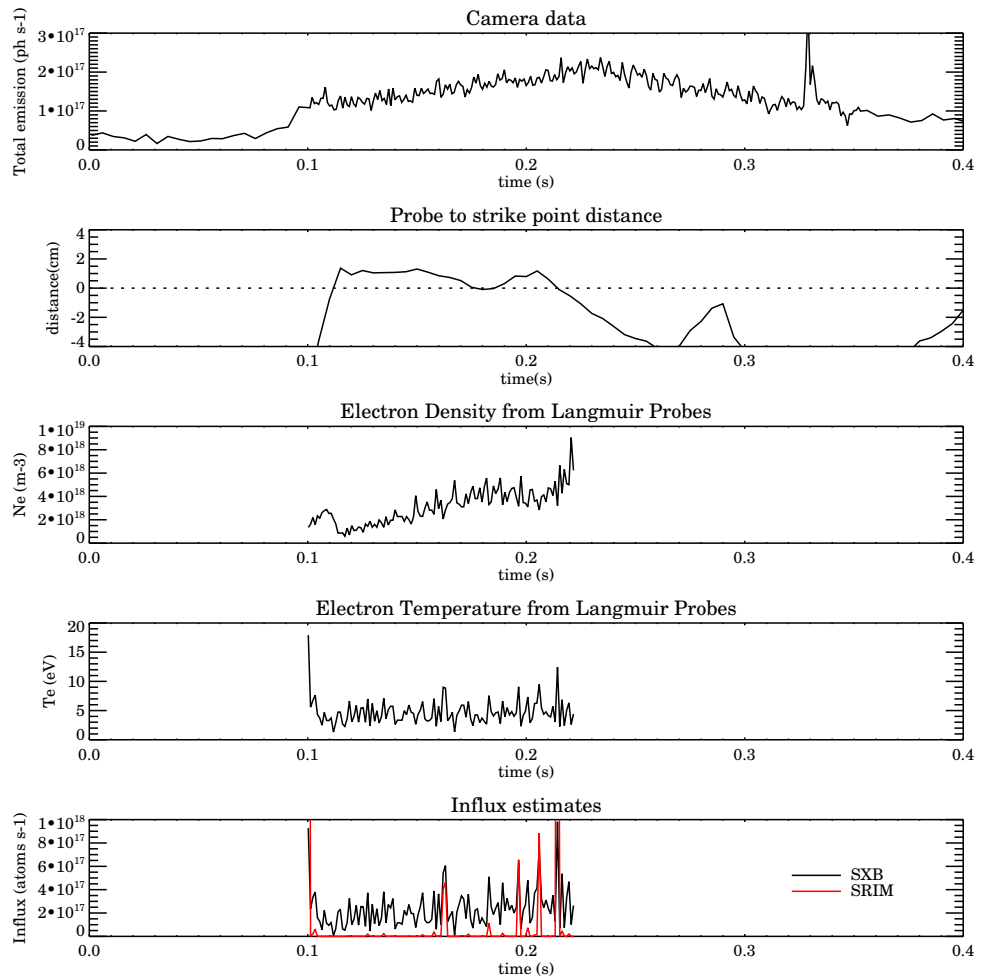


Figure 4.26: The conditions at the sample and the influx rates measured using  $\mathcal{SXB}$  and SRIM techniques for MAST shot 18426.

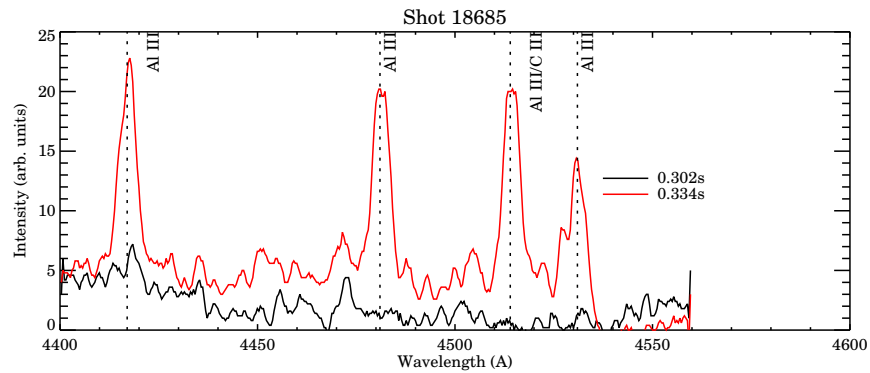


Figure 4.27: The Al spectrum lines recorded on SPEX-A before and during the disruption of shot 18685.

trations at the divertor are of the order of 1% of the electron density. The reason for this discrepancy is unknown.

## 4.7 Conclusions

Mechanisms for introducing non-gaseous heavy species impurities to the MAST plasma at both the outboard midplane and the divertor plates have been implemented on MAST. In the former case this involved a new head on the existing reciprocating probe system, in the latter a whole new probe system was designed, constructed and deployed.

For the midplane experiments, both tin and indium impurities were successfully observed in the core using soft x-ray spectroscopy and at the source using visible spectroscopy. It was found that the influx obtained from both spectroscopic and physical sputtering models agreed to within an order of magnitude. The dependence on  $T_e$  and  $N_e$  at the probe tip is significant, and the errors in these measurements can easily dwarf any differences between the models.

Impurity transport calculations were carried out in the core with the UTC-SANCO code to try to match the calculated influx and the observed impurity lines. The physical sputtering model was found to give better results for the magnitude of the influx.

Divertor impurity probe experiments failed to observe any impurity in the core or upstream in the divertor leg. Instead, use was made of Langmuir probe and filtered

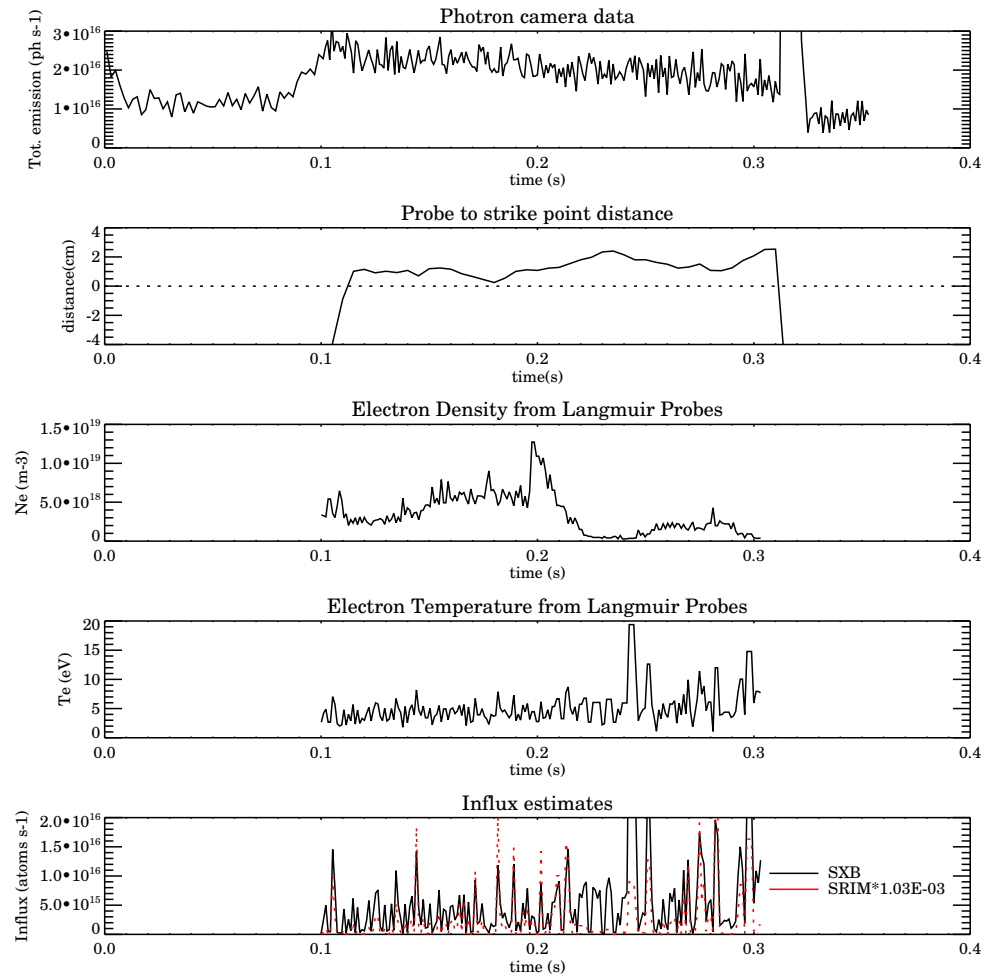


Figure 4.28: The conditions at the sample and the influx rates measured using the  $SXB$  and SRIM techniques for MAST shot 18693.

camera data to estimate the influx both spectroscopically and through physical sputtering models for Sn and Al. The low temperatures in the SOL results in a break-down of the model used for physical sputtering of Sn, however for Al the model works well. Good qualitative agreement is found between the two different methods for influx estimates of Al. Quantitative agreement depends on the carbon concentration assumed in the plasma edge: a value of 0.1% gives the best agreement. This is an order of magnitude smaller than typical impurity densities assumed for MAST in other experiments.

## Chapter 5

# Charge Exchange and Heavy Species

In addition to the emission arising from ion-electron collisions, (see chapters 2 and 3) the emission from ion-ion collisions in plasmas can and is routinely used to measure profiles of the ion temperature,  $T_i$  and the plasma rotation velocity,  $v$ [81]. In some systems it is also possible to measure the plasma impurity density profile, given suitably accurate calibration of the system[82].

In early laboratory fusion plasmas, there was no need to rely on the ion-ion collisions for these measurements - direct observation of impurity lines in the visible region could be made. As technology has advanced and plasma temperatures have increased, the light impurities found in plasmas are now usually fully ionised in all but the very edge regions of the plasma, and therefore there is little or no line emission from the core to use for these measurements. Heavier elements, which may not be fully ionised in the core, are undesirable in large quantities in the plasma and active efforts are made to keep them out of the plasma: ideally this results in the signal being too weak to usefully observe. In any case, the strongest of these transitions moves from being in the visible region, where spectroscopy is simple, into the vacuum ultra violet or soft x-ray regions, where spectroscopy is significantly more challenging.

Fortunately, a side effect of the use of neutral beam injection (NBI) heating, which is present on nearly all modern tokamaks, is that the charge exchange process is enhanced in

such a way as to allow observation of these properties in the visible region. Such diagnostic techniques are termed Charge Exchange Recombination Spectroscopy (CXRS), and a brief description of this technique as applied to hydrogen - carbon charge exchange is given in section 5.1.

For reactors such as ITER, all the impurities except tungsten will be fully ionised in the core of the plasma. It remains desirable to be able to quantify the impurity content of the plasma. This can once again be achieved through a charge exchange measurement for the light elements, and recent work[83] shows that this should be achievable for all ions, though with signal to noise ratios dropping in some cases to as low as  $\approx 5$ .

In many current fusion devices, and planned for ITER, the spectra recorded by CXRS diagnostics are matched by plasma modelling to obtain the contribution to the spectra from the background, with the remaining radiation attributed to CX. Other tokamaks make use of background subtraction, where the NBI is notched (briefly turned off and back on), and the spectrum recorded during this period is subtracted from the CXRS spectrum to obtain the residual spectrum from CX. This method is complimentary to background modelling, as both suffer from some difficulties: accurate modelling of the background is difficult, and the plasma conditions may change significantly while the beam is turned off, therefore the comparison is not between like plasmas.

Lines of sight which avoid the beam itself can be used for this background subtraction, or as a measure of the background radiation to aid the modelling of this background. Such background measurements are also used to obtain the effective average ionisation state,  $Z_{eff}$  of the plasma. The spectral regions chosen for these background measurements are deliberately chosen to be free from strong line emission.

In a plasma such as the ITER one, there will be a significant tungsten content. While the absolute concentration may be small (estimates are for a concentration of  $\approx 1 \times 10^{-5}$  of  $N_e$ ), the number of different ionisation stages, and the many electrons present in these stages, are expected to produce a large number of lines.

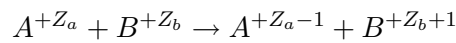
Due to the low concentrations and the many different ionisation stages of tungsten present, it is unlikely that any CXRS observations or calculations could be usefully performed on the tungsten lines. It is, however possible that the tungsten lines could interfere with the other measurements being made. Therefore it is useful to be able to estimate the

magnitude of such effects and the wavelength that any such features would appear at.

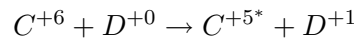
As well as being a consideration for ITER, such issues arise as a growing number of tokamaks which have or will implement tungsten plasma facing components. The case of the proposed tungsten divertor upgrade for MAST will be examined in section 5.4.1.

## 5.1 The Charge Exchange Reaction

The charge exchange reaction takes place when during a collision between two atoms/ions an electron is transferred from one ion to the other:

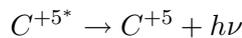


In the context of a fusion plasma, the reaction between neutral hydrogen or (more commonly) deuterium atoms and a completely ionised impurity ion in the core is often used as a plasma diagnostic. Carbon in particular is commonly used, due to its use in the plasma facing components of many tokamaks, giving rise to the reaction:



The neutral deuterium in the reaction comes from two sources: firstly, there is the small fraction of neutral deuterium which exists at any given time in the plasma (*thermal* or *passive* CX) and secondly there are the high energy neutral deuterium ions which come from the neutral beam injectors (*beam* or *active* CX).

The excited impurity ion then decays from this excited state, emitting one or more photons as it does so:



To lowest order, the energy levels depend only on the  $n$  quantum number, and the separation of energy levels between two  $n$  shells  $n$  and  $n'$  is given by

$$\Delta E_{nn'} = R_{\infty} Z^2 \left( \frac{1}{n^2} - \frac{1}{n'^2} \right)$$

where  $R_{\infty}$  is the Rydberg constant.

For carbon, this results in the  $n$ -resolved wavelengths of their emission lying as shown in figure 5.1. The  $n=8 \rightarrow 7$  transition emits in the visible region and is free from interference

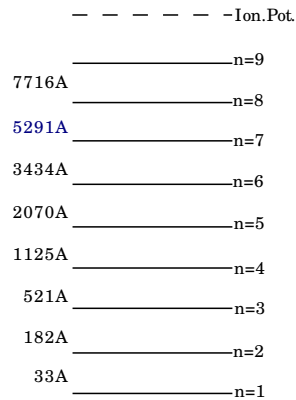


Figure 5.1: The wavelength of light emitted in  $n$  to  $n'$  transitions in  $C^{+5}$ . The  $n=8 \rightarrow 7$  transition is customarily used for charge exchange measurements as it lies in the visible region and is free from interference from other impurity lines.

from spectral lines emitted by other elements typically present in fusion plasmas and can therefore be easily observed. The high  $n$ -shell has the added virtue of ensuring that capture into this high level is almost exclusively from energetic beam neutrals: the thermal charge exchange contribution to this line emission is therefore neglected in this section, as is electron impact excitation/spontaneous emission.

Due to the fine structure splitting of different  $l$  shells, within each  $n$  shell there are different energy levels and therefore the  $n = 8 \rightarrow 7$  transition is in fact not one line but many. In practice, the splitting is so small in energy that it can be ignored for measurements such as ion temperatures. It is, however, still necessary to have  $nl$ -selective capture cross sections even if one is not going to directly use the  $nl$ -selective data, as which  $l$  shell the electron is captured into will effect the allowed radiative transitions and therefore the emissivity of the spectral lines.

It is not possible to directly measure  $nl$ -selective cross sections, though experiments can be used to verify them. Therefore theoretical calculations of the capture cross sections are required.

## 5.2 Charge Exchange Cross Sections

### 5.2.1 Calculation for Light Elements

There are many different models used to obtain charge exchange cross sections. In part, the proliferation of codes is due to the difficulty in measuring these experimentally: in such circumstances the only check of the quality of a method is the agreement of calculations with other theoretical models. Models relevant to the energies of fusion NBI systems include: molecular orbital (MO[84]) and atomic orbital (AO[85]) multichannel close coupling expansions; classical trajectory Monte Carlo (CTMC[86]); and the unitarized distorted-wave approximation (UDWA[87]). Each of these has different energy ranges of validity[81]. The AO approach is valid from 1 to 60keV/amu, with the MO method favoured below 25keV/amu. The CTMC method is valid above 50keV/amu. The UDWA method overlaps all these energy ranges.

Due to the varying energy validities of the differing techniques, a full dataset for CX cross sections is not usually obtained from just one method. For example the ADAS database, which stores total  $n$  and  $nl$  selective cross sections as ADF01 files, contains 5 different combinations of methods for the  $H^0 + C^{+6}$  reaction alone. The datasets which will be utilised in section 5.2.2 have been chosen for the combination of the quality and breadth of  $n$  shell coverage. For the ground state hydrogen donor,  $H(n=1)$ , AO data from [85, 88] have been used below 50keV/amu, while UDWA data from [89] has been used above this, for  $Be^{+4}$ ,  $C^{+6}$ ,  $O^{+8}$  and  $Ne^{+10}$ . Data from CTMC calculations [90] was available but only for a reduced number of  $n$ -shells. For the excited donor,  $H(n=2)$ , the CTMC calculations of [91] are used for  $He^{+2}$ ,  $Be^{+4}$ ,  $C^{+6}$  and  $Ne^{+10}$ .

Recently, cross section have been produced for the  $H(n=1)$  collision with  $Ar^{+16}$ ,  $Ar^{+17}$  and  $Ar^{+18}$  using an improved version of the CTMC method[92]. This data improves on both the quality of low energy calculations and  $n$  shell coverage of the earlier work for argon. Experiments have been conducted on ASDEX-U to validate this data, and produced good results [93]. This has motivated this investigation into heavier species. Before describing this, it is worth noting some features of the CX cross sections.

It has been noted in [90] that the principal  $n$  shell into which capture occurs, known as the critical  $n$ ,  $n_{crit}$ , is dependent on the recombining ion charge as  $n_{crit} \approx z_r^{(3/4)}$ . At

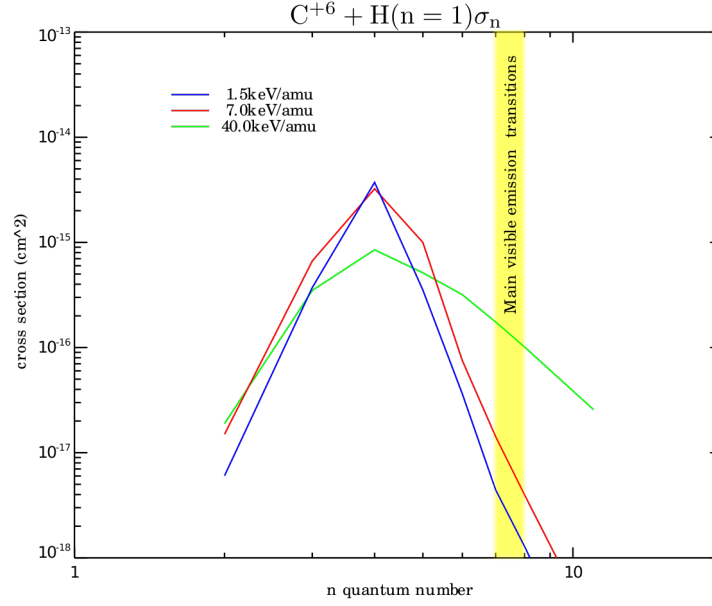


Figure 5.2: Behaviour of  $n$ -shell selective charge exchange cross sections for the  $H(n=1)$  donor.  $\sigma_n$  maximises at  $n_{crit} \approx z_r^{(3/4)}$ . Visible emission is from  $n \approx 2n_{crit}$ , in this case the  $n = 8 \rightarrow 7$  transition. The data shown are for  $C^{+6}$ . Similar effects are observed for other ions.

higher energies, this peaking becomes less pronounced, as shown in figure 5.2. These shells into which the majority of capture occur are known as the *dominant shells*.

The lines giving rise to visible CXRS emission are from  $n$  shells with  $n \approx 2n_{crit}$ . This means that for capture from the  $H(n=1)$  donor, the observed emission is due to capture into *subdominant* shells. The dominant  $n$  shells for capture from the excited  $H(n=2)$  donor are shells where  $n \approx 2n_{crit}$ , therefore directly into the shells responsible for visible radiation. The ratio of beam atoms in the ground state to those in the excited state (determined by collisions with the plasma ions), is such that for light ions the  $H(n=1)$  emission is still dominant despite the greater cross sections for the  $H(n=2)$  capture, although the  $n = 2$  effects cannot be ignored.

The  $l$  shell cross section behaviour is shown in figure 5.3. At values of  $l > n_{crit}$  there is an exponential fall off of the cross section  $\sigma_{nl}$ . For  $l < n_{crit}$  the cross section increases as  $\sigma_{nl} \propto (2l + 1)$

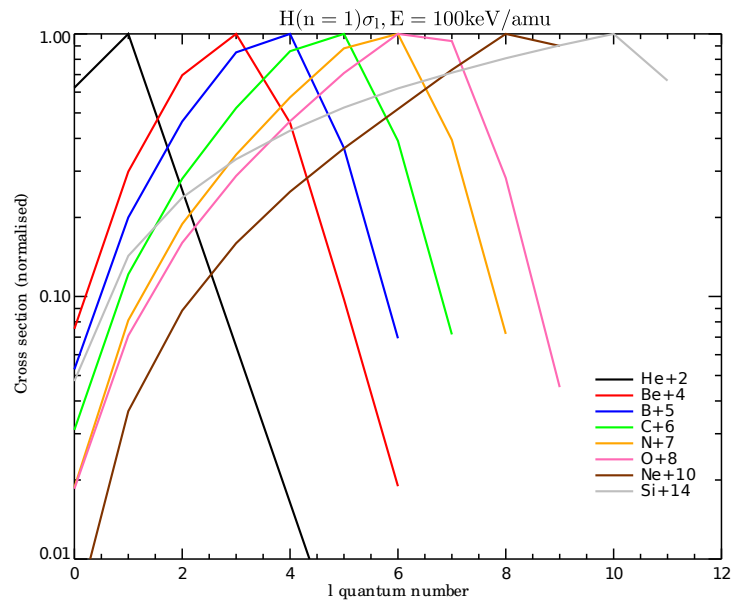


Figure 5.3: Behaviour of  $l$ -shell selective charge exchange cross sections for the  $H(n=1)$  donor.  $\sigma_{nl}$  maximises at  $l_{crit} \approx n_{crit} \approx z^{3/4}$ . Data is taken from the highest  $n$  shell for which  $nl$  cross sections are tabulated in the ADAS ADF01 file for that element. The  $n$  shell for each ion can be determined by the maximum  $l$  plotted plus 1 (e.g.  $n = 12$  for Si).

### 5.2.2 Estimation for Heavy Elements

While the work by Errea et al[92] has extended the database of ions for which cross sections exist, it does not approach the heavy species which will appear in ITER, for example, the tungsten ions. Therefore a scaling law system has been devised to extrapolate from the best data currently available and to apply it to heavier elements.

It was found for the light elements that the contribution of the H(n=1) donor strongly dominated that of the H(n=2) donor. It is not a priori certain that this is true for the heavier elements, therefore both the H(n=1) and H(n=2) donors will be treated independently using this method.

#### Total Cross Section, $\sigma_{tot}$

Examination of the total CX cross section data for both H(n=1) and H(n=2) reveals some trends. The cross sections are shown for a variety of elements on the left hand side of figure 5.4 as a function of the energy of the donor ions. Having observed the previously described  $z^{(3/4)}$  dependence of  $n_{crit}$ , it was decided to investigate if similar  $z$  scalings could be used for other attributes of the charge exchange cross sections. A simple scaling law has been applied to obtain a scaled total cross section  $\sigma_{tot}^*$  and energy  $E^*$ , with form  $\sigma_{tot}^* = \sigma_{tot} z_r^{-\alpha}$ ,  $E^* = E z_r^{-\beta}$ , where  $\alpha$  and  $\beta$  are constants and  $z_r$  is the recombining ion charge. This is shown in the right hand side of figure 5.4. This scaling is found to bring the total cross sections onto a universal curve, which has been named the universal total cross section,  $\overline{\sigma_{tot}}$ . The values of  $\alpha$ ,  $\beta$  and the individual points on  $\overline{\sigma_{tot}}$  have been chosen to minimise the standard deviation of the real data from the universal curve.

Given the universal cross section and the scaling parameters, it becomes possible to reverse the process and estimate the total charge exchange cross section for any ion simply using its charge. Thus the total cross section for capture to tungsten can be estimated.

It is noted here that, as the scaling depends only on the charge of the recombining ion, there will be no difference between cross sections for (for example)  $W^{+16}$  and  $Sn^{+16}$ . This is justified by the fact that the critical  $n$  shell for capture is a high one, and therefore the donor atom and transferring electron are screened from the structure of the atom with which they are recombining, and see only the residual charge of the recombining ion,  $z_r$ .

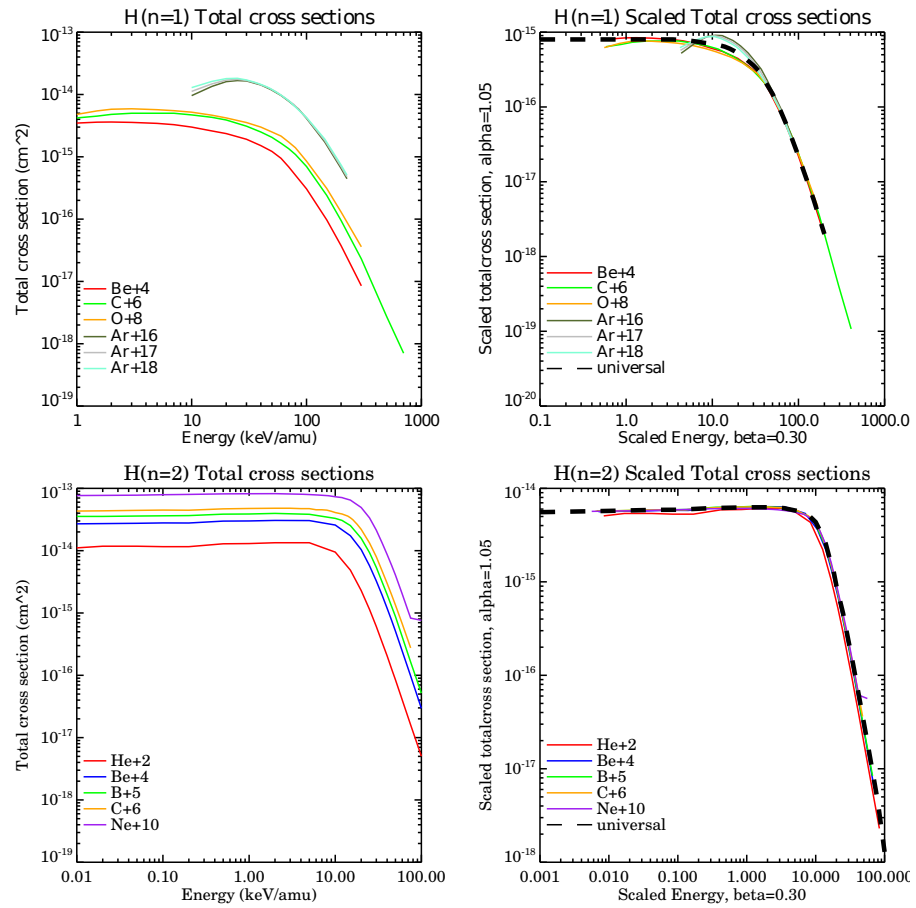


Figure 5.4: *Left*: the total cross sections for the H<sup>0</sup> CX cross sections for n=1 and n=2 shell donor hydrogen atoms. *Right*: The scaled total cross section, with the specified values of scaling parameters  $\alpha$  and  $\beta$

It is also noted that the extrapolation of data from fully stripped argon (or even neon for the H(n=2) donor) to highly ionised tungsten is a large one, and likely to lead to significant error. However it provides the best estimate that is currently possible of the likely charge exchange cross sections for heavy elements. It is tempting to ignore the potential effect heavy species charge exchange may have on any plasma diagnostics until good quality data exists. However such calculations are unlikely to be forthcoming in the near future, if at all, therefore it is better to attempt to examine the process rather than ignore it. This work therefore represents an attempt to obtain the best possible estimate of the effect of this process given the available data. It is expected that these estimates will be improved upon in the future when charge exchange calculations for heavier species are produced.

### 5.2.3 The $n$ -shell Resolved Cross Section, $\sigma_n$

The total capture cross sections in the previous section lend themselves well to a scaling law approximation. However, to estimate emission from plasma, greater resolution is required - it is important to know which shell the electron is captured into. Ideally, the  $nl$  shell into which the capture takes place will be resolved. Dealing with this issue in a sequential manner, the  $n$  shell selective data will be looked at first, with attendant cross section  $\sigma_n$ .

The same data sets are used as for the  $\sigma_{tot}$  calculations. The  $\sigma_n$  are interpolated onto the same scaled energy grid as was used for  $\sigma_{tot}$ . Both the  $n$  quantum number and the  $\sigma_n$  are then scaled by energy dependent factors  $\gamma(E^*)$  and  $\delta(E^*)$ , as  $\sigma_n^* = \sigma_n z_r^{-\delta(E^*)}$ , and  $n^* = n z_r^{-\gamma(E^*)}$ . Least squares fitting is then used to obtain the optimal values of  $\gamma$  and  $\delta$  and a universal scaled  $\bar{\sigma}_n$  for that energy, as shown in figure 5.5. Given the expected scaling  $n_{crit} \propto z_r^{(3/4)}$ , it is reassuring to note that these results give values of  $\gamma$  of close to 0.75.

The system is found to work well for high values of the beam energy, but breaks down at low energies ( $\leq 5\text{keV/amu}$ ) as the cross sections become less consistent (figure 5.6). This breakdown at low energy is, however, not relevant to the high energies of NBI injectors in fusion plasmas. Consider the ITER diagnostic NBI system, which has  $E=100\text{keV/amu}$ , and the tungsten impurity in ITER. As shown in figure 5.4,  $\beta = 0.3$  for the H(n=1)

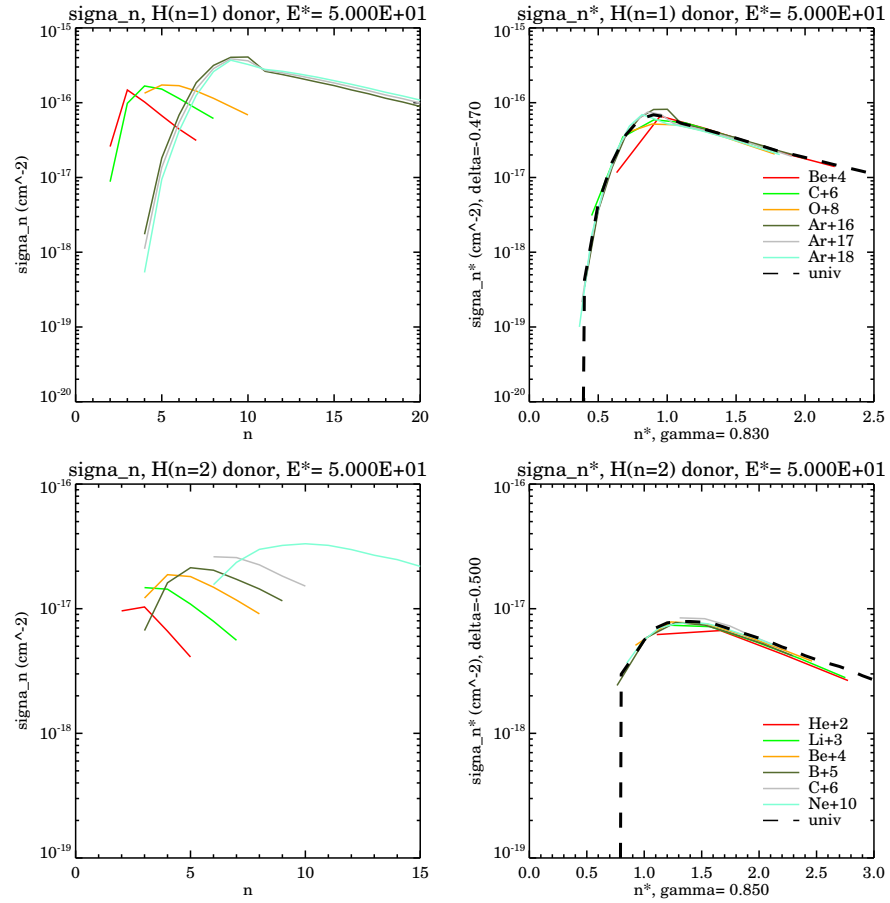


Figure 5.5: *left*: The cross sections  $\sigma_n$  for the charge exchange reaction for the H(n=1) and H(n=2) donor, at scaled energy  $E^* = E/z_r^\beta = 50\text{keV}/\text{amu}$ . *right*: The scaled cross sections  $\sigma_n^* = \sigma_n/z_r^\delta$  as a function of the scaled  $n^* = n/z_r^\gamma$ , and the universal curve derived from this.

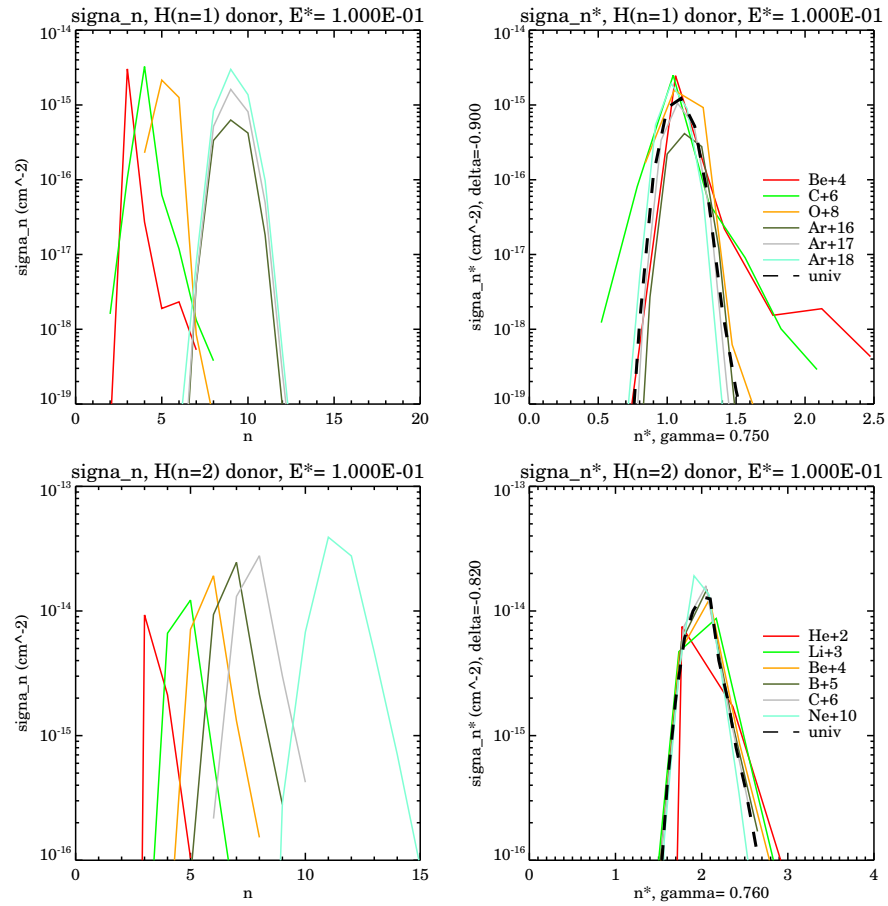


Figure 5.6: As for figure 5.5, but for a lower scaled energy  $E^* = E/z_r^\beta = 0.1\text{keV}/\text{amu}$ . The scaling law techniques work less well in this region, however these energies are not common for NBI systems on fusion devices.

donor, therefore even for fully stripped tungsten,  $E^* = 27.5\text{keV}/\text{amu}$ , which is well within the region where these fits work well.

As with the total cross sections, the tabulation of the  $n$ -selective cross sections allows extraction and generation of  $n$  resolved data for any arbitrary species. When extracting the data, the  $\sigma_n$  will reach an upper  $n$  shell for which data is tabulated, however capture into higher  $n$  shells is still significant, as shown in figure 5.2. Within the ADAS ADF01 data format, an extrapolation parameter is used to represent the capture to high  $n$  shells for a given beam energy. Within ADAS this is known as the  $\alpha$  parameter, though to avoid confusion with the  $\alpha$  scaling parameter it will be denoted by  $\kappa$  here. The high  $n$  cross sections are given by:

$$\sigma_n(E_i) = \left(\frac{n_{max}}{n}\right)^{\kappa(E_i)} \sigma_{n_{max}}(E_i) \quad (5.1)$$

here  $n_{max}$  is the last shell for which cross section data is tabulated.

For low energies,  $\kappa$  is estimated from the  $\sigma_n$  for the last two cross sections for which there are cross sections tabulated. For high energies, this scheme leads to unphysically small values of  $\kappa$ : when  $\kappa \leq 1$  the integral to infinity of cross sections becomes infinite. Comparison of different  $\sigma_n$  from the original data with that obtained from the methods in this chapter for the same ions have led to a minimum value of 2.0 being assigned to  $\kappa$ .

Extracted  $\sigma_n$  are re-normalised against the total cross sections,  $\sigma_{tot}$  for the energy in question, by summing the  $\sigma_n$  and including the sum to infinity from the  $\kappa$  parameter, to provide self consistent data.

#### 5.2.4 The $l$ -shell Resolved Cross Section, $\sigma_l$

Attempts were made to obtain  $l$  shell resolved capture cross sections, however it was found that this could not be satisfactorily achieved using scaling laws of the form of those used for  $\sigma_{tot}$  and  $\sigma_n$ . It was also discovered that there was insufficient  $l$ -shell resolved data for the  $n = 2$  donor ions to achieve a satisfactory fit which could be extrapolated. In future a return to re-examine these cross sections would be desirable, to investigate for a more complex form of scaling should it exist. In the current work, due to the applicability of the bundle- $n$  model for heavy species, this was not deemed to be crucial for obtaining emission estimates, and therefore further optimisation has not been done. An example of

some of the  $l$  resolved cross sections obtained is shown in figure 5.7.

### 5.3 The Bundle- $n$ Model

The ultimate goal of these cross section estimates is to obtain an estimate of the emission from the CX process. In order to achieve this, it is necessary to model both the capture and the cascade to extract a prediction for the CX line emission from the cross sections.

As outlined in the previous section, it was not possible to obtain reliable estimates of the  $nl$  resolved cross section. As also outlined in section 2.2.3, it will therefore be assumed that the population of each  $l$  shell is statistical due to collisional redistribution among  $n$  shells. This is implemented in ADAS as the ADAS316 code, as outlined in figure 5.8.

Within this model, several processes initiating the population of each different  $n$  shell are considered: electron impact excitation from the ground, free-electron recombination, thermal CX and beam CX. An existing code, which calculates the populations as a total of these processes has been modified to be called four different times, with the input parameters modified each time to obtain the effect of switching off all but one process in each case. From this it is possible to isolate the contribution of each process to the excited populations, and therefore to obtain the emission due to CX. Exact calculation for each process is carried out for a set of representative  $n$  shells, typically stretching to  $n \approx 20z_1^{(3/4)}$ . Populations of intermediate shells are obtained by interpolation from results of these representative shells.

Cross sections for ion and electron impact excitation are obtained from several different formulae. For electron impact excitation, impact parameter calculations are used for transitions with small  $\Delta n$ , typically  $\Delta n \leq 4$ , while for the remaining transitions Van Regemorter[59] or Lodge-Percival-Richards (LPR) [94] cross sections may be used (the choice is at the user's discretion). For impact with thermal hydrogen ions, the impact parameter is again used for small  $\Delta n$ , while for large  $\Delta n$  the Vainshtein[95] or, again, LPR formulae can be used. For the impurity ions, the Vainshtein or LPR approaches are preferred for all transitions. For beam CX reactions, the data from the ADF01 files is used for cross sections. A record of the populations obtained from these calculations is then tabulated at a reference set of conditions, and stored as an ADF26 file.

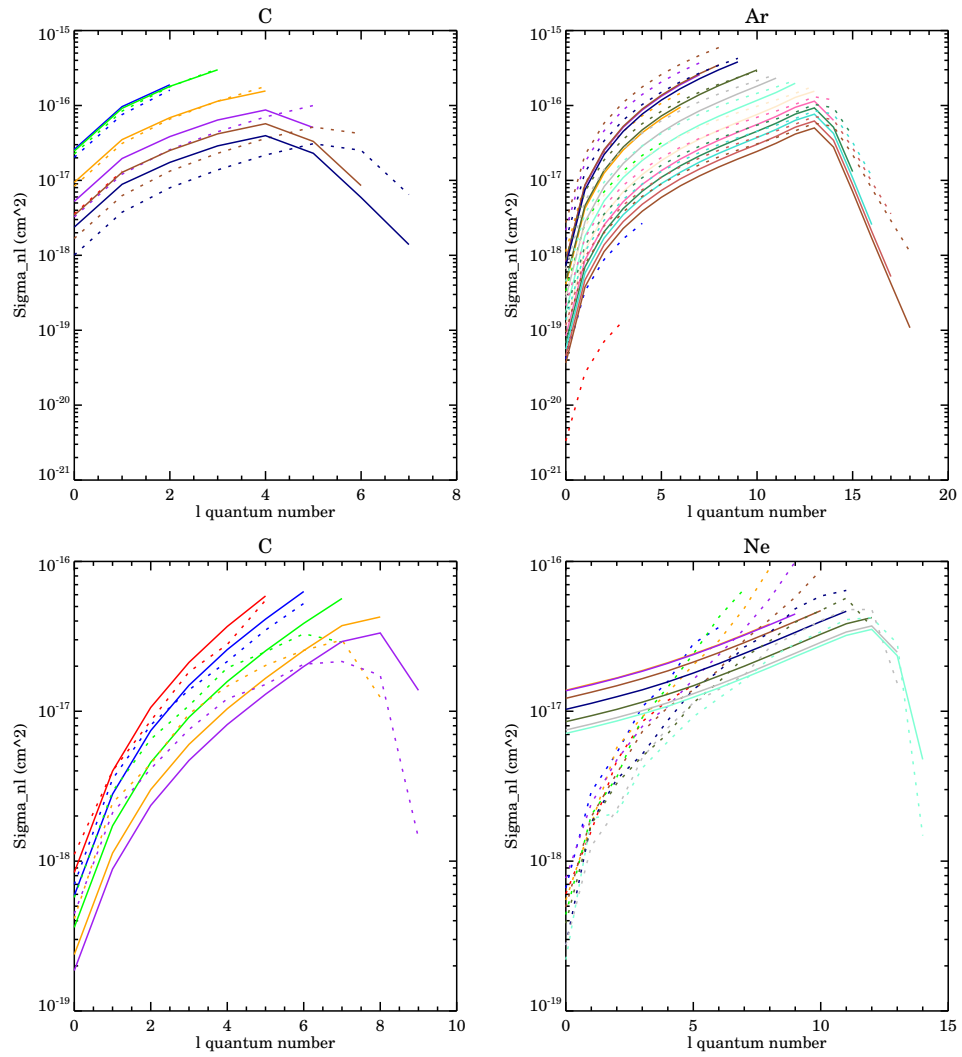


Figure 5.7: The cross sections  $\sigma_{nl}$  for the charge exchange reaction for (top) the H( $n=1$ ) and (bottom) H( $n=2$ ) donor, at energy  $E=50\text{keV/amu}$ . The solid line is obtained from the scalings in this chapter, the dotted line is data from ADAS.

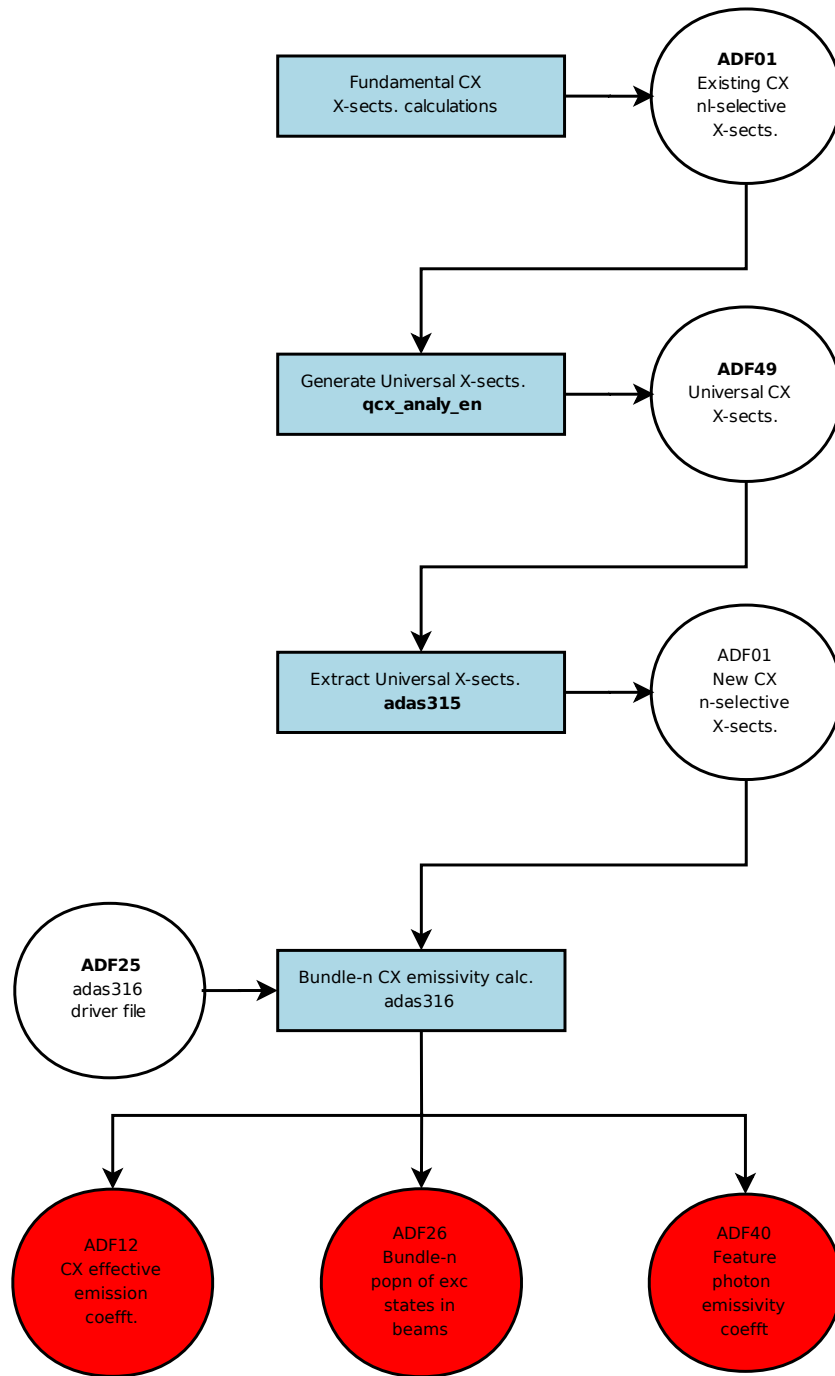


Figure 5.8: Structure of codes for obtaining CX emission estimates.

Energies and wavelengths are obtained from the hydrogenic relations:

$$E = \frac{R_{\infty} z^2}{\nu^2} \quad (5.2)$$

and

$$\lambda = \left[ R_{\infty} z^2 \left( \frac{1}{\nu_1^2} - \frac{1}{\nu_2^2} \right) \right]^{-1} \quad (5.3)$$

where  $\nu$  is the effective principal quantum number, that is  $n - \delta$  where  $\delta$  is the quantum defect, to account for non-hydrogenic nature of the ions. The rate coefficient for each radiative transition is then obtained by calculation of the Einstein A coefficients for the  $n - n'$  transitions and multiplying by the initial shell populations.

Typically, this process is then repeated for a range of different parameters: beam neutral energy,  $E$ , ion temperature,  $T_i$ , ion density,  $N_i$ , average plasma ion charge,  $Z_{eff}$  and magnetic field,  $B$ . Due to the large amount of space required to store six-dimensional arrays for this data, it is stored instead as the exact value at a reference set of conditions, and then as six one dimensional arrays adjusting one parameter in each. This is the ADF12 data format.

From this ADF12 file it is then possible to extract the spectrum of the radiation from charge exchange, as will be done in the following section. It is also useful to be able to immediately observe the spectrum, for this reason a single energy, single density ADF40 file is produced, which contains the  $\mathcal{FPEC}$  for the CX interaction with the ion.

## 5.4 Emission from Tungsten

### 5.4.1 MAST Upgrade

The aim of this work is to estimate the charge exchange cross sections for a device with heavy species in it. The MAST tokamak will be upgraded over the next decade with significant increases in ECRH heating and a total of 4 Positive Ion Neutral Beam Injector (PINI) NBI devices[96]. Also of significance is the proposed change from a carbon divertor to a tungsten coated one. This could lead to a significant presence of tungsten in the plasma.

The impurity content of MAST Upgrade plasmas is an unknown. It is assumed that to operate successfully, the core  $Z_{eff} \approx 1.7$  or less. This has been simulated using a combina-

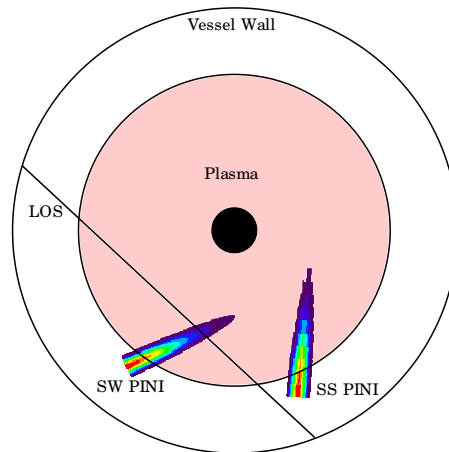


Figure 5.9: The line of sight used for the MAST Upgrade predictions in figure 5.12, and the neutral beams as included in MAST. The plasma conditions have been taken from TRANSP simulations, while the beam profile and attenuation are taken from the MAST beam code[98], implementing ADAS beam stopping coefficients.

tion of carbon (1%), tungsten (0.001%) and He (1%) when obtaining the Bremsstrahlung estimates in this section.

Since the exact design for this upgrade is still under consideration there is no definitive layout on which to model diagnostic lines of sight. Similarly, the location and direction in which the 4 proposed NBIs will be pointing have not yet been settled on. Therefore, while the plasma conditions have been simulated using the TRANSP[97] code, the existing neutral beam locations and profiles have been used in estimating the charge exchange emission. The line of sight selected crosses one of the neutral beams in the core of the plasma and avoids the other, as shown in figure 5.9. Predicted MAST Upgrade core temperatures from the TRANSP data are  $T_e \approx 2.4\text{keV}$ ,  $N_e \approx 3.3 \times 10^{13}\text{cm}^{-3}$

#### 5.4.2 Emission Estimates

An example of the emission calculated for a single stage,  $\text{W}^{+40}$ , is shown in figure 5.10. The reference temperature, 2376eV, is chosen as this is the core temperature obtained from the MAST-Upgrade simulations. In the final plot in this figure the fraction of the beam in the ground and excited states is used to modify the relative emissivity from the

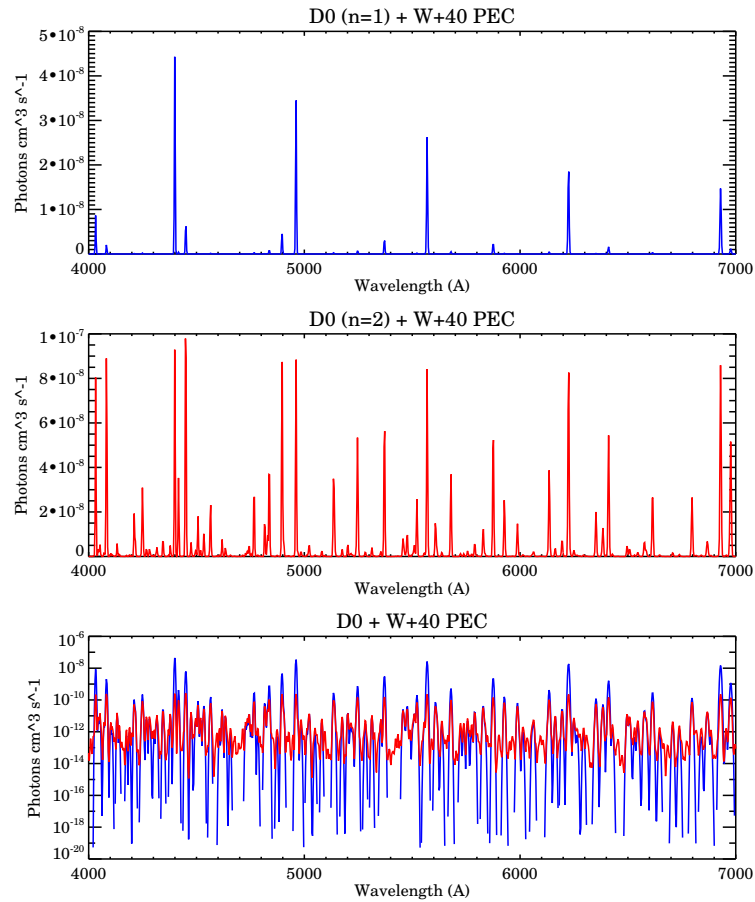


Figure 5.10: The predicted emission from one ionisation stage of tungsten at  $T_e \approx 2.4\text{keV}$ . In the final graph the spectra have been multiplied by the fraction of the beam deuterium in the ground and excited states.

two processes, and the  $n = 1$  contribution is found to dominate. The fraction of the beam deuterium in each state is determined by collisions between beam ions (initially all in the ground state) and plasma ions, and it is found that approximately 0.2% of the beam neutrals are in the  $n=2$  state in the plasma core.

It is clear that in a real plasma there will be more than one ionisation state of tungsten present at any given time. Applying a steady state ionisation balance to the tungsten for the same plasma conditions (figure 5.11) already produces a mass of spectral lines covering the entire of the visible spectrum. .

The goal of the next stage is to estimate the effect of the lines in a simulation of a

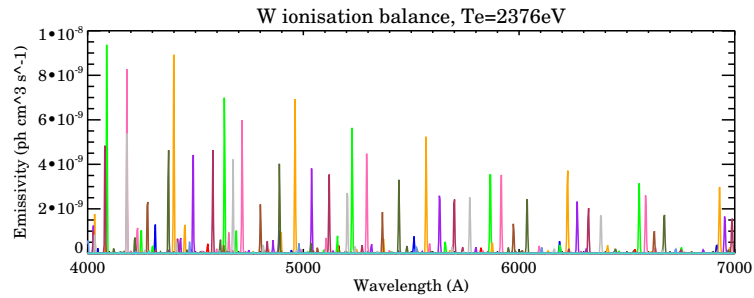


Figure 5.11: The predicted emission from a steady state ionisation balance of tungsten at  $T_e \approx 2.4\text{keV}$ . The different colours indicate different stages of tungsten.

realistic line of sight across the plasma. The case shown here is for the line of sight across the plasma shown in figure 5.9. The line of sight integrated results across the plasma are shown in figure 5.12. It is found that the CX and the Bremsstrahlung emission are of the same order of magnitude, and therefore there is likely to be significant interference in measurements of such background quantities.

## 5.5 Application to ITER and Conclusions

The same model was then applied to ITER plasmas, using a vertical line of sight crossing one of the neutral beams. It is found (figure 5.13) for a vertical line of sight that the ratio of the CX to the Bremsstrahlung emission is similar, with peaks arising to about 15-20% of the Bremsstrahlung levels.

Given the typically narrow spectral regions which are used for measurements of  $Z_{eff}$  (the MAST system uses a 1nm bandpass filter[99]) care must be taken to select an appropriate region of the plasma with no such emission. This in turn may prove difficult given the sheer number of lines present, and the change in wavelengths depending on the area of the plasma viewed (and therefore the underlying impurity ionisation balance).

While the results of this section are of modest accuracy due to the extrapolations which these data are based upon, it is likely that these will mostly affect the intensities of the lines present, not their wavelengths. Therefore the potential problems that these lines pose are likely to be real effects, and they should be taken into account in future

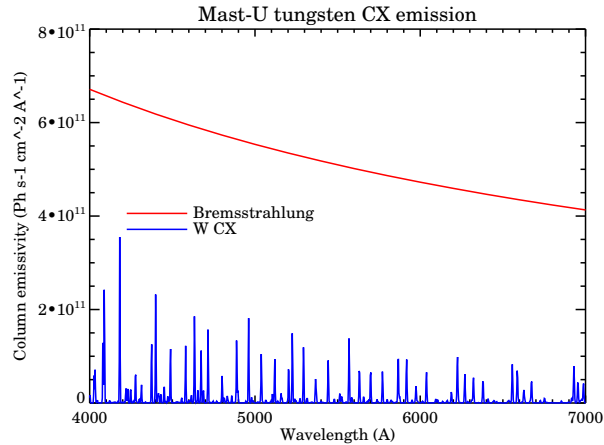


Figure 5.12: The predicted line integrated tungsten charge exchange and Bremsstrahlung emission for a chord on MAST-U. While the Bremsstrahlung level is greater than the charge exchange estimates, the CX emission is of the same order of magnitude, and therefore it is likely that it will interfere with background measurements of  $Z_{eff}$

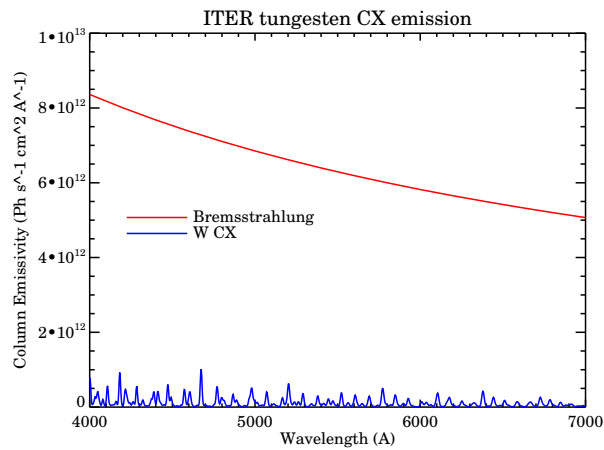


Figure 5.13: The predicted line integrated tungsten charge exchange and Bremsstrahlung emission for a vertical chord on ITER viewing the diagnostic neutral beam through the core of the plasma. Again, as for MAST Upgrade the CX emission is found to be a significant fraction of the background.

diagnostic design.

## Chapter 6

# Conclusions

This work has extended the baseline atomic datasets for fusion plasmas, and applied this extension to experiments in MAST and simulations of ITER conditions. It is now possible to rapidly produce useful baseline atomic data for any element, enabling analysis of any impurity found in or introduced to fusion plasmas. The modular nature of the model allows higher quality data to be used where it exists. Comparison with selected data from more precise atomic calculations show that emissivities produced by the two methods differ by at most 50%, which is acceptable for most applications.

Use has been made of the present techniques to provide data for predictions of ITER plasma conditions. These predictions have made use of the new superstaging methodology to allow 2D fluid plasma simulations to be run with tungsten as a trace impurity. It has been found that in a 1D test model the superstaged and non-superstaged model agree very well. In 2D models there are some discrepancies between different bundling schemes but these are small enough to be attributed to numerical issues within the fluid code, not the superstage model itself.

Analysis of an experiment involving the introduction of heavy impurities by erosion into the plasma edge has also been carried out on MAST, with a view to application as an erosion diagnostic for ITER. Results have proved inconclusive as no estimate of transport in the SOL was possible. However, when introduced at the midplane separatrix, impurity was observed in the core and estimates of the erosion rate from both spectroscopic and physical sputtering calculations agree to within an order of magnitude.

Finally, a method for estimating the charge exchange emission from an arbitrary heavy species has been developed. This model shows that the charge exchange contribution to the background is going to be both non-negligible and have strong wavelength dependence, and therefore may interfere with measurements of background radiation or very weak charge exchange lines.

## 6.1 Future Work

### 6.1.1 Further Experimental Work

Further experimental work can be carried out to investigate the validity of the erosion diagnostic, which is only in a very preliminary stage. Ideally an embedded tile would be placed in an existing tokamak with a dedicated spectrometer to observe when it is exposed and whether released impurities can be detected. However this will still suffer from the constraint that current devices have at least an order of magnitude lower erosion rates than will be encountered on ITER, therefore such an experiment on a small localised scale is highly likely to produce a null result.

Embedding relatively high concentration layers of impurity in a large range of tiles, and viewing with a filtered 2D camera, would probably be a better solution. Once the impurity is exposed, this camera image could provide an influx estimate and then core impurity spectrometer data would allow estimation of a penetration factor. This method would also probably have more relevance to the proposed application compared with inserting a probe into a plasma.

In a similar vein, if multiple impurities are to be used to localise the erosion spectroscopically, it will be important to check that they can be distinguished experimentally<sup>1</sup>, and also to examine similarities or differences in their transport behaviour. To this end, experiments on ASDEX-Upgrade have been planned for laser blow off from a mixed Sn/In target.

---

<sup>1</sup>The theoretical ‘marching’ of transition arrays from the present baseline model indicates this distinguishability

### 6.1.2 Heavy Species Baseline Development

The extensions to the Cowan code have now been pushed to the limits of what can usefully be achieved with this system. There is little to gain from further extension of the baseline excitation calculations: this data is now ready for exploitation during impurity experiments with any arbitrary species.

Further work on the implementation of the superstaging technique is desirable. In particular, a scheme for altering the superstaging partition across the plasma radius 'on the fly' - that is dynamically, during a simulation may prove very useful: it would enable aggressive bundling of high ionisation at the edge and lower ones in the core, enabling the computational benefits of superstaging to be realised but reducing the impact on the accuracy of the simulation.

Further improvements to the GCR coefficient calculations are also possible. Problems with the Case B calculation of the dielectronic recombination have been highlighted in chapter 2. Ideally, given the superior model of case B, it would be possible to improve this longstanding issue. There is, however, currently work underway within ADAS and with collaborators to improve many of these coefficients to produce a case C set of collisional radiative coefficients. One method currently being developed is to benchmark the Burgess-Bethe General Program (BBGP[58]) against results of a reduced size zero-density DR calculations from Autostructure[33]. This will allow the coefficients for BBGP for an ion to be calculated more accurately, and then the results extended to finite densities using BBGP.

The ionisation coefficients,  $S_{CD}$  are also under improvement. Recent work [100] using configuration averaged distorted wave calculations of electron impact ionisation rates promises a comprehensive improvement to ionisation rates for all elements. This has been completed for several elements including argon, krypton, xenon and tungsten. They are currently under assessment for implementation in ADAS.

Considerable work is in progress involving collaborators with the ADAS project to prepare the most precise collisional data for the individual strong line emitter ions for several elements, as identified by the natural partition. This work is targeting both selected individual ions and entire isoelectronic sequences. The embedding of variable precision

(GCR and CR) data in the superstage model is enabled in the codes described in this thesis.

### 6.1.3 Charge Exchange

The charge exchange method described in chapter 5 is clearly incomplete. Two main improvements to the model can be considered. One is the extension of the scaling laws to incorporate the  $l$ -shell selective cross section. The  $l$  dependence appears to be systematic, but there is insufficient data to obtain extrapolatable forms. Further examination with more a sophisticated scaling law may also prove more successful than the methods in this work.

The second possible improvement is to calculate the charge exchange cross sections for heavier species and to incorporate this data into the scaling laws, to more accurately present the scaling to high  $Z$ . This would ideally be done with close coupled AO fiducials; this is, however, considerably easier to state than to achieve, as argon is beyond the limit of close coupled models at this point in time. Extension of the CTMC calculations to higher  $Z$  is under discussion and the early stages of implementation, and is therefore the most likely source of cross sections for heavy species. There are, to the best of the author's knowledge, no cross sections for elements beyond argon at this time.

As well as extending the work, it is important to test the validity of the scaling law concept as much as is possible. One method proposed for this is a set of experiments using noble gas impurities introduced into the edge plasmas by gas puffing, and then observing both their charge exchange and passive emission spectra. Transport calculations similar to those in chapter 4 could then be used with this data to estimate the validity of the complete heavy species model, including an estimate of the validity of the charge exchange cross sections. Also of interest will be the point at which individual lines from charge exchange becomes unobservable, and whether emission features can be identified in their place for heavier elements. It has been proposed to attempt this by starting experiments on ASDEX-Upgrade and JET, making use of the higher temperatures available in the latter to study higher ionisation stages of heavier elements, and to progressively move from neon, to argon, to krypton and then xenon, if the emission can still be resolved. A proposal for such an experiment has been accepted for both ASDEX-U and JET and

awaits scheduling.

## 6.2 Contributions of the Author and Publication Plans

It is the nature of scientific research, especially in the fusion field, that many people contribute to any one project. Therefore at this point I will attempt to define my exact contribution to the work described in this thesis.

The idea for the heavy species promotion rules method was first suggested by others. I made refinements to this technique. The idea of optimising the configuration sets using line radiated power calculations is my own, as is its full implementation.

The superstaging technique was also a pre-existing idea within ADAS, although it has only come to full fruition during this work. I was involved in the latter developments of this, and was responsible for providing the data to be used in EDGE-2D. This also involved an investigation of the appropriate bundling schemes as well as the generation and then superstaging of relevant data.

The experimental conditions used during the experiments on MAST were my selection, although the nature of a tokamak experiment such as MAST means that many people were involved on the day, in particular the session leaders who set up the plasmas and made adjustments where necessary during the sessions. The original ideas and design of the DIP probe and the RP head were my own, while the actual details of design, manufacture and construction were performed in conjunction with others, in particular Graeme Wearing for the DIP probe. The analysis of the experiments were entirely my own work, including porting the UTC code to run for MAST plasmas, although the UTC code itself was developed elsewhere.

The idea for the charge exchange extrapolation technique was taken from conversations with Hugh Summers, whilst I worked out the details of the scheme and implemented the process. The bundle-n model used for generating tungsten spectra was developed from pre-existing ADAS codes primarily by others but with my involvement, although its use to produce the data in chapter 5 was again my work. The TRANSP data for MAST-Upgrade was generated by Rob Akers.

There are two existing publications associated with this work, [64] and [101]. Likely

future publications will include publication of the heavy species techniques in chapter 3 as a laboratory report, with results from applications of the technique appearing in open literature. The charge exchange technique is also expected to form the basis of another laboratory report. Possibilities for publishing in open literature are being considered for the emission simulations.

# Bibliography

- [1] D. J. Campbell and the JET Team. *J. Nucl. Mat.*, 241-243:379, 1997.
- [2] G. Federici et al. *Fusion Engineering and Design*, 39-40:445, 1998.
- [3] A. Makhankov et.al. *Proc. 20 Symposium on Fusion Technology, Marseilles*, page 267, 1998.
- [4] M. Merola et al. *J. Nucl. Mat.*, 283-287:1068, 1999.
- [5] S. Suckewer and R. J. Hawryluk. Plasma edge cooling during RF heating. *Phys. Rev. Lett.*, 40:1649, 1978.
- [6] Alcator C-Mod homepage. <http://www.psfc.mit.edu/research/alcator/>.
- [7] ASDEX-Upgrade homepage. [http://www.ipp.mpg.de/eng/for/projekte/asdex/for\\_proj\\_asdex.h](http://www.ipp.mpg.de/eng/for/projekte/asdex/for_proj_asdex.h)
- [8] R. Neu et al. *Nucl. Fus.*, 45:209, 2005.
- [9] T. Pütterich. *Investigations on Spectroscopic Diagnostics of High-Z Elements in Fusion Plasmas*. PhD thesis, Universität Augsburg, 2005.
- [10] A. Kallenbach et al. *Plasma Physics and Controlled Fusion*, 47:B207, 2005.
- [11] V. Philipps et al. *Plasma Physics and Controlled Fusion*, 42:B293, 2000.
- [12] J. Pamèla et al. *J. Nucl. Mat.*, 363-365:1, 2007.
- [13] F. Wagner et al. *Proceedings of the Thirteenth Conference on Plasma Physics and Controlled Nuclear Fusion Research (IAEA, Vienna)*, 1:277, 1982.
- [14] M. Cox and The MAST Team. *Fusion Engineering and Design*, 46:397, 1999.

- [15] A. Pironti and M. Walker. *Control Systems Magazine, IEEE*, 25:24, 2005.
- [16] J. Wesson. *Tokamaks*. Clarendon Press, Oxford, 1997.
- [17] Y-K. M. Peng and D. J. Stricker. *Nuc. Fus.*, 26:769, 1986.
- [18] Summary of the ITER Design Report. [http://www.iter.org/pdfs/Summary\\_FDR.pdf](http://www.iter.org/pdfs/Summary_FDR.pdf).
- [19] H. Bruhns, R. Brendel, G. Raupp, and J. Steiger. *Nuc. Fus.*, 27:2178, 1987.
- [20] P. K. Browning, B. Browning, and J. Clegg et al. *Controlled Fusion and Plasma Physics (Proc. 16th Eur. Conf, Venice, 1989)*, 13B, part II:787, 1989.
- [21] A. Sykes et al. *Nuc. Fus.*, 32:694, 1992.
- [22] M. Gryaznevich et al. *Phys. Rev. Lett.*, 80:3972, 1998.
- [23] NSTX Team and C. Neumeyer. *Fusion Technology*, 29(2):469, 2001.
- [24] B. Lloyd et al. *Plasma Physics and Controlled Fusion*, 46:B477, 2004.
- [25] A. Loarte et al. *Nuc. Fus.*, 38(3):331, 1998.
- [26] E. T. Cheng et al. *Fusion Engineering and Design*, 38:219, 1998.
- [27] Y-K. M. Peng et al. *Plasma Physics and Controlled Fusion*, 47:B263, 2005.
- [28] H. P. Summers. Atomic Data and Analysis Structure. <http://www.adas.ac.uk>.
- [29] NIST Atomic Spectra Database. <http://physics.nist.gov/PhysRefData/ASD/>.
- [30] E. Schrödinger. *Annalen der Physik*, 8:734, 1926.
- [31] H. N. Russell and F. A. Saunders. *Astrophys. Journal*, 61:38, 1925.
- [32] R. D. Cowan. *The Theory of Atomic Structure and Spectra*. University of California Press, 1981.
- [33] N.R. Badnell. *J. Phys. B: At. Mol. Opt. Phys.*, 19:3827, 1986.
- [34] A. Bar-Shalom, M. Klapisch, and J. Oreg. *Journal of Quantitative Spectroscopy and Radiative Transfer*, 71:169, 2001.

- [35] M. F. Gu. The Flexible Atomic Code. In *Atomic Process in Plasmas: 14th APS Topical Conference on Atomic Process in Plasmas*, volume 730, page 127. AIP, 2004.
- [36] I. P. Grant, J. B. McKenzie, P. H. Norrington, D. F. Mayers, and N. C. Pyper. *Computer Physics Communications*, 21(2):207, 1980.
- [37] D. R. Hartree. *Proc. Cambridge Phil. Soc.*, 24:111, 1928.
- [38] V. Fock. *Z. Physik*, 61:126, 1930.
- [39] V. Fock. *Z. Physik*, 62:795, 1930.
- [40] V. Fock and M. J. Petrashen. *Physik. Z. Sowjetunion*, 6:368, 1934.
- [41] P. Bryans. *On the Spectral Emission of Non-Maxwellian Plasmas*. PhD thesis, University of Strathclyde, 2005.
- [42] J. J. Thomson. *Phil. Mag.*, 6:449, 1912.
- [43] D. V. Fursa and I. Bray. *J. Phys. B: At. Mol. Opt. Phys.*, 30:757, 1997.
- [44] M. S. Pindzola et al. *J. Phys. B: At. Mol. Opt. Phys.*, 40:R39, 2007.
- [45] P. G. Burke and K. A. Berrington. Institute of Physics Publishing, Bristol, 1993.
- [46] D. C. Griffin, N. R. Badnell, and M. S. Pindzola. *J. Phys. B: At. Mol. Opt. Phys.*, 31:3713–3727, 1998.
- [47] P. H. Norrington and I. P. Grant. *J. Phys. B: At. Mol. Opt. Phys.*, 20:4869–4881, 1987.
- [48] K. Bartschat, E. T. Hudson, M. P. Scott, P. G. Burke, and V. M. Burke. *J. Phys. B: At. Mol. Opt. Phys.*, 29:115–123, 1996.
- [49] N. R. Badnell, K. A. Berrington, H. P. Summers, M. G. O'Mullane, A. D. Whiteford, and C. P. Ballance. *J. Phys. B: At. Mol. Opt. Phys.*, 37:4589–4601, 2004.
- [50] C. P. Ballance and D. C. Griffin. *J. Phys. B: At. Mol. Opt. Phys.*, 39(17):3617–3628, 2006.

- [51] A. D. Whiteford M. C. Witthoef and N. R. Badnell. *J. Phys. B: At. Mol. Opt. Phys.*, 40:2969, 2007.
- [52] D. J. Griffiths. *Introduction to Quantum Mechanics*. Prentice Hall, New Jersey, 1995.
- [53] H. P. Summers et al. *Plasma Physics and Controlled Fusion*, 48:263, 2006.
- [54] W. Lotz. *Z. Phys.*, 216:241, 1968.
- [55] A. Burgess and M. C. Chidichimo. *Mon. Not. R. astr. Soc.*, 203:1269, 1983.
- [56] A. Burgess, H. P. Summers, D. M. Cochrane, and R. W. P. McWhirter. *Mon. Not. R. Astr. Soc.*, 179:275, 1977.
- [57] A. Burgess. *Astr. J.*, 141:1588, 1965.
- [58] N.R. Badnell, M. G. O'Mullane, H. P. Summers, and et al. *Astronomy and Astrophysics*, 406:1151, 2003.
- [59] H. Van Regemorter. *Mon. Not. Roy. Astr. Soc.*, 121:213, 1960.
- [60] The Iron Project. <http://www.usm.uni-muenchen.de/people/ip/iron-project.html>.
- [61] A. D. Whiteford. *On the spectral emission of impurity species for diagnostic application to magnetically confined fusion plasmas*. PhD thesis, University of Strathclyde, 2004.
- [62] B. J. Brahm's. *Computational studies in tokamak equilibrium and transport*. PhD thesis, Rijksuniversiteit Utrecht, 1986.
- [63] Simonini et al. *Contrib. Plasma Phys.*, 34(2-3):368, 1994.
- [64] L. Lauro-Taroni, G. Corrigan, A. Foster, M. O'Mullane, V. Parail, J. Strachan, H. P. Summers, A. Whiteford, and S. Wiesen. Proceedings of the 35th EPS Conference on Plasma Physics, 2008.
- [65] ITER physics basis. *Nuc. Fus.*, page 2137, 1999.
- [66] K. Asmussen et al. *Nuc. Fus.*, 38(7):967, 1998.

- [67] P. Galli et al. *Nuc. Fus.*, 38(9):1355, 1998.
- [68] P. C. Stangeby. *The Plasma Boundary of Magnetic Fusion Devices*, chapter 2. IOP Publishing, Bristol, 2000.
- [69] D. Bohm. *The Characteristics of Electrical Discharges in Magnetic Fields*, chapter 3. McGraw-Hill, New York, 1949.
- [70] I. Langmuir. *Science*, 58:290, 1923.
- [71] R. J. Fonck, A. T. Ramsey, and R. V. Yelle. *Applied Optics*, 21(12):2115, 1982.
- [72] J. Sugar, V. Kaufman, D. H. Baik, Y. Kim, and W. L. Rowan. *J. Opt. Soc. Am. B*, 8(9):1795, 1991.
- [73] J. B. Green and R. A. Loring. *Phys. Rev.*, 30(5):574, 1927.
- [74] G. V. Deverall, K. W. Meissner, and G. J. Zissis. *Phys. Rev.*, 91:297, 1953.
- [75] K. H. Behringer. *J. Nucl. Mat.*, 145-147:145, 1987.
- [76] J. F. Ziegler, J. P. Biersack, and M. D. Ziegler. The Stopping Range of Ions in Matter. <http://www.srim.org>.
- [77] R. Scannell, M. J. Walsh, P. G. Carolan, N. J. Conway, A. C. Darke, M. R. Dunstan, D. Hare, and S. L. Prunty. *Rev. Sci. Instr.*, 77(10):10E510, 2006.
- [78] L. Lauro-Taroni L, B. Alper, R. Giannella, K. Lawson, F. Marcus, M. Mattioli, P. Smeulders, and M von Hellermann. In *21st EPS Conference on Controlled Fusion and Plasma Physics*, page 102. ECA, 1994.
- [79] A. D. Whiteford. In *Proc. 31st European Conf.*, page 1.159. ECA, 2004.
- [80] I. Lehane, G. Turri et al. In *Proceedings of the 30th EPS Conference on Controlled Fusion and Plasma Physics*, pages P-3.92. ECA, 2003.
- [81] R. C. Isler. *Plasma Physics and Controlled Fusion*, 36:171, 1994.
- [82] W. R. Heiss, J. L. Farjon, R. Guirlet, and M. Druetta. *Rev. Sci. Instr.*, 73(4):1775, 2002.

- [83] M. von Hellerman et al. *Rev. Sci. Inst.*, 77:10F516, 2006.
- [84] T. A. Green, E. J. Shipsey, and J. C. Browne. *Phys. Rev. A*, 25(3):1364, 1982.
- [85] W. Fritsch and C. D. Lin. *Phys. Rev. A*, 29(6):3039, 1984.
- [86] R. E. Olson and D. R. Schultz. *Science*, 58:290, 1923.
- [87] H. Ryufuku and T. Watanabe. *Phys. Rev. A*, 18(5):2005, 1978.
- [88] W. Fritsch. *Phys. Rev. A*, 30(6):3324, 1984.
- [89] Hiroshi Ryufuku. *Phys. Rev. A*, 25(2):720, 1982.
- [90] R. E. Olson. *Phys. Rev. A*, 24(4):1726, 1981.
- [91] R Hoekstra, H Anderson, F W Blik, M von Hellermann, C F Maggi, R E Olson, and H P Summers. *Plasma Physics and Controlled Fusion*, 40(8):1541, 1998.
- [92] L. F. Errea, C. Illescas, L. Méndez, B. Pons, A. Riera, and J. Suárez. *J. Phys. B: At. Mol. Opt. Phys.*, 39:L91, 2006.
- [93] C. F. Maggi et al. Not yet published.
- [94] J. G. Lodge, I. C. Percial, and D. Richards. *J. Phys. B: At. Mol. Opt. Phys.*, 9:239, 1976.
- [95] L. A. Vainshtein, I. I. Sobelman, and E. A. Yukov. *Excitation of Atoms and Broadening of Spectral Lines*. Springer, Berlin, 1981.
- [96] S. J. Gee et al. MAST neutral beam long pulse upgrade. *Fusion Engineering and Design*, 74:403, 2005.
- [97] R. J. Hawryluk. *Physics of Plasmas Close to Thermonuclear Conditions*, page 19. CEC, Brussels, 1980.
- [98] M. Tournianski. Private Communication.
- [99] A. Patel, P. G. Carolan, N. J. Conway, and R. J. Akers. *Rev. Sci. Inst.*, 75(11):4944, 2004.

- [100] S. D. Loch, J. A. Ludlow, M. S. Pindzola, A. D. Whiteford, and D. C. Griffin. *Phys. Rev. A*, 72:052716, 2005.
- [101] A. R. Foster, G. F. Counsell, and H. P. Summers. *J. Nucl. Mat.*, 363-365:152, 2007.